Selecting Electron Antineutrino Charged-Current Interactions at the T2K ND280

Luke Southwell

Lancaster University

August 17, 2016

Lancaster University

Abstract

The contamination from $\bar{\nu}_e$ in the T2K antineutrino beam is predicted to be approximately 1% and needs to be evaluated in order to constrain the systematic uncertainties in a T2K antineutrino oscillation measurement. In this thesis we present a $\bar{\nu}_e$ charged-current selection with which we test the Monte Carlo prediction using T2K data. To select $\bar{\nu}_e$ charged-current events, the tracker region and electromagnetic calorimeters of the T2K off-axis near detector are used.

The selected sample has a $\bar{\nu}_e$ purity of $(41.9\pm2.4)\%$ and an efficiency of $(27.1\pm1.7)\%$. The data to Monte Carlo ratio for $\bar{\nu}_e$ charged-current inclusive interactions is $1.07 \pm 0.16(\text{stat.}) \pm 0.13(\text{syst.})$.

Declaration

No part of this thesis has been previously submitted for the award of a higher degree.

Preface

My work on $\bar{\nu}_e$ at T2K began after it was determined that my prior work in looking for sterile neutrino oscillations using the ν_e CC selection, for the ND280, would explore no new regions of phase space. As part of a wider collaboration not all of this work was undertaken solely by myself and several parts were done either in collaboration with others or is the work of others that I adapted to create a $\bar{\nu}_e$ selection.

Chapter 2 describes the theory behind neutrino physics and is generic to all neutrino experiments. Chapter 3 covers the T2K experiment which was already established when I joined the collaboration. While I was in charge of monitering the upload scripts mentioned in Section 3.2.3, I made minimal changes to the scripts which had been written by my predecessors.

Chapter 4 coveres my development of the $\bar{\nu}_e$ CC selection which was based on the existing ν_e CC selection. The selection criteria shared between the two selections, as discussed in Section 4.2 were developed by Ben Smith of Imperial College London for his ν_e CC selection. My work on surmounting the additional challenges a $\bar{\nu}_e$ CC selection presents is covered from Section 4.3.1 onwards.

Chapter 5 details the assessment of the systematic uncertainties associated with the $\bar{\nu}_e$ CC selection. The highland tools package described in Section 5.1.1 was developed by several members of the T2K collaboration. The code used to calculate the flux systematic uncertainty detailed in Section 5.2 was provided by Iain Lamont though required some modification for antineutrino beam mode. The TPC-ECal matching systematic uncertainty in Section 5.3 was calculated by Iain Lamont.

Acknowledgements

Firstly I would like to thank Dr. Laura Kormos, Dr. Helen O'Keeffe, Dr. Alex Finch and all the staff at Lancaster University who have helped me through this.

Thank you to the other students that I shared an office with during my time at Lancaster University and during my time in Tokai. Without some of you I doubt I would have kept my sanity.

Thank you to Mr. Colin Brooke who helped nurture my growing love of physics and set me on the path to where I am now.

Thank you to my family for their continued support during my PhD, there really is no substitute for a home cooked Sunday roast.

Jenni Field may be last but is be no means the least on this list. Her support of my decision to live abroad for a year was invaluable and her continued love and support through my PhD has helped my get through many of the lower points I have had.

The Thesis encouragement stick for all the help provided will not be missed.

Quote

"There are only five notes in the musical scale, but their variations are so many that they cannot all be heard. There are only five basic colours, but their variations are so many that they cannot all be seen. There are only five basic flavours, but their variations are so many that they cannot all be tasted. There are only two kinds of charge in battle, the unorthodox surprise attack and the orthodox direct attack, but variations of the unorthodox and the orthodox are endless. The unorthodox and the orthodox give rise to each other, like a beginning-less circle – who could exhaust them?"

Sun Tzu, The Art of War - translated by Thomas Cleary

Contents

List of Tables

List of Figures

Chapter 1

Introduction

The standard model of particle physics [1, 2, 3], which is discussed in Section 2.1, is currently the best model of subatomic interactions available to the particle physics community. The accuracy of the standard model is such that several fundamental particles and many bound states of fundamental particles have been predicted long before they were discovered experimentally, the most obvious example being the Higgs boson [4].

However, there are still many examples of physical phenomena prevalent in the universe which are beyond the standard model.

One of these examples is the matter-antimatter asymmetry in the universe. This could be explained by CP violation which is often seen in quark interactions (for example asymmetric B–$\bar{B}$ meson oscillation, where the transformation does not occur with the same probability in each direction); however, there is insufficient CP violation in the quark sector to account for the matter-antimatter asymmetry in the universe. Therefore it is important to measure the CP violation in the leptonic sector which may occur during neutrino oscillations.

The biggest discoveries of physics that exists beyond the standard model during the last century were that neutrinos have mass, and that they are capable of violat-

ing conservation of lepton flavour through flavour–changing neutrino oscillations, both of which are discussed in Section 2.3 of Chapter 2.

Several parameters in neutrino physics are still unmeasured and are discussed in Section 2.4 of Chapter 2. In order to answer the questions posed by neutrino physics several experiments have been built, one of which is the T2K experiment in Japan (discussed in Chapter 3). The T2K experiment uses ν_μ and $\bar{\nu}_\mu$ beams to investigate the properties of neutrino oscillations. However, the T2K beam is not perfect and contains impurities from other flavours of neutrinos, particularly in the $\bar{\nu}_\mu$ case where $\bar{\nu}_e$ is a significant component of the beam. To quantify some of this contamination, a selection was developed using the T2K near detector (discussed in Section 3.2.2 of Chapter 3) so that the $\bar{\nu}_e$ present in the beam before flavour-changing could be measured. The systematic uncertainties on this measurement and how they were obtained are discussed in Chapter 5. The results of the selection are presented in Section 4.4 of Chapter 4, and conclusions are drawn in Chapter 6.

Chapter 2

Neutrino Physics

2.1 The Standard Model

In order to discuss the neutrino it is imperative that the theory at the forefront of particle physics be briefly discussed. This theory is the standard model. The standard model of particle physics models the interactions of particles through three fundamental forces, which are:

- The electromagnetic force, which mediates interactions between particles with electric charge via exchange of photons.

- The weak force, which mediates interactions between fundamental particles with half-integer spin via exchange of a $W^{\pm}$ or Z^0 boson.

- The strong force, which mediates interactions between particles with colour via exchange of gluons.

Each particle in the standard model has a set of quantum numbers including spin, electric charge, colour charge, baryon number and several quantum numbers relating to the particle's flavour. Depending on the quantum numbers a particle possesses, it can have several classifications.

When expressed as a multiple of the reduced Planck constant $\hbar$, a particle's spin (the intrinsic angular momentum a particle possesses) is either integer or half-integer. Fundamental particles with half-integer spin are classified as fermions, whereas fundamental particles with integer spin are classified as bosons. These two classifications of particles obey different rules in the universe. Fermions obey Fermi-Dirac statistics and the Pauli exclusion principle [5], which states that there cannot be two identical fermions simultaneously having the same quantum numbers. All of the classical matter in the universe is composed of fermions. The fundamental fermions are shown in Figure 2.1 in purple and green. Bosons, by contrast, obey Bose-Einstein statistics [6] and do not obey the Pauli exclusion principle. Bosons take the role of force carriers with each of the three fundamental forces listed above being mediated by one or more bosons: the strong force is carried by gluons, the electromagnetic force is carried by the photon and the weak force is carried by the $W^{\pm}$ and Z^0 bosons. Figure 2.1 shows the bosons in red.

Fermions which have the colour property are known as quarks and are the only fermions that experience the strong force. Figure 2.1 shows the quarks in purple. Colour comes in three charge types: red, green and blue. Quarks have one of these properties as either colour or anti-colour, and gluons (of which there are eight) contain two different colour charges, one colour charge and one anti-colour charge. All quarks are electrically charged with one set (u,c,t) having an electric charge of $\frac{2}{3}$ the charge of a positron and the other set (d,s,b) having an electric charge of $-\frac{1}{3}$ the charge of a positron. The antiparticles of quarks, which have anti-colour, have the opposite charges. The $\frac{2}{3}$ charge set are referred to as up-type quarks and the $-\frac{1}{3}$ charge set are referred to as down-type quarks with different quarks of the same set being referred to as having different flavours. The down-type and up-type quarks have the strongest coupling to their closest mass partner and so pair off by mass (lightest to lightest etc.) to form a generation of quarks. Each column of

fermions in Figure 2.1 is one generation. Recent experiments at CERN have ruled out the possibility of a fourth generation of quarks existing in nature [7].

The colour charge is subject to a phenomenon known as colour confinement [8] where, unlike the other forces, the strong force does not diminish with distance. This leads to an absence of free quarks existing in nature, and instead quarks group into composite, colour-neutral particles. As the colour force has three charges, in order to be colour-neutral, quarks can either form groups of three with one of each colour charge, or pairs with a colour charge and an anticolour charge of the same type. Particles composed of three quarks are known as baryons and have a quantum number, known as the baryon number, which is a conserved quantity. Particles composed of a quark and an antiquark are known as mesons. Larger pairings are also possible with results consistent with a pentaquark (4 quarks and an antiquark) having been observed at CERN [9]. Collectively, any particles composed of quarks are known as hadrons.

Fermions which do not have the colour property are known as leptons. Figure 2.1 shows the leptons in green. Leptons are also split into two subclassifications by their electric charge. Unlike quarks, where both subclassifications have some electric charge, one group of leptons has a charge of -1 times the positron charge, while the other has no electric charge. The three flavours of charged leptons are the electron (e), the muon (μ) and the tau (τ) and the three uncharged leptons are the electron neutrino (ν_e), the muon neutrino (ν_μ) and the tau neutrino (ν_τ). As may be inferred from their names, the charged leptons and neutrinos are linked, like the quarks, into three generations, albeit with some additional subtleties as covered in Section 2.3. The possibility of a fourth generation of neutrinos with a mass less than half the mass of the Z^0 boson has been ruled out by experiments at LEP, as will be discussed in Section 2.4.

In total there are 61 fundamental particles in the standard model as shown in

Particle Classification	Generations	Charge Types	Antiparticles	Colour	Total
Quark	3	2	yes	yes	36
Lepton	3	2	yes	none	12
Gluon	1	no charge	own	yes	8
Photon	1	no charge	own	none	1
Z boson	1	no charge	own	none	1
W boson	1	2	yes	none	2
Higgs	1	no charge	own	none	1
Total					61

Table 2.1: The fundamental particles of the standard model that have so far been discovered.

Table 2.1. Figure 2.1 also shows the fundamental particles of the standard model. All of the force-carrying bosons couple to quarks, all but the gluons couple to the charged leptons and only the $W^{\pm}$ and Z^0 couple to neutrinos.
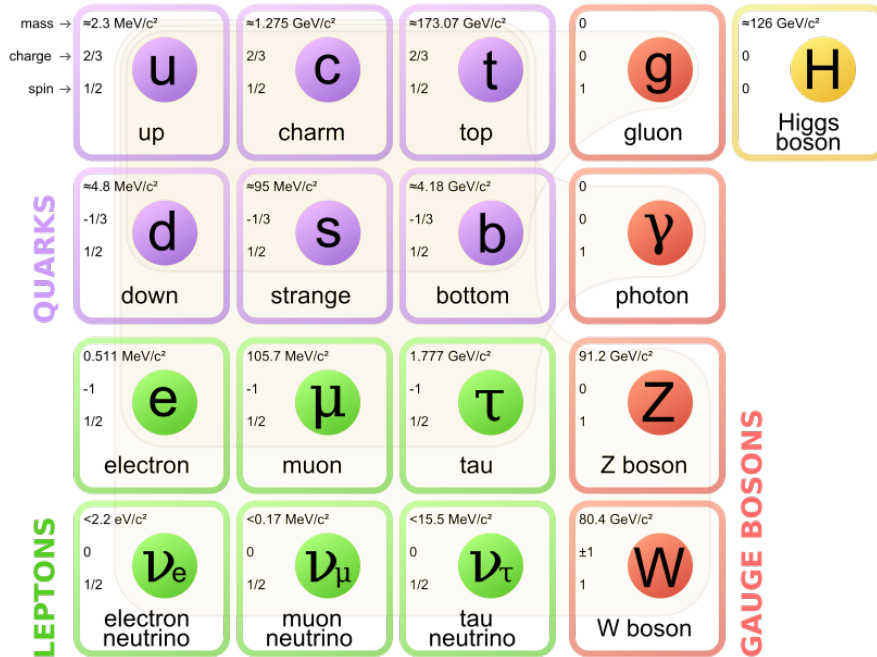
Figure 2.1: The fundamental particles of the standard model. Quarks are highlighted in purple, leptons are highlighted in green, gauge bosons are highlighted orange and the Higgs is highlighted in yellow [10].

A property which derives from a particle's spin is its helicity. The helicity of a particle is the projection of a particle's angular momentum onto the direction

of its momentum and can either be left-handed or right-handed. A particle has right-handed helicity if the momentum and spin vectors are parallel; if the vectors are anti-parallel then a particle has left-handed helicity as shown in Figure 2.2.
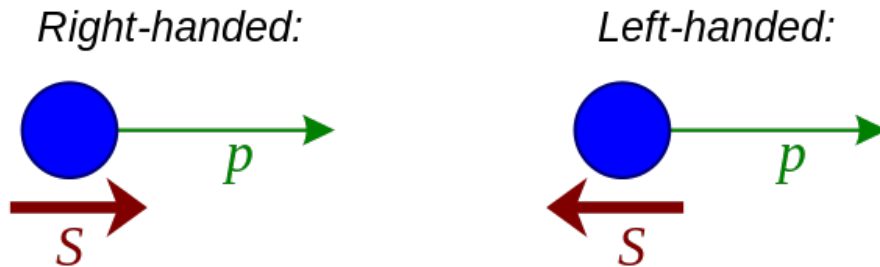
Figure 2.2: A particle's helicity as defined by its momentum and spin vectors, shown as p and S respectively [11].

The chirality of a particle describes whether two particles are identical or are mirror images of each other. Chirality is similar to helicity, in that chirality can also be expressed as a projection of a particle's angular momentum onto the direction of its momentum. For a massless particle the helicity and chirality are identical; however, for particles with mass, chirality and helicity may differ as helicity is not Lorentz invariant. This is because a massive particle can be observed to have a different momentum vector by two different observers but both observers will measure the same spin vector. In this case, while the helicity can change between observers, a particle will not change between itself and its mirror image under a Lorentz transformation. This means that chirality is an intrinsic property of a particle.

A transformation which changes a particle into its mirror image is known as a parity transformation. When combined with a transformation that flips the charge this creates a charge-parity (CP) transformation. According to the principle of CP-symmetry, the laws of physics should be the same after a CP transformation; however, as evidenced by the matter dominance over antimatter in the observable universe, this is not the case. Currently, the measured parameters in the standard

model do not have sufficient CP violation to account for the matter dominance over antimatter in the observable universe, and searches for sources of this CP violation are a major driving force behind particle physics experiments as will be shown in Section 2.3.

Overall, the standard model is an extremely reliable theory but it does have several shortcomings, such as not incorporating the mixing of neutrinos or their non-zero masses, as will be discussed in Section 2.3. The standard model is also considered to be inelegant as a theory as it requires 19 numerical constants as inputs which must be established experimentally. As a predictive tool, the standard model has enjoyed great success predicting the existence of several particles before their discovery, such as the top quark and, as will be discussed in Section 2.2, neutrinos.

2.2   History of the Neutrino

In 1930 it was observed that, while alpha decay has a single-peak energy spectrum as is consistent with a two-body decay, the energy spectrum of beta decay was continuous. This posed a problem for physicists at the time as only two bodies (the emitted beta particle and the recoil nucleus) had been observed in beta decay and so it appeared that energy was being lost during the beta decay process. To preserve the law of energy conservation while still allowing for this continuous energy spectrum, Wolfgang Pauli proposed that a third particle was involved during beta decay that had not yet been observed, thus making the process a three-body decay [12]. This third particle would need to have no electric charge and a mass far smaller than anything that had been observed at the time. With a third, unobserved particle carrying the missing energy and momentum, beta decay could occur without violating the law of energy conservation [13].

In 1956 C. Cowan and F. Reines confirmed the existence of the neutrino by looking at inverse beta-capture [14]:

$$\bar{\nu}_e + p \rightarrow e^+ + n \tag{2.1}$$

using antineutrinos coming from a nuclear reactor, thus confirming Pauli's theory. Though at the time it was thought that there was only one type, or flavour, of neutrino, as additional charged leptons were discovered their neutrino partners were also found with the ν_μ first being detected in 1962 [15] and the ν_τ first being detected in 2000 [16]. These are referred to as different flavours of neutrinos and are shown in Table 2.2 along with their mass limits.

Neutrino Flavour	Mass Limit
ν_e	< 2 eV
ν_μ	< 170 keV
ν_τ	< 18.2 MeV

Table 2.2: The different flavours of neutrinos and the limits on their masses at the 90% confidence level [17].

A problem began to arise in the field of neutrino physics in 1965 when Ray Davis and John Bahcall decided to try to detect neutrinos that are being produced via nuclear fusion in the core of the sun via the p-p process, which begins with the interaction in Equation 2.2:

$$p + p \rightarrow d^+ + e^+ + \nu_e. \tag{2.2}$$

This led to the construction of the Homestake experiment [18, 19]. Davis and Bahcall measured a difference between the solar neutrino flux and the theoretical predictions from the standard solar model [20, 21] whereby the theoretical flux was three times the measured flux. This measurement of the ν_e flux from the sun was eventually backed up by evidence from further experiments such as

Kamiokande in 1991 [22], GALLEX in 1995 [23], SAGE in 1999 [24], GNO in 2000 [25] and Super-Kamiokande in 2001 [26].

The discrepancy between the theoretical prediction and the experimental measurements of the ν_e flux from the sun was called the Solar Neutrino Problem.

In 1967 Bruno Pontecorvo proposed a possible way to resolve the discrepancy between the experimentally-observed solar ν_e flux as compared to the theoretical predictions of the solar model by defining a mechanism via which neutrinos of one flavour could change into neutrinos of a different flavour; therefore, there would be a deficit of ν_e measured on Earth but not of the total number of neutrinos coming from the sun [27]. In 2001, the Sudbury Neutrino Observatory (SNO) in Canada confirmed the existence of solar neutrino flavour-change using neutral-current neutrino interactions (see Section 2.5) to measure the solar neutrino flux. SNO measured a total neutrino rate of $(5.44 \pm 0.99) \times 10^6$ cm^{-2}s^{-1} [28] which was consistent with Bahcall's prediction of $(5.05 \pm 1.01) \times 10^6$ cm^{-2}s^{-1} [21]. As will be seen in Section 2.3, neutrinos must have mass in order to change flavour.

The Super-Kamiokande observatory in Japan observed a different kind of neutrino deficit in 1998. The source of neutrinos for this measurement was cosmic ray interactions in the Earth's upper atmosphere. During cosmic ray interactions, the majority of neutrinos are produced by pion decay, which gives a ν_μ to ν_e ratio of 2 to 1. However, SK observed that the number of ν_μ coming from the nadir direction, so as to have travelled through the Earth, is half the number of ν_μ coming from the zenith, so as to only have travelled through the Earth's atmosphere [29]. This indicates that neutrinos oscillate and therefore they have mass, which was not what was predicted in the standard model.

The final confirmation that neutrinos change flavour came from the KamLAND experiment in 2003, which looked at $\bar{\nu}_e$ produced in nuclear reactors. By measuring the energy of the neutrinos, KamLAND was able to show a clear oscillation pattern

that is inconsistent with a no-oscillation hypothesis as shown in Figure 2.3 [30].
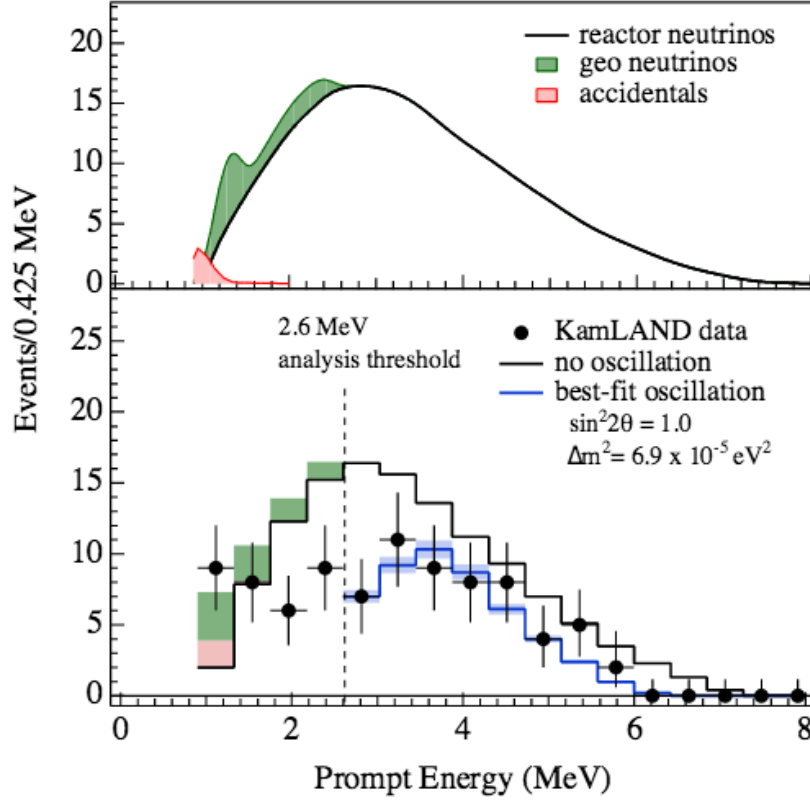
Figure 2.3: Upper panel: Expected reactor $\bar{\nu}_e$ energy spectrum with contributions of geoneutrinos and accidental background. Lower panel: Energy spectrum of the observed prompt events, along with the expected no oscillation spectrum and best fit including neutrino oscillations. The shaded band indicates the systematic error in the best-fit spectrum. The vertical dashed line corresponds to the analysis threshold at 2.6 MeV [30].

2.3   Neutrino Oscillations

Neutrino flavour oscillations arise due to neutrino mass states and flavour states not matching up one to one, but instead each of the three flavour states, ν_e, ν_μ and ν_τ, is a mix of the three mass states, ν_1, ν_2 and ν_3, and vice versa. For a neutrino of a given energy, the heavier mass states travel slightly slower than the

lighter states; hence, the proportions of the mass states change as the neutrino propagates through space leading to a change in the flavour states.

In a two-flavour case (ν_e and ν_μ), when a ν_e is created the superposition of mass states is:

$$|\nu_e\rangle = U_{e1}|\nu_1\rangle + U_{e2}|\nu_2\rangle \tag{2.3}$$

where U_{e1} and U_{e2} are elements of the two-flavour oscillation matrix:

$$\begin{pmatrix} \nu_e \\ \nu_\mu \end{pmatrix} = \begin{pmatrix} U_{e1} & U_{e2} \\ U_{\mu1} & U_{\mu2} \end{pmatrix} \begin{pmatrix} \nu_1 \\ \nu_2 \end{pmatrix}. \tag{2.4}$$

The 2×2 matrix in Equation 2.4 is equivalent to a two-dimensional rotation matrix:

$$U = \begin{pmatrix} \cos(\theta) & \sin(\theta) \\ -\sin(\theta) & \cos(\theta) \end{pmatrix} \tag{2.5}$$

where if θ was zero, the mass and flavour states would be the same; however, as mentioned above, experiments show this is not the case.

As the neutrinos travel, they evolve with time and distance. After time t and distance x, the flavour state $|\nu_\beta(x,t)\rangle$ can be expressed as:

$$|\nu_\beta(x,t)\rangle = e^{-i(P_i x - E_i t)}|\nu_\alpha(0,0)\rangle. \tag{2.6}$$

where E_i and P_i are the energy and momentum of the neutrino mass state i.

It is assumed that the neutrino is highly relativistic, which allows us to make

the approximation

$$E_i \approx P + (m_i)^2/2E \qquad (2.7)$$

where m_i is the mass of the ith mass state. The probability of a neutrino being found in state β when it was created in state α is

$$P(\nu_\alpha \to \nu_\beta) = |\langle \nu_\alpha | \nu_\beta(t) \rangle|^2, \qquad (2.8)$$

which for a neutrino of energy E traveling distance L is written as:

$$P(\nu_\alpha \to \nu_\beta) = \delta_{\alpha\beta} - 4 \sum_{j>i} Re(U_{\alpha j} U_{\beta j} U_{\alpha i} U_{\beta i}) \sin^2 \left((\Delta m_{ji}^2) \frac{L}{4E} \right) \qquad (2.9)$$

where i and j represent mass states, Δm_{ji}^2 is the mass-squared difference $(m_j^2 - m_i^2)$ and $U_{\alpha j}$ are the components of the two-flavour mixing matrix shown in Equation 2.5.

For the more complex three-flavour case the probability of a neutrino of energy E and flavour α being detected as flavour β after a distance L is

$$\begin{aligned} P(\nu_\alpha \to \nu_\beta) = \delta_{\alpha\beta} \\ -4 \sum_{j>i} Re(U_{\alpha j}^* U_{\beta j} U_{\alpha i} U_{\beta i}^*) \sin^2 \left((\Delta m_{ji}^2) \frac{L}{4E} \right) \\ +2 \sum_{j>i} Im(U_{\alpha j}^* U_{\beta j} U_{\alpha i} U_{\beta i}^*) \sin^2 \left((\Delta m_{ji}^2) \frac{L}{4E} \right) \end{aligned} \qquad (2.10)$$

where the $U_{\alpha j}$ are the components of the three-flavour Pontecorvo-Maki-Nakagawa-Sakata (PMNS) [31] mixing matrix given by:

$$U = \begin{pmatrix} C_{12}C_{13} & S_{12}C_{13} & S_{13}e^{-i\delta} \\ -S_{12}C_{23} - C_{12}S_{23}S_{13}e^{i\delta} & C_{12}C_{23} - S_{12}S_{23}S_{13}e^{i\delta} & S_{23}C_{13} \\ S_{12}S_{23} - C_{12}C_{23}S_{13}e^{i\delta} & -C_{12}C_{23} - S_{12}C_{23}S_{13}e^{i\delta} & C_{23}C_{13} \end{pmatrix}. \qquad (2.11)$$

Here,

- $C_{ij} = \cos\theta_{ij}$.

- $S_{ij} = \sin\theta_{ij}$.

- θ = the mixing angles for the rotation matrices, which transform between the mass eigenstates and the flavour eigenstates.

- δ = the CP-violating phase. CP is conserved in neutrino interactions if this phase is equal to 0 or π.

Equation 2.11 can be decomposed into three two-flavour oscillation matrices:

$$\begin{pmatrix} 1 & 0 & 0 \\ 0 & C_{23} & S_{23} \\ 0 & -S_{23} & C_{23} \end{pmatrix} \begin{pmatrix} C_{13} & 0 & S_{13}e^{-i\delta} \\ 0 & 1 & 0 \\ -S_{13}e^{i\delta} & 0 & C_{13} \end{pmatrix} \begin{pmatrix} C_{12} & S_{12} & 0 \\ -S_{12} & C_{12} & 0 \\ 0 & 0 & 1 \end{pmatrix}. \qquad (2.12)$$

Each of these matrices corresponds to a different wavelength of oscillation for a given energy of neutrino; because of this they are often referred to by the types of experiment on which they have the largest effect.

Atmospheric neutrino oscillations are oscillations by neutrinos that were created during cosmic ray interactions in the upper atmosphere. These neutrinos often have energies from a few hundred MeV to several TeV and have a baseline of the diameter of the Earth. The dominant term when calculating atmospheric

oscillation probabilities is θ_{23}; because of this the left-most matrix in Equation 2.12 is sometimes referred to as the atmospheric oscillation matrix.

Reactor neutrino oscillations are oscillations by neutrinos that were created in nuclear reactors. These neutrinos have energies of a few MeV and baselines of tens of meters to a few hundred kilometers. The dominant term when calculating reactor neutrino oscillation probabilities is θ_{13}; because of this the middle matrix in Equation 2.12 is sometimes referred to as the reactor oscillation matrix.

Solar oscillations are oscillations by neutrinos that were created in the core of the sun. These neutrinos have energies less than 20 MeV and a baseline of 1 AU. The dominant term when calculating solar oscillation probabilities is θ_{12}; because of this the right-most matrix Equation 2.12 is sometimes referred to as the solar oscillation matrix.

Accelerator oscillations are oscillations by neutrinos that were created using a particle accelerator. These neutrinos have evergies of a few GeV and baselines of hundreds of kilometers. θ_{23} and θ_{13} have the largest effects when considering accelerator oscillations.

In 2011 T2K found the first indications for a nonzero θ_{13} [32] which was the last of the three oscillation angles to be measured. The middle term of Equation 2.12 shows that if θ_{13} were zero, it would be impossible to measure δ, so non-zero θ_{13} is necessary for future neutrino experiments which plan to attempt this. The Daya Bay experiment then measured $\sin^2(2\theta_{13})$ to be 0.092 ± 0.016 (stat.) ± 0.005 (syst.) in 2012 [33]. Currently, all of the neutrino oscillation parameters apart from δ have been measured [17] and the global average for each of the parameters is shown in Table 2.3.

The oscillation angles in the PMNS matrix are significantly larger than the angles in its quark sector equivalent (Cabibbo-Kobayashi-Maskawa matrix). This results in a much larger rate of oscillation in the neutrino sector compared to the

Parameter	Global Average
θ_{12}	$34. \pm 1$ degrees
θ_{13}	8.5 ± 0.2 degrees
θ_{23}	45 ± 4 degrees
Δm_{21}^2	$(7.53 \pm 0.18) \times 10^{-5}\ eV^2$
$\mid \Delta m_{32}^2 \mid$	$(2.44 \pm 0.06) \times 10^{-3}\ eV^2$

Table 2.3: The global average for each of the neutrino oscillation parameters that have been measured [17].

quark sector.

Although many parameters in neutrino physics have been measured in the past decade, there are still some unknown quantities. The fact that the absolute value of Δm_{32}^2 is not known also opens up the possibility for interesting physics which will be discussed in Section 2.4.

2.4   Remaining Questions

There are several important questions which remain unanswered in neutrino physics. These questions are prominent in the aims of both current and future neutrino experiments and are discussed below.

Although the two mass splittings $m_j^2 - m_i^2$ of the three neutrinos have been measured, it is currently unknown whether mass state ν_3 is the heaviest or lightest of the neutrinos. It is, however, known that ν_2 is heavier than ν_1 due to the effect that matter interactions have on the solar neutrino oscillation probability. The matter effect or Mikheyev-Smirnov-Wolfenstein (MSW) [34] effect is the mechanism by which neutrino oscillation probabilities change when they are traveling through matter instead of empty space. The presence of electrons in matter gives ν_e an additional charged-current coherent scattering interaction which ν_μ and ν_τ do not experience. This gives neutrinos, depending on their ν_e component, a different effective mass. As seen in Equation 2.9 neutrino oscillations depend the

squared mass difference, and so the oscillation probabilities in matter are different to the probabilities in a vacuum. Solar neutrinos, which travel via the sun's dense core, undergo measurable MSW effects. Other neutrinos detected to date do not. This gives rise to two possible mass hierarchies: the normal hierarchy where the mass states ν_1, ν_2 and ν_3 are in order from lightest to heaviest, and the inverted hierarchy where ν_3 is lighter than states ν_1 and ν_2, as shown in Figure 2.4.
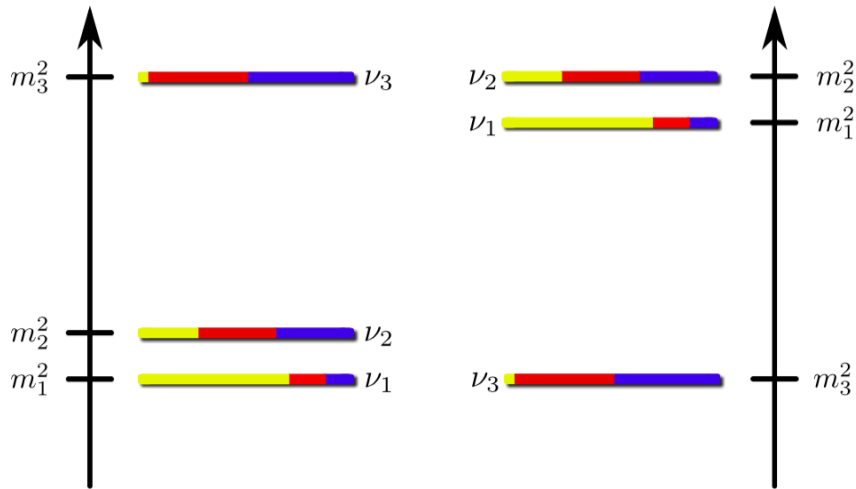
Figure 2.4: The two possible orderings of the neutrino mass states. The colours represent the distributions of the flavour states within the mass states, with yellow representing ν_e, red representing ν_μ and blue representing ν_τ [36].

The octant of θ_{23} is also unknown. θ_{23} is measured during atmospheric oscillations where it has the form $\sin^2(2\theta_{23})$; therefore, as θ_{23} is close to maximal it could either be slightly above 45 degrees or slightly below. The world's best measurement at time of writing was performed by the T2K experiment which found that $\sin^2(\theta_{23}) = 0.514 \pm 0.055$ [35]. The octant of θ_{23} is correlated with the mass hierarchy. In the latest T2K results if $\theta_{23} < 45$ degrees the inverted hierarchy is favoured and if $\theta_{23} > 45$ degrees the normal hierarchy is favoured. If θ_{23} is exactly 45 degrees ($\sin^2(\theta_{23}) = 0.5$), it would indicate that some high-energy symmetry is present.

Absolute neutrino mass is another unsolved problem in neutrino physics. Even though the squared differences between the masses of the neutrino mass states are known, the absolute mass of any of the states is currently unknown. The best limits suggest that the average neutrino mass is less than an electron-volt [17]. The neutrino mass is an important variable in models of early universe evolution as shown in Figure 2.5. After the big bang all particles in the universe were in thermal equilibrium; however, as the universe expanded the mean free paths of the particles increased up to a series of critical points where each flavour of particle "decouples" and falls out of thermal equilibrium. Unlike photons that decoupled approximately 200000 years after the big bang, neutrinos decoupled after approximately 2 years, allowing them to move mass significantly earlier in the universe's initial expansion and so have a much larger effect on mass distribution on a cosmic scale.
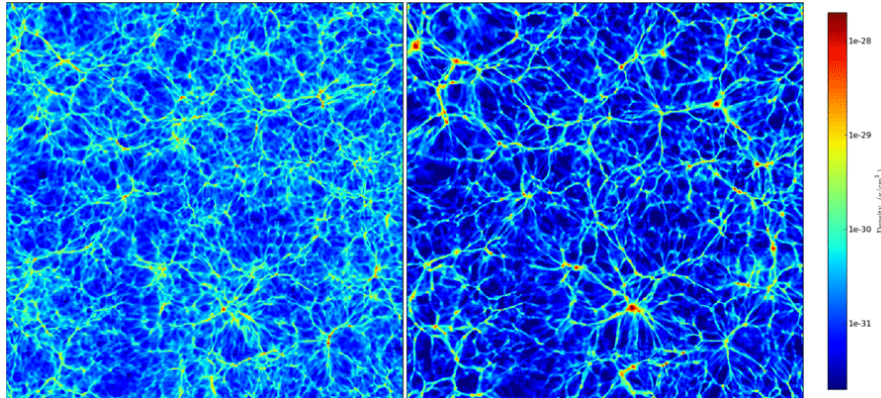
Figure 2.5: A simulation of the matter density of the universe, where the only parameter that changes is neutrino mass. In the image on the left the neutrino is massless, on the right the neutrino has an average mass of 1.9 eV. In the simulation with the massless neutrino, matter is spread much more uniformly than in the case with the massive neutrino where most of the mass is concentrated into a small number of large structures [37].

The current best limit on the average neutrino mass is $m_\nu < 0.23$ eV from cosmological observations, though the measurement is extremely model-dependent [37]. The best direct experimental limit comes from the Mainz tritium decay experiments where the end point of the energy spectrum for the final state electron

is dependent on the neutrino mass. The current best measurement from this technique gives an upper limit on the ν_e mass of 2.3 eV/c^2 [38]. The KATRIN experiment is designed to push this limit down to 200 meV [39].

The amount of CP violation in neutrino oscillations is unknown. The value of δ in Equation 2.11 has not been measured. As of the time of writing, CP violation has only been observed in meson interactions, mainly B and K oscillations. CP violation has not yet been observed in baryons or leptons; however, the amount of CP violation observed in meson interactions is insufficient to explain the matter-antimatter asymmetry in the universe. Given the role neutrinos play in the mass distribution of the universe, the neutrino sector would be an ideal place to observe CP violation.

Another unanswered question is whether neutrinos are Dirac or Majorana fermions. A Majorana fermion is one which is its own antiparticle. All standard model fermions except the neutrino are known to be Dirac fermions. The other fermions are known to be Dirac because they have non-zero charge and a Majorana particle must have zero charge or else it would violate the principle of charge conservation. The neutrino, however, being the only fermion with zero charge, could be either Majorana or Dirac. If the neutrino is Majorana, this would introduce another mixing matrix to the three-flavour oscillations in Equation 2.12 which takes the form

$$U = \begin{pmatrix} 1 & 0 & 0 \\ 0 & e^{i\alpha_1/2} & 0 \\ 0 & 0 & e^{i\alpha_2/2} \end{pmatrix} \tag{2.13}$$

where α_1 and α_2 are the Majorana phase factors and are zero if the neutrino is a Dirac fermion [40].
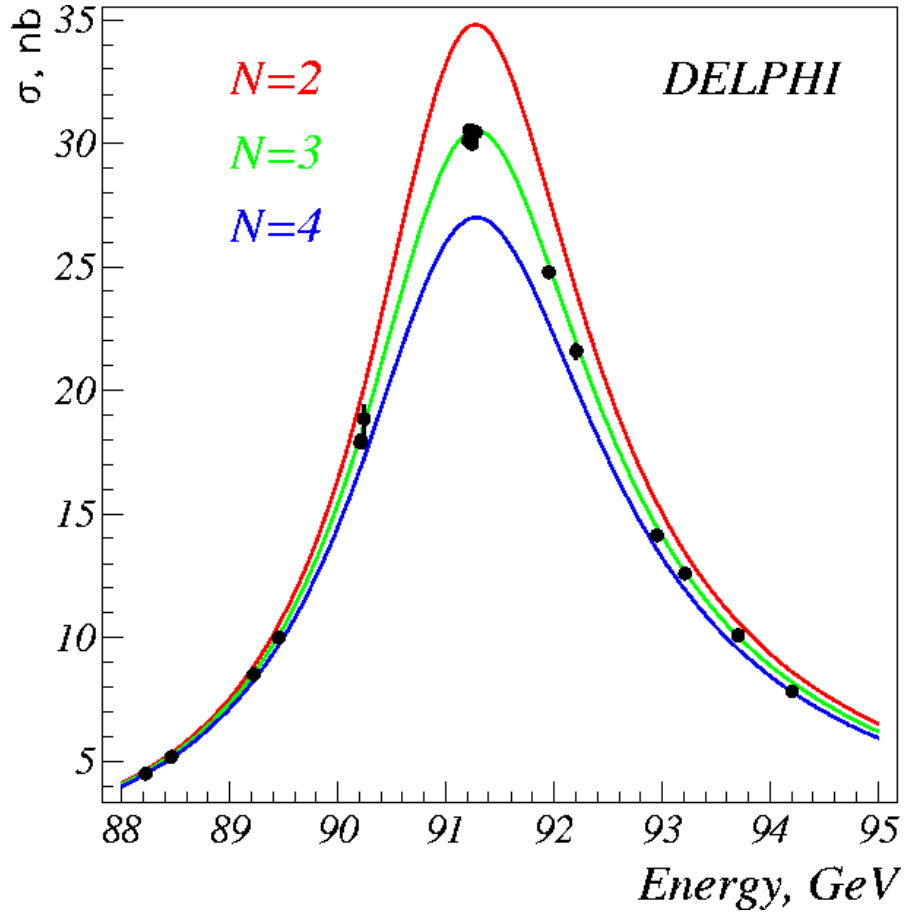
Figure 2.6: The Z^0 bozon decay width as measured by the DELPHI experiment [41]. The coloured lines show the theoretical decay width for 2 (red), 3 (green) and 4 (blue) neutrino flavours. The data points, which have error bars smaller than the points, fit the three neutrino flavour theoretical curve.

The number of neutrino flavour states was determined by experiments at the LEP collider using the decay width of Z^0 bosons as shown in Figure 2.6. However, LSND [42] measured another mass splitting in addition to the two mentioned in Section 2.3, which is of the order of 1 eV^2. With three neutrino mass splittings of different magnitudes more than three neutrinos are required, in conflict with the LEP result that shows that only three neutrinos actively couple to the Z^0 boson. This indicates that any additional neutrinos, if they exist, are "sterile" neutrinos that have no coupling to the weak force, or else they are heavier than half the Z mass, i.e. approximately 45 GeV, which would make them many orders

of magnitude heavier than the other neutrino states.

Assuming that they have no weak coupling, the only way to observe these sterile neutrinos is through the effect they have on neutrino oscillations. Due to the large mass-splitting, sterile oscillations would occur over much shorter distances than other neutrino oscillations and they are widely used to explain several anomalous results such as the reactor neutrino anomaly [43], the gallium anomaly [44] and the MiniBooNE excess [45]. However, several other explanations have been proposed for these anomalies [46, 47], and null results from MINOS [48] and other sterile searches have thrown the idea of sterile neutrinos into further contention.

The T2K experiment has no sensitivity to the absolute neutrino mass and while it does have sensitivity to θ_{23} and Δm^2_{32} it is unlikely that it will accumulate enough data to resolve the octant and mass-hierarchy problems [49]. However, by combining results from reactor experiments with both neutrino and antineutrino data it is possible for T2K to eliminate half of the δ_{cp} phase space at the 90% confidence level as shown in Figure 2.7 [50]. Figure 2.7(a) shows that with just neutrino data no constraint can be made on δ_{cp}; however, Figure 2.7(b) shows that by taking an equal mix of neutrino and antineutrino data almost 50% of the δ_{cp} phase space can be eliminated. Figure 2.7(c) and Figure 2.7(d) show that by adding reactor experiment constraints on θ_{13} a measurement of δ_{cp} can be further improved.

(a) 100% ν-mode.

(b) 50% ν-, 50% $\bar{\nu}$-mode.

(c) 100% ν-mode, with ultimate reactor constraint.

(d) 50% ν-, 50% $\bar{\nu}$-mode, with ultimate reactor constraint.
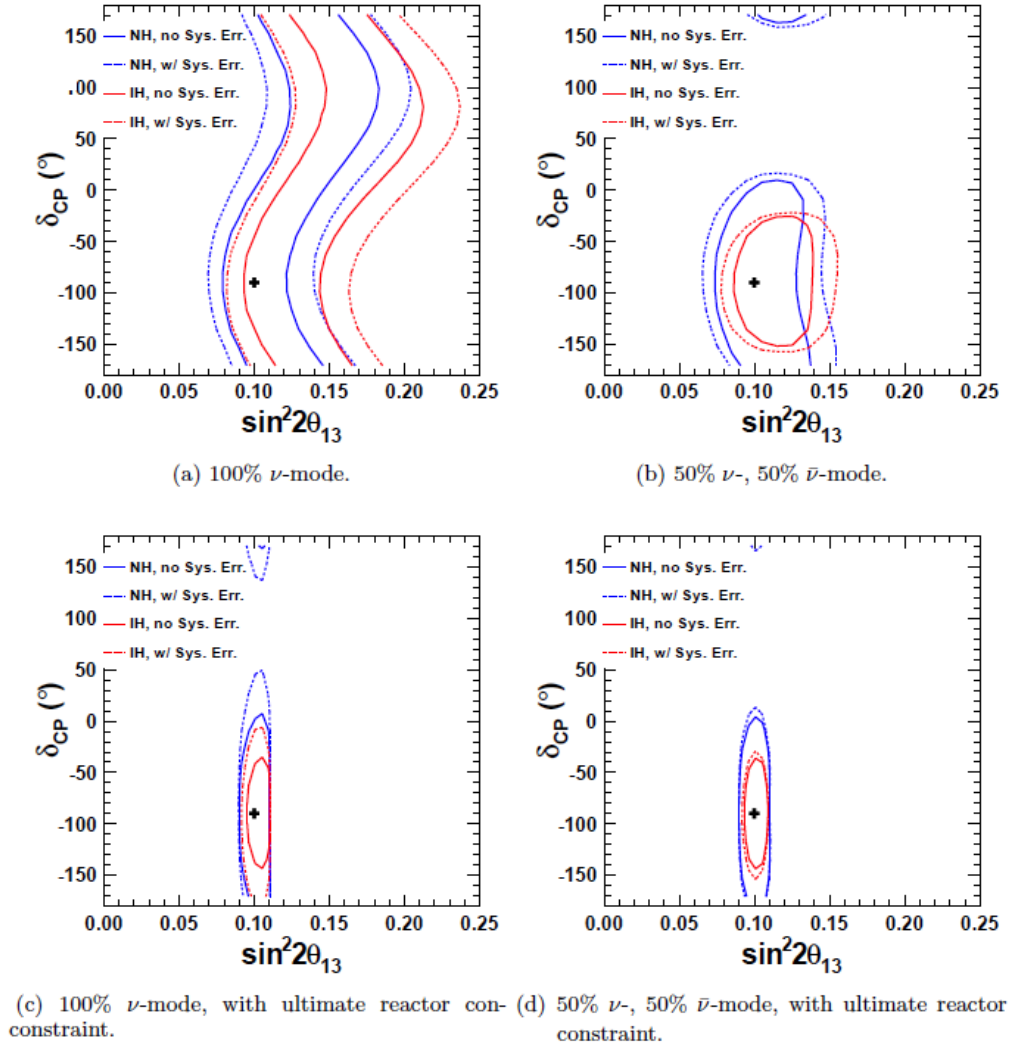
Figure 2.7: The expected T2K sensitivity for θ_{23} and δ_{cp} for 7.8×10^{21} POT. The black cross represents the input oscillation parameters. The systematic uncertainties included are those established for the 2012 oscillation analyses [50].

2.5   Neutrino Interactions at T2K

When neutrinos interact with matter they do so using the weak force which can propagate via either the W or Z bozons. As the Z boson is uncharged and the W bozon is charged we refer to their interactions as Neutral-Current (NC) interactions and Charged-Current (CC), respectively. When neutrinos interact via NC interactions, the neutrino does not change state (Figure 2.8 right) and so it is impossible to determine its flavour. When neutrinos interact via CC interactions (Figure 2.8 left), however, the neutrino is changed to its corresponding charged-lepton flavour partner. This allows us to determine the flavour of the original neutrino whenever CC interactions occur by identifying the flavour of the lepton produced. This work focuses on CC interactions. Feynman diagrams for NC and CC interactions can be seen in Figure 2.8.
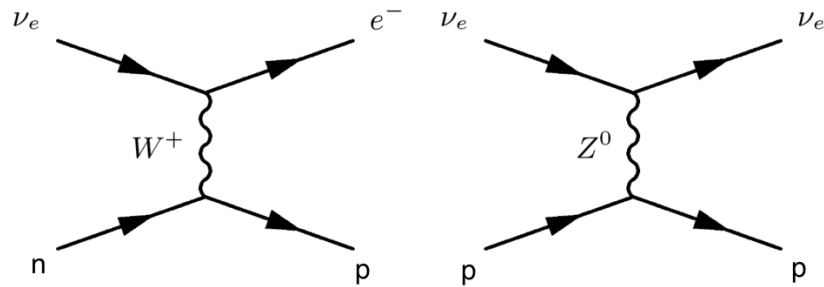
Figure 2.8: The Feynman diagrams for Charged-Current (left) and Neutral-Current (right) neutrino interactions. Initial states are shown on the left and final states on the right. [51]

Neutrino interactions are further subdivided into Quasi-Elastic (QE), Resonant (RES) and Deep Inelastic Scattering (DIS) interactions. CCQE interactions are the simplest of the CC neutrino interactions and are dominant at neutrino energies less than 1 GeV. In CCQE interactions the neutrino does not have enough energy to break a nucleon apart and so is effectively acting on the nucleon as a whole. This produces a single lepton which matches the flavour of the interacting neutrino and often results in the ejection of the nucleon involved. CCQE is dominant at T2K for energies below 1 GeV as seen in Figure 2.9(a) for neutrinos and Figure 2.9(b) for antineutrinos. At higher energies between 1 GeV and 5 GeV in neutrino interactions and between 1 GeV and 8 GeV in antineutrino interactions the CCRES process becomes dominant. As in the CCQE case, there is still not enough energy to break the nucleon apart; however, there is now enough energy to promote the nucleon to a higher energy state. For example protons can be excited to a Δ^+ state in neutrino CCRES interactions and neutrons can be excited to a Δ^0 in antineutrino CCRES interactions. These Δ baryons, then rapidly decay to produce a pion and proton or neutron as shown in Equations 2.14 and 2.15.

$$\Delta^+ \rightarrow n + \pi^+ \tag{2.14}$$

$$\Delta^0 \rightarrow p + \pi^- \tag{2.15}$$

The most energetic process is CCDIS which becomes the dominant process above 5 GeV for neutrino interactions and above 8 GeV for antineutrino interactions. In this interaction the neutrino has enough energy to directly interact with individual quarks inside the nucleons, which results in an energetic hadronic shower of several particles.
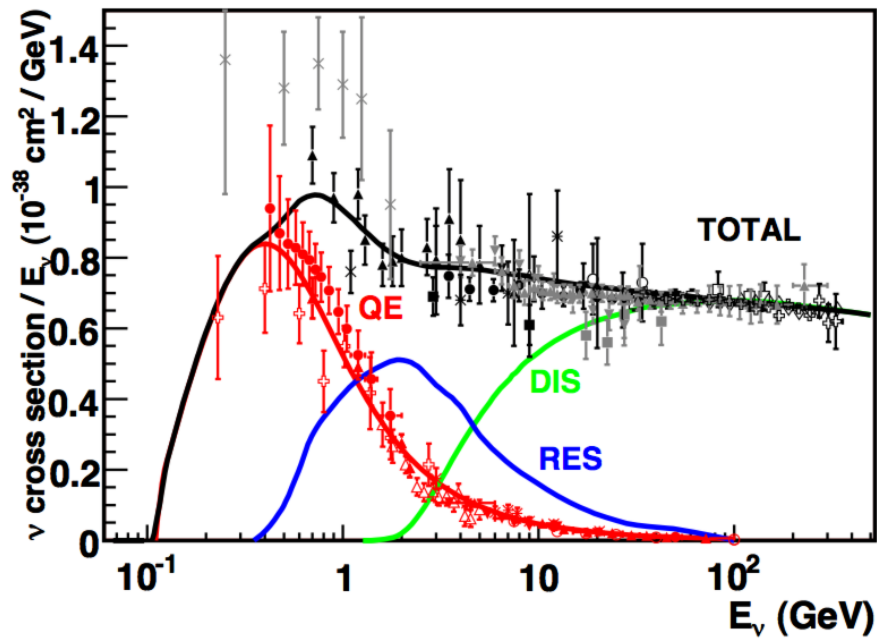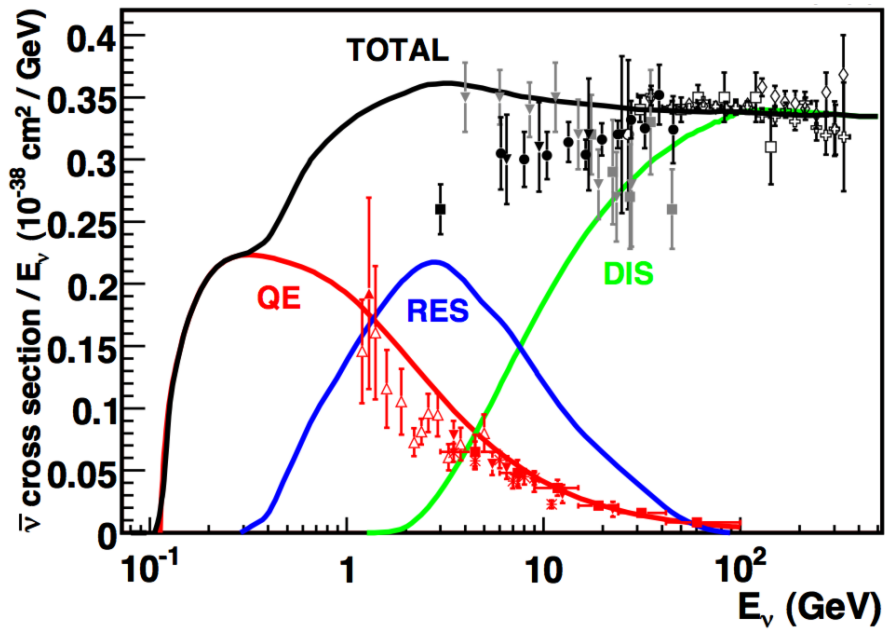
Figure 2.9: The cross sections for ν_μ (a) and $\bar{\nu}_\mu$ (b) of varying energies. The variation of the cross sections of the three processes are shown with CCQE in red, CCRES in blue and CCDIS in green. The black line shows the total cross section per nucleon. The curves are theoretical with the points being experimental measurements from multiple experiments: see Reference [51] for details.

Chapter 3

T2K Experiment

The Tokai to Kamioka (T2K) experiment (Figure 3.1) is a long-baseline neutrino oscillation experiment. The main objectives of the T2K experiment are [52]:

- Measure the θ_{13} mixing angle by looking for ν_e appearance in a ν_μ beam.

- Improve the precision on Δm_{23}^2 and θ_{23} by investigating ν_μ disappearance.

- Search for potential oscillations of sterile neutrinos.

In order to achieve these aims, a ν_μ beam is produced at the Japanese Proton Accelerator Research Complex (J-PARC) and is aimed at the far detector, Super-Kamiokande (SK), 295 km away in the Kamioka mountains. The ν_μ beam is monitored by two near detectors: the on-axis INGRID and the off-axis ND280, both of which are 280 m from the neutrino production target. This chapter covers the T2K experiment. The beam is described in Section 3.1, the near detectors INGRID and ND280 are described in Sections 3.2.1 and 3.2.2, respectively. The far detector SK is described in Section 3.3.

The T2K experiment measures neutrino oscillations by first using the ND280 to measure the neutrino flavour composition of the unoscillated neutrino beam, and then using SK to measure the neutrino flavour composition of the oscillated

neutrino beam. The neutrino parameters are then calculated by ν_e appearance measurements where more ν_e are present in the beam after oscillation, or by ν_μ disappearance measurements where less ν_μ are present in the beam after oscillation.

The T2K experiment was the first experiment to show evidence for ν_e appearance in a ν_μ beam [53] and has measured $\sin^2(2\theta_{13}) = 0.14 \pm 0.03$ [54]. The experiment has also measured Δm_{23}^2 and θ_{23} via observation of ν_μ disappearance, with the measurement of θ_{23} being the world's best measurement [35]. In 2014 the T2K experiment began running with an antineutrino beam in order to investigate CP violation in the lepton sector.
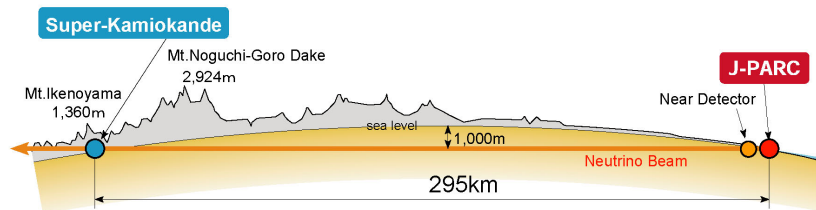
Figure 3.1: An overview of the T2K experiment. J-PARC (right) where the beam is created is shown as a red dot, the near detector complex is shown as an orange dot and SK is shown as a blue dot (left). The beam travels from the east coast of Japan to the western mountains [52].

3.1 Beam Generation

The T2K neutrino beam is produced at the J-PARC facility in Tokai, where H^- ions are accelerated to 400 MeV by a linear accelerator (LINAC). These ions are then stripped of their charge to create H^+ ions (protons) and are injected into a 3 GeV rapid-cycling synchrotron which in turn feeds the protons into the J-PARC main ring which accelerates the protons up to an energy of 30 GeV [52]. Figure 3.2 shows an aerial view of the J-PARC facility.
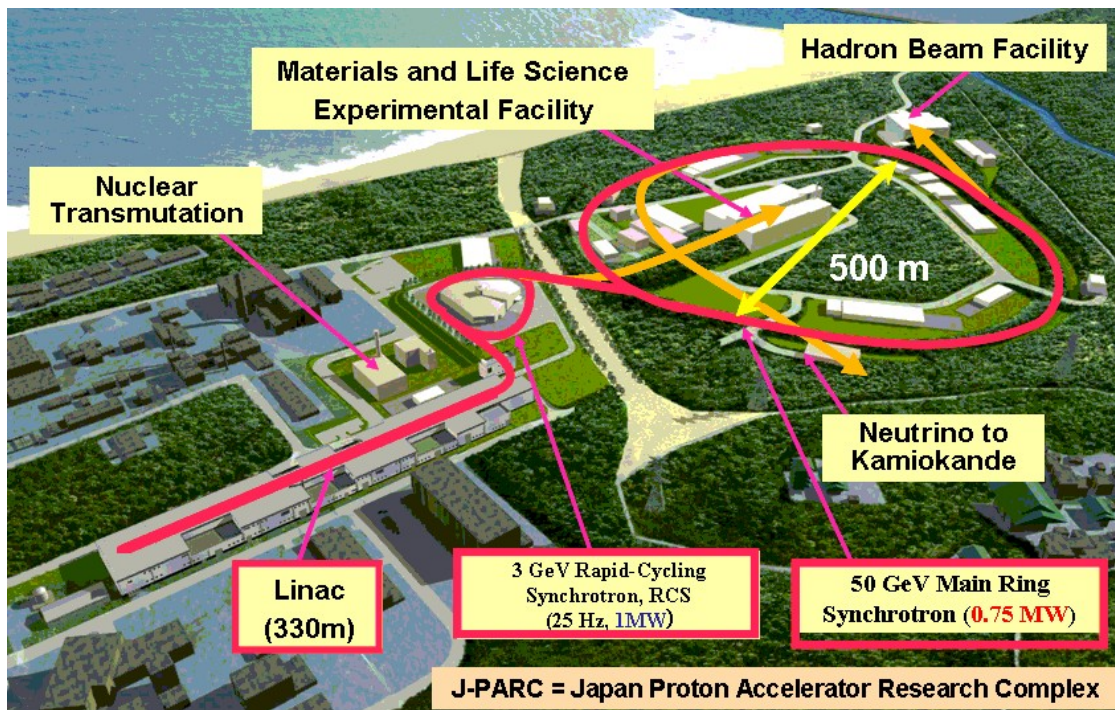
Figure 3.2: An aerial simulation of the J-PARC facility. The path of the protons from the LINAC through the Rapid-Cycling Synchrotron and finally the Main Ring Synchrotron is shown in pink. Where the beam is extracted for various experiments is coloured in orange. The neutrino beam is extracted on the bottom portion of the main ring. The main ring has a theoretical maximum energy of 50 GeV but is currently operating with an energy of 30 GeV [55].

The protons at this point consist of eight bunches which are extracted from the main ring to form a single spill. The resulting time distribution carries through to the neutrino beam, as can be seen in the time distribution seen in Figure 3.3
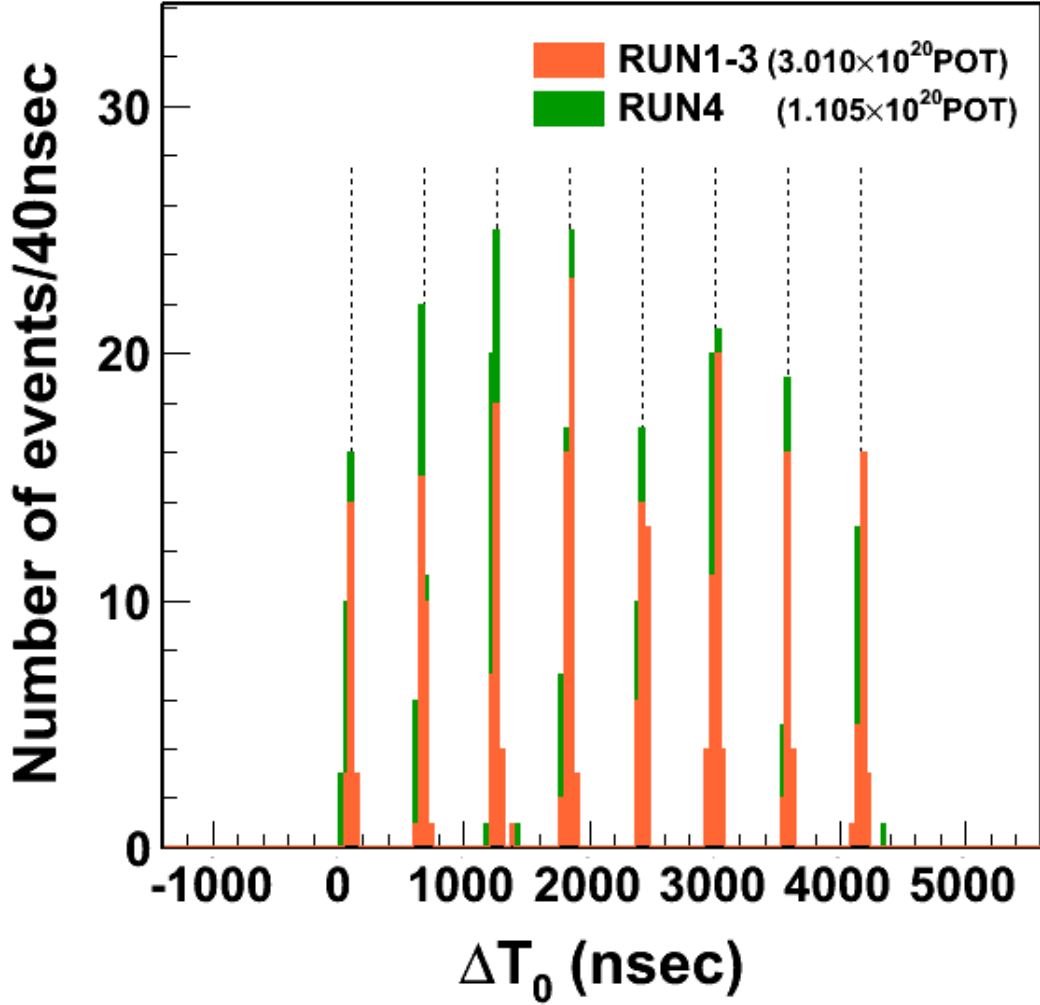
Figure 3.3: The distribution in time of neutrino events, and the bunch structure of a T2K spill at SK. The dashed lines show the centre of each bunch and zero on the time axis corresponds to the time at which the start of the pulse arrives at SK [56].

which shows the time distribution of neutrino interactions at SK. When running at the projected peak beam power of 0.75 MW, this corresponds to 3.3×10^{14} protons per spill [56]. This proton spill is directed onto a target to produce a shower of particles. The target is a 2.6 cm-diameter graphite rod which is 91.4 cm in length. A denser material than graphite would be destroyed by the heat shock of the proton beam. Charged pions are selected from the shower of particles by a series of focusing horns. A schematic diagram of the beam components is shown

in Figure 3.4, with protons striking the target on the left and the SK detector on the right.
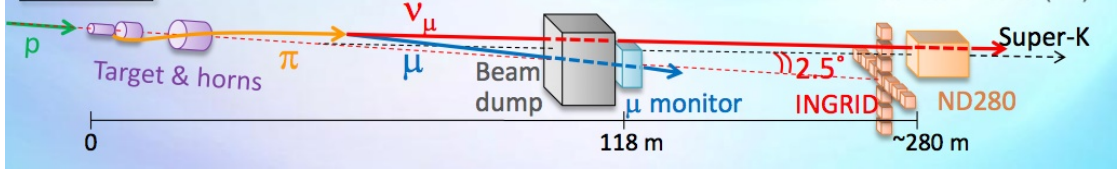
Figure 3.4: The process T2K uses to generate its ν_μ beam, starting from a 30 GeV proton beam [57].

To ensure the greatest focusing efficiency, three magnetic horns are employed. In neutrino beam mode the first horn, which surrounds the target, collects the positive pions and kaons that are generated and focuses them in the general direction of the neutrino beam. The second and third horns focus these particles into a concentrated beam. This has the effect of increasing the neutrino flux at SK by a factor of approximately 16 when running the horns at a current of 320 kA compared to a current of 0 kA. The horns also defocus any contaminating particles, such as negatively charged pions and kaons, the decay products of which would contaminate the ν_μ beam.

The products of the proton interaction that have been focused by the horns then enter the decay volume where the positive pions decay to positive muons and muon neutrinos, as shown in Equation 3.1.

$$\pi^+ \rightarrow \mu^+ + \nu_\mu \qquad (3.1)$$

These pion decays give T2K its ν_μ beam. By reversing the polarity of the magnetic horns negative pions will be focused and positive pions defocused, which results in the decay shown in Equation 3.2.

$$\pi^- \rightarrow \mu^- + \bar{\nu}_\mu \qquad (3.2)$$

This decay produces negative muons and muon antineutrinos, which allows T2K to also run with a $\bar{\nu}_\mu$ beam.

However, if the muons in either Equation 3.1 or 3.2 decay, they will produce contaminating flavours of neutrinos as shown on the right hand side of Equation 3.3.

$$\mu^+ \rightarrow e^+ + \bar{\nu}_\mu + \nu_e \tag{3.3}$$

In order to range out all of the remaining hadrons and the muons before they can decay as in Equation 3.3, there is a beam dump starting 109 m from the target consisting of 3.1 m of graphite and 2.4 m of iron. It is capable of stopping all hadrons and any muons with momenta less than 5 GeV/c. Muons with momenta greater than 5 GeV/c reach the muon monitor (shown in Figure 3.4) which is used to measure the position of the neutrino beam. The muon monitor is capable of measuring the muon profile to a precision of 0.25 mrad (3 cm) [52]. The neutrino beam then passes through approximately 150 m of rock, removing all of the muons, before it reaches the ND280 complex which is discussed in Section 3.2.

The charged kaons that remain after the focusing horns and enter the decay volume also introduce contamination into the neutrino beam, although there is an order of magnitude fewer kaons than pions after horn focusing, as shown in Figure 14 of [56]. The contamination arises due to the decay shown in Equation 3.4.

$$K^+ \rightarrow e^+ + \nu_e + \pi^0 \tag{3.4}$$

	ν_μ	$\bar{\nu}_\mu$	ν_e	$\bar{\nu}_e$
Neutrino beam mode	92.6%	6.2%	1.1%	0.1%
Antineutrino beam mode	37.5%	60.1%	1.4%	1.0%

Table 3.1: The flavour composition of the T2K beam for neutrino and antineutrino beam modes.
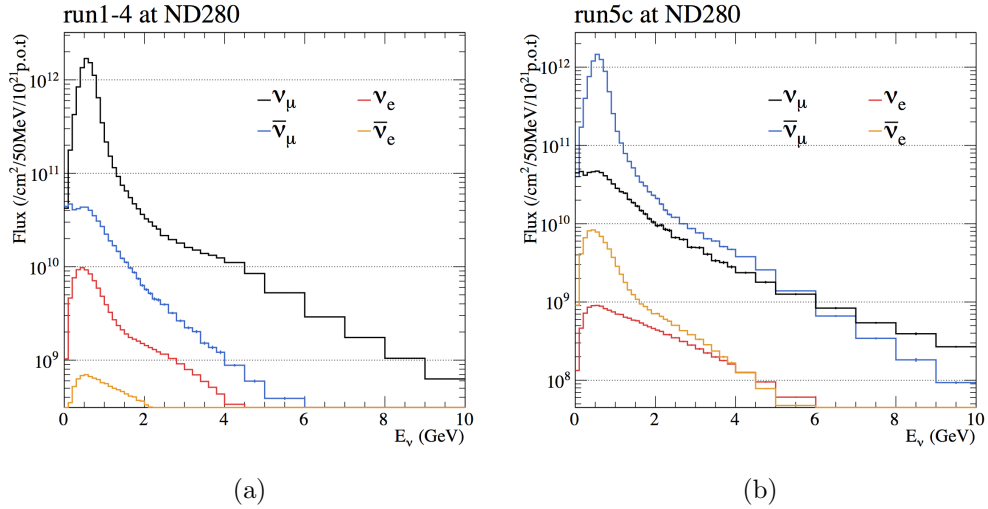
Figure 3.5: The beam compositions for neutrino (a) and antineutrino (b) beam modes as a function of energy. In neutrino mode the beam is highly pure in ν_μ; however, in antineutrino mode the beam has a large background from ν_μ as well as approximately 1% ν_e and $\bar{\nu}_e$ [58]. The full breakdown of the flavour content can be seen in Table 3.1.

When running in neutrino beam mode, the neutrino interactions in the ND280 are approximately 93% ν_μ; however, when running in antineutrino beam mode, the interactions in the ND280 are far less pure with approximately 60% of the neutrino interactions being $\bar{\nu}_\mu$, the desired primary component [58]. There are several reasons for this difference:

- The interaction cross section of neutrinos on matter is approximately a factor of 3 larger than the interaction cross section for antineutrinos on matter [51].

- The interactions of protons on the carbon target to produce pions has a charge asymmetry and so is biased towards the production of π^+ which decay to produce neutrinos over π^- which decay to produce antineutrinos [59].

The breakdowns by neutrino flavour for neutrino beam mode and antineutrino beam mode are shown in Figure 3.5 and in Table 3.1.

While both the processes shown in Equations 3.3 and 3.4 introduce ν_e contamination into the neutrino beam, the negative charge equivalent decays shown in Equations 3.5 and 3.6 introduce $\bar{\nu}_e$ contamination into the antineutrino beam.

$$\mu^- \rightarrow e^- + \nu_\mu + \bar{\nu}_e \tag{3.5}$$

$$K^- \rightarrow e^- + \bar{\nu}_e + \pi^0 \tag{3.6}$$

In normal beam mode where negatively-charged particles are rare, the $\bar{\nu}_e$ contamination is below the 1% level; however, when operating in antineutrino beam mode where the horn focuses negative pions to create a beam that is predominantly $\bar{\nu}_\mu$, the $\bar{\nu}_e$ contamination becomes an issue. When the neutrino beam is measured at SK the $\bar{\nu}_e$ contamination will be indistinguishable from an oscillated $\bar{\nu}_e$ that was produced as a $\bar{\nu}_\mu$. For this reason a measurement of the $\bar{\nu}_e$ contamination using the ND280 is essential.

The T2K beam is designed so that the ND280 and SK detectors lie slightly off the central axis of the neutrino beam. Neutrinos that travel down the central axis of the neutrino beam have a wide distribution of energies. However, due to the kinematics of pion decay, the off-axis neutrino energy is spread across a relatively narrow spectrum. The angle of 2.5 degrees used in the T2K experiment gives a median beam energy of 600 MeV, which for a distance of 295 km results in the maximal probability of oscillations. Figure 3.6 shows the energy distribution at T2K for the on-axis beam and several off-axis beam angles.

The protons on target (POT) accumulation of the T2K experiment with time is shown in Figure 3.7, where neutrino mode running periods are shown in red and antineutrino mode running periods are shown in purple; the total integrated beam power is shown in blue. The total POT for each run is shown in Table
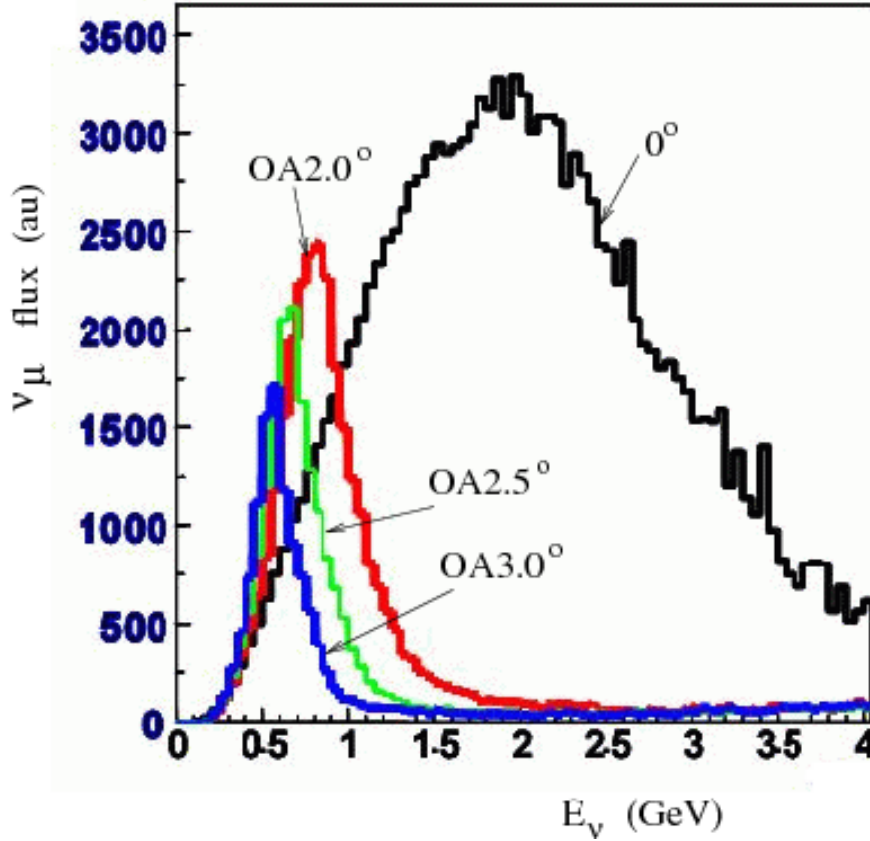
Figure 3.6: The change in the neutrino beam energy distribution as the off-axis angle changes. The black line represents an on-axis beam while the green line shows the T2K off-axis energy distribution. The blue and red lines show 0.5 degree differences from the T2K off-axis angle with 3 degree and 2 degree off-axis angles respectively. The ordinate axis is in arbitrary units [60].

3.2. The large break between runs 2 and 3 (March 2011 to February 2012) is due to a shutdown forced by the 2011 earthquake. The earthquake caused significant damage to both the J-PARC facility and the ND280. The large break between runs 4 and 5 (May 2013 to May 2014) was caused by shutdown of the J-PARC facility due to a radioactive material leak at the hadron hall facility. In the analysis presented in this thesis antineutrino data from run 5 and 6 is used.
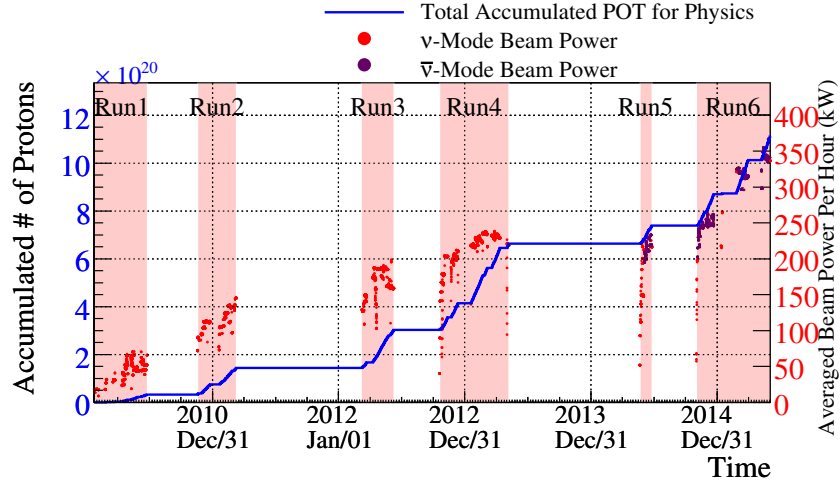
Figure 3.7: The proton on target (POT) accumulation of the T2K experiment with time. Neutrino mode running periods are shown in red and antineutrino mode running periods are shown in purple; the total integrated beam power is shown in blue, and the total POT for each run is shown in Table 3.2.

T2K Run	Run Period	Total POT ($\times 10^{20}$)
1	19th March 2010 - 26th June 2010	0.311
2	18th November 2010 - 11th March 2011	1.12
3	27th February 2012 - 9th June 2012	1.59
4	19th October 2012 - 8th May 2013	3.60
5	21st May 2014 - 26th June 2014	0.75
6	1st November 2014 - 3rd June 2015	3.75

Table 3.2: The total POT and running period for each of the T2K runs.

3.2 ND280 Complex

3.2.1 INGRID

The Interactive Neutrino GRID (INGRID) [61] is the on-axis beam monitor used by T2K to measure the neutrino beam direction, on-axis flux and profile. INGRID is made up of 16 identical $1.2\times1.2\times1.2$ m^3 modules each of which has a sandwich structure of 9 $120\times120\times6.4$ cm^3 iron target plates and 11 tracking scintillator plates. Each of the scintillator plates is made up of 24 $5\times1\times120$ cm^3 vertical and horizontal scintillator bars [52]. The INGRID modules are arranged into 14 modules forming a cross, with 7 modules in both the vertical and horizontal directions. Two modules overlap in the centre in order to collect more data at the beam centre. The remaining two modules are both above the horizontal arm as shown in Figure 3.8.

The function of INGRID is to measure the neutrino beam direction and intensity via neutrino interactions in the iron, with enough data that at nominal beam intensity a daily measurement can be performed to good statistical precision. Using the total number of neutrino interactions in each module, the beam centre can be determined to a precision better than 10 cm which corresponds to an angular precision of 0.4 mrad [52]. INGRID also measures the beam stability and profile; a measurement of the T2K beam profile by INGRID can be seen in Figure 3.9.
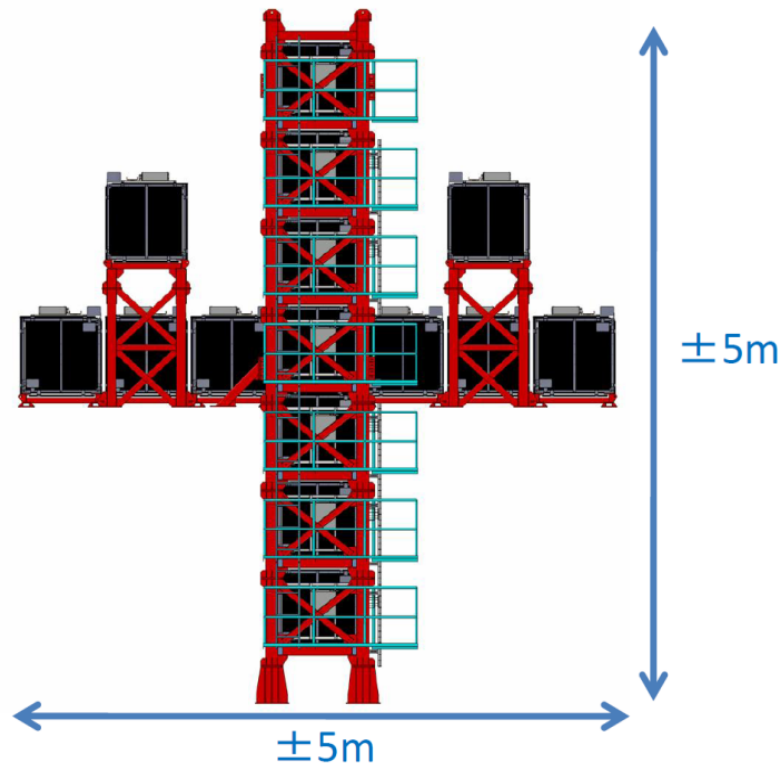
Figure 3.8: The INGRID detector with 7 modules making up both the horizontal and vertical arms. The remaining two modules are placed above the horizontal section [52].
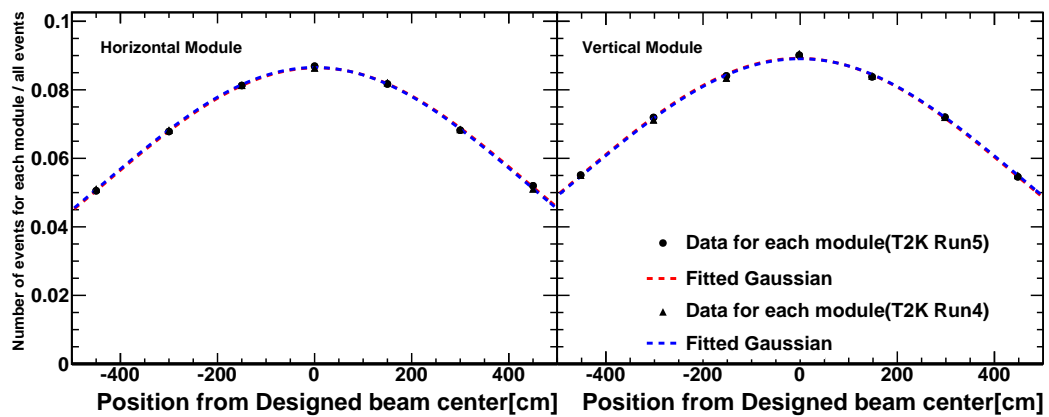
Figure 3.9: Measurements of the T2K beam profile in the horizontal (left) and vertical (right) directions by the INGRID detector. Both neutrino (run 4) and antineutrino (run 5) data are shown. It can be seen that both beam modes have a similar profile [61].

3.2.2 ND280

The ND280 measures the off-axis neutrino beam flux and composition and neutrino interaction cross sections. It is important that these quantities be measured so that the T2K experiment is able to reduce the systematic uncertainties in the neutrino oscillation measurements. The ND280 is made up of several subdetectors, shown in Figure 3.10 which shows an exploded view of the detector with the neutrino beam entering from the left. The tracking region of the detector is composed of three Time Projection Chambers (TPCs) interspersed with two Fine-Grained Detectors (FGDs), which are described in Sections 3.2.2.2 and 3.2.2.3. At the downstream end of the tracker region is the Downstream Electromagnetic Calorimeter (DsECal). At the upstream end of the detector is the Pi-Zero Detector (P0D) which is described in Section 3.2.2.5. The tracker region, the P0D and DsECal are inside a steel basket which is $6.5{\times}2.6{\times}2.5$ m^3. The P0D is then surrounded by the P0D Electromagnetic Calorimeter (P0DECal), and the tracker region by the Barrel ECal (BrECal) which are described in Section 3.2.2.4 along with the DsECal. All of this is inside the former UA1 0.2 T magnet which is covered in Section 3.2.2.1. Inside the gaps in the magnet yoke is the Side Muon Range Detector (SMRD) which is covered in Section 3.2.2.6.

3.2.2.1 Magnet

The magnetic field for ND280 is generated by the former UA1 magnet, also used by the NOMAD experiment, which was refurbished at CERN for the purpose of the T2K experiment. The magnet consists of 16 C-shaped yokes and 4 coils generating a dipole magnetic field of 0.2 T [62] in the horizontal plane, perpendicular to the ND280 central axis. During data-taking the two halves of the magnet are in the closed position fully enclosing the basket. The magnet yolk splits vertically as
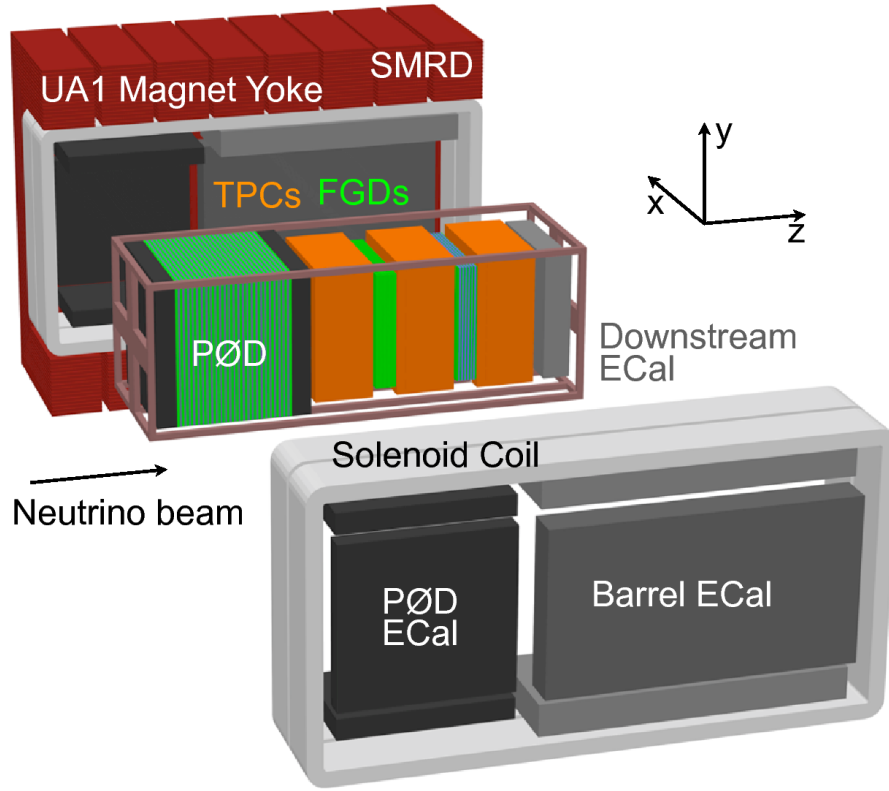
Figure 3.10: An exploded view of the ND280 showing the tracking region, the P0D and the DsECal inside the basket, with the P0D ECals and Barrel ECals surrounding it. The magnet is on the outside. In this image, the beam is coming from the left and the coordinate system is shown on the right [52].

shown in Figure 3.10 to allow access to the basket and the ND280 subdetectors for maintenance.

3.2.2.2   TPCs

The three TPCs [63] (coloured orange in Figure 3.10) are used for measuring particle momentum and the rate of energy loss due to ionisation (dE/dx), which are used in particle identification. The TPCs are $2.3 \times 2.4 \times 1.0$ m^3 boxes containing a drift gas, which is a mixture of 95% argon, 3% tetrafluoromethane and 2% isobutane [63]. This mixture was chosen for its low diffusion and good performance with the Micromegas readout modules. Each TPC is split in half by a central cathode that stands in the yz plane, as seen in Figure 3.11. The TPCs also have

extremely powerful three-dimensional imaging capabilities to identify the number of charged particles and their orientations as they traverse the subdetector. As can be seen from Figure 3.11, the TPCs are constructed from an inner box which holds the drift gas, and an outer box. The inner box also functions as a field cage, ensuring a uniform electrostatic field inside the TPC in order to transport ionisation electrons from their point of creation to the Micromegas modules with minimal distortion. Between the inner and outer boxes is carbon dioxide which is used as an insulating gas. When a charged particle passes through a TPC, ionisation electrons are produced. These electrons then drift away from the central cathode towards one of the readout plates where the Micromegas modules multiply the electrons thus amplifying the signal. Front-end electronic cards that plug into the back of the Micromegas modules digitise analog data and transmit the data out of the TPC. Each TPC is instrumented with 12 Micromegas modules on each side. Each side is split into pads (7.0 mm × 9.8 mm) arranged into 48 rows and 36 columns. All pads are in the same plane (yz) with the position of the particle in the third dimension (x) being calculated via the charge drift time.

The TPCs are capable of measuring a particle's position with a spacial resolution of approximately 1 mm depending on charge drift distance. The design goal of a single TPC, to measure the momentum perpendicular to the magnetic field to at least a precision of 0.1 $\mathrm{p_{perpendicular}}/(GeV/c)$, has been achieved. The TPCs were also required to be able to measure a particle's ionisation energy to 10% precision; this has been surpassed with the resolution being $7.8 \pm 0.2\%$ for minimum-ionising particles (MIP) [64].

3.2.2.3 FGDs

The FGDs [65] provide a target mass for neutrino interactions as well as precise tracking of charged particles coming from the interaction vertex. Both FGDs
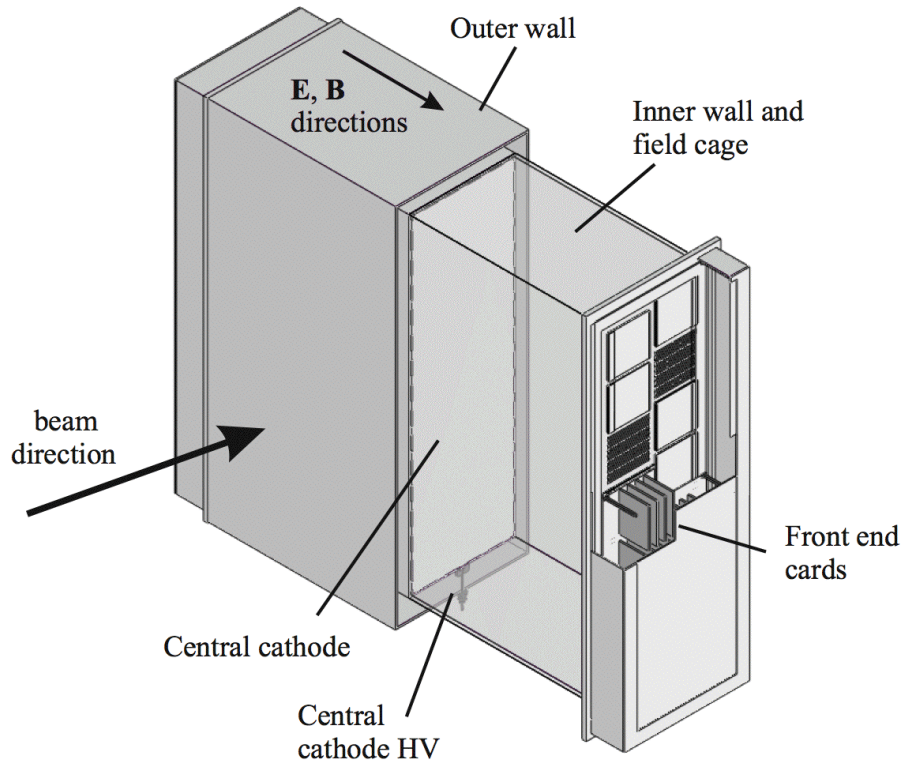
Figure 3.11: A cutaway view of a TPC module highlighting the main aspects of the design [63].

contain 1.1 tonnes of target material. The FGDs are constructed using 9.6 mm ×
9.6 mm cross-section plastic scintillator bars of length 1864 mm, arranged in layers
of 192 bars. The most upstream FGD (FGD1), shown in green in Figure 3.10, has
30 layers, with the bars in each subsequent layer being orientated alternating in
the x and y directions, giving 5760 scintillator bars in total. The second FGD
(FGD2), shown in blue and green in Figure 3.10, has 14 scintillator layers giving
2688 scintillator bars in total; however, between each pair of layers is a 2.5 cm
layer of water encased in polystyrene tubes (6 water layers in total) to allow for
comparisons between neutrino cross sections for carbon (plastic scintillator) and
oxygen (water). This gives a useful test of neutrino interaction theory as the
ratio of carbon and oxygen interaction cross sections is predictable. The neutrino

interaction cross section on oxygen is also necessary for predictions of the flux at SK. Each scintillator bar contains a Wavelength Shifting Fiber (WLS) running down its centre. The WLS fibre is used because the fibre has a much longer attenuation length than the scintillator, allowing the light produced by a charged particle in the scintillator bar to travel further and thus increasing the readout efficiency of the FGDs. One end of the WLS fibre is mirrored with aluminium and the other is attached to a Multi-Pixel Photon Counter (MPPC) [66], which digitises the light signal produced by the scintillator bar. The MPPC is an array of photodiodes that are optimised to detect light in the green part of the visible spectrum, which is the output wavelength of the WLS fiber [67]. MPPCs are used because, unlike photo-multiplier tubes (PMTs), they can function in a magnetic field. Each MPPC contains 667 (23 × 29) photodiodes or pixels, each of which act as independent binary counters. This is useful for minimising noise because if only a few pixels on an MPPC fire it is likely due to noise; whereas, if many pixels fire it is likely due to incident scintillation photons.

The FGDs supply the target mass for neutrino interactions in the ND280 tracker region and FGD information is used to determine where the neutrino interaction took place (the interaction vertex).

3.2.2.4 ECals

There are 13 ECal modules [67]: six in the P0DECal, six in the BrECal, and the DsECal. The DsECal is located inside the basket that contains the tracker region and P0D; whereas, the other 12 ECals are outside the basket, attached to the inside of the magnet. All ECal modules have similar construction in that they are all made of alternating sheets of lead and layers of plastic scintillator bars, but there are small differences between each of the sets of modules. In the Barrel the lead sheets are 1.75 mm thick with 31 layers for a total thickness of 9.7 radiation

lengths, in the DsECal there are 34 layers with 1.75 mm thick lead for a total thickness of 10.6 radiation lengths, and in the P0D ECal, which is not designed to be a tracking ECal, there are only six layers with 4 mm thick sheets of lead for a total thickness of 4.3 radiation lengths. For the DsECal and BrECal the bars in each successive layer are in alternating planes; however, the P0D ECals only have one orientation of bar (z). All ECal scintillator bars have a 1 cm × 4 cm cross section. Inside each of the scintillator bars is a WLS fibre that is read out by an MPPC [67].

In the DsECal where all bars are 2.04 m long, each of the 50 bars in a plane are read out by two MPPCs, one at each end of the bar. For the BrECals the bars in the z direction are 3.84 m long and, like the DsECal, are read out by an MPPC at each end. For the top and bottom modules the bars running perpendicular to the z direction (x) are 1.52 m long, and for the side modules the bars running perpendicular to the z direction (y) are 2.36 m long; however, all of these are read out by only a single MPPC with the uninstrumented end of the WLS fibre being mirrored like in the FGDs.

3.2.2.5   P0D

The main objective of the P0D [68] is to measure the cross section of NC neutrino interactions which produce π^0s, one of the main backgrounds for SK ν_e and $\bar{\nu}_e$ measurements. The P0D uses alternating x and y planes of plastic scintillator bars, each of which are read out by a WLS fibre. Unlike the other subdetectors, the scintillator bars in the P0D are triangle-shaped, which allows for better position resolution than square bars. As with FGD2, the planes of scintillator are interspaced with water bags; however, unlike FGD2, these bags can be filled and emptied allowing for a comparison between water-in and water-out measurements. There are also lead and brass sheets between the layers of scintillator so that the

two gamma rays coming from a π^0 decay in the P0D have a reasonable chance of interacting and thus being detected. The P0D is split into several sections or P0Dules:

- An upstream ECal-P0Dule comprised of scintillator and lead.

- An upstream water target comprised of scintillator, water bags and brass.

- A central water target comprised of scintillator, water bags and brass.

- A central ECal-P0Dule comprised of scintillator and lead.

The upstream and central ECals-PODules are identical with 7 layers of scintillator and lead; whereas, the upstream and central water targets differ slightly with the upstream target having 13 layers of brass, scintillator and water and the central water target having only 12 [52].

3.2.2.6   Side Muon Range Detector

The Side Muon Range Detector (SMRD) [69] is a collection of 440 scintillator modules, 192 horizontally oriented and 248 vertically oriented, inserted into the gaps in the magnet yoke surrounding the tracker region (see Figure 3.10). The SMRD modules measure 9 mm×686 mm×955 mm for horizontal modules and 9 mm×892 mm×955 mm for vertical modules. The SMRD also uses WLS fibres for readout. The SMRD is used to track cosmic rays and muons which are entering or escaping the detector at high angle with respect to the beam.

3.2.3   Data Distribution

T2K uses the LHC Computing GRID (LCG) for its data storage and processing. Data from the ND280 and INGRID is first transfered to the KEK Computing Centre in Japan, which is the T2K Tier 0 site, for archiving. The data is then

distributed to the Tier 1 sites at RAL in the UK and TRIUMF in Canada. From
the Tier 1 sites the data can then be downloaded to the Tier 2 sites such as
Lancaster for use in analyses. A diagram of this system can be seen in Figure
3.12. Large processing jobs such as Monte Carlo productions (Section 4.1) are
distributed across many GRID sites though processing of the raw data through
the software is currently performed at TRIUMF [70].

The upload to the KEK Computing Centre is managed by a set of Perl scripts
which require periodic monitoring to ensure that all files are uploaded to the GRID
and that no data is lost unnecessarily.
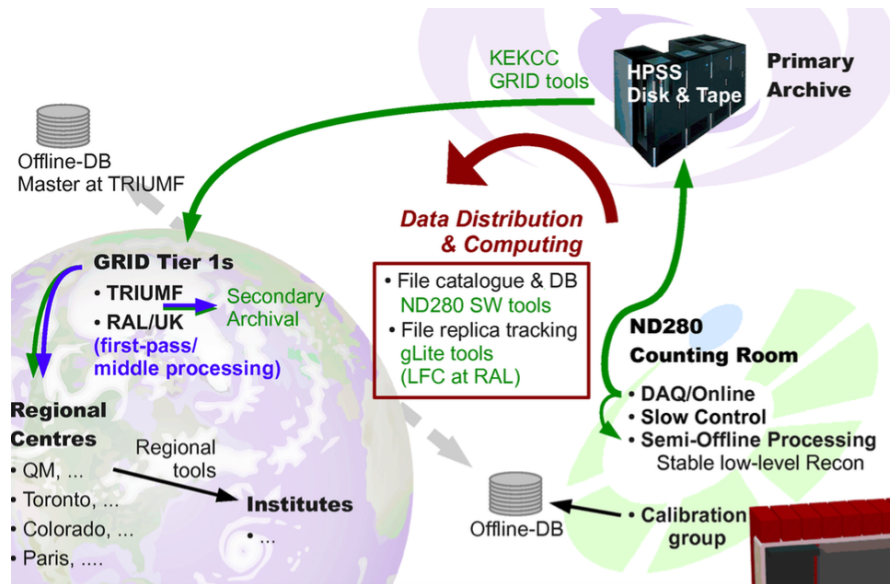
Figure 3.12: The implementation of the T2K GRID storage system. Data is first
archived at the KEKCC site before being distributed to the Tier 1 sites at RAL
and TRIUMF. From the Tier 1 sites the data can then be downloaded to the Tier
2 sites such as Lancaster for use [70].

3.3   Super-Kamiokande

Super-Kamiokande (SK) is the far detector for T2K located 295 km from the beam target and 2.5 degrees away from the beam axis. It is the successor to the Kamioka Nucleon Decay Experiment and in addition to functioning as a neutrino detector, SK continues to look for proton decays [71]. The detector is located in the Kamioka mine as the surrounding mountain provides 1000 m of rock overburden (equivalent to 2700 m water overburden) which reduces the background from cosmic ray muons by a factor of 100000. The detector is a cylindrical water-Cherenkov detector measuring 39.1 m in diameter and 41.4 m in height. SK contains 50 kton of pure water which is split into two volumes, an inner detector and an outer detector. The inner detector, which measures 33.8 m in diameter and 36.2 m in height, is instrumented with 11129 inward-facing 50 cm PMTs. The outer detector is instrumented with 1885 20 cm PMTs which face outwards from the same frame as the inner detector. The inner detector is lined with black plastic to prevent light from scattering in the inner detector or from entering the inner detector from the outer detector. The inner detector volume contains 35 kton of pure water. A cutaway of the SK detector can be seen in Figure 3.13. ν_e and ν_μ are identified in SK if they interact and produce charged particles. In particular, CC interactions result in the production of muons or electrons from ν_μ and ν_e, respectively.

When a charged particle passes through the water in SK at a velocity which exceeds the speed of light in the water, the particle produces Cherenkov radiation which is detected by the PMTs. This radiation is emitted at angle determined by:

$$cos\theta = \frac{1}{n\beta} \tag{3.7}$$

where n is the refractive index of the medium and $\beta = v/c$, with v as the speed of the particle and c is the speed of light in a vacuum. For relativistic particles in

water, the light is emitted at an angle of 42 degrees. Electrons and muons can be distinguished from each other by the patterns the Cherenkov radiation creates in the inner detector:

- Electrons scatter easily because of their small mass, producing a fuzzy-edged ring as can be seen in Figure 3.14(a).

- Muons in contrast have a mass 210 times greater than an electron and thus rarely scatter, producing a sharp-edged, well-defined ring as seen in Figure 3.14(b).

This effect is further enhanced by muons being MIPs and thus rarely having highly-energetic interactions; whereas, electrons have a high probability to induce an electromagnetic shower thus producing multiple overlapping "fuzzy" Cherenkov rings [72].

The main background to electron and positron identification, and therefore to ν_e and $\bar{\nu}_e$ identification, is due to interactions which produce π^0s. π^0s rapidly decay into two gamma rays, producing an electromagnetic shower and subsequent radiation that cannot be distinguished at SK from electrons or positrons. If one of the two gamma rays from the π^0 is not reconstructed or the two gamma rays are so close together that they are reconstructed as a single object, a single fuzzy ring is observed which mimics the ν_e or $\bar{\nu}_e$ signal of an electron or positron. For this reason, improving the knowledge of π^0 production via neutrino interactions on water is a high-priority goal for the ND280 detector.
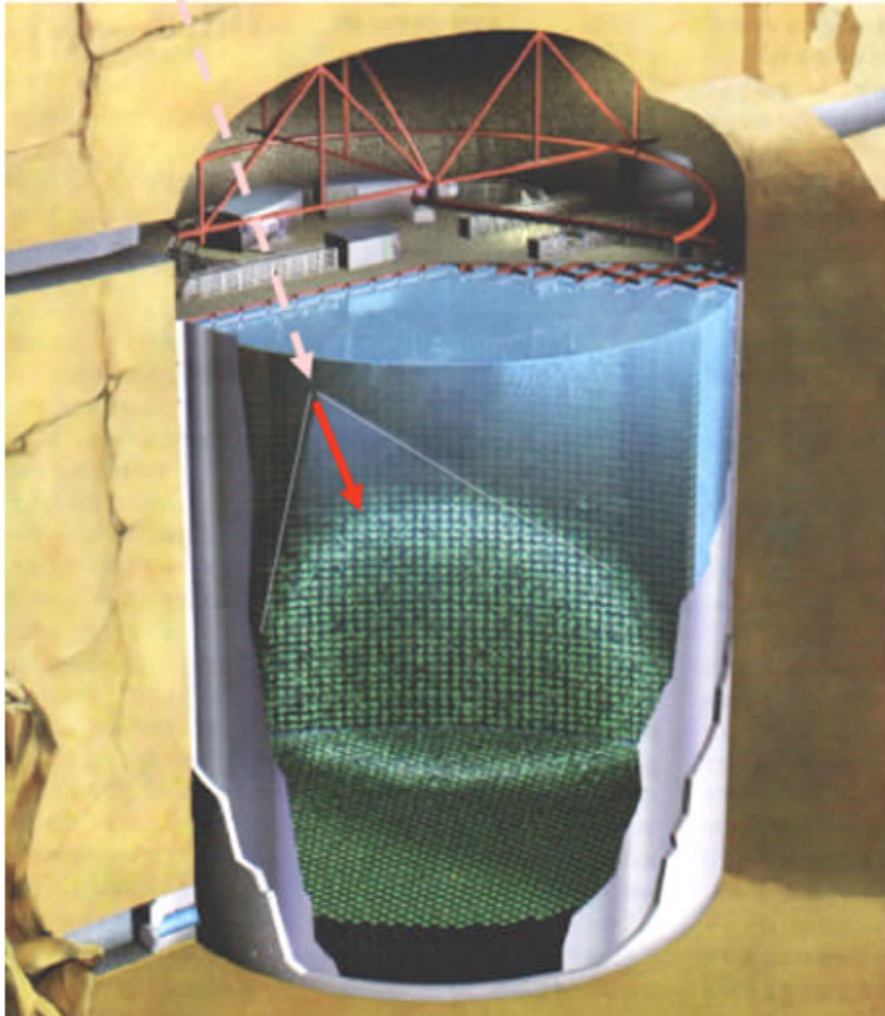
Figure 3.13: A cutaway view of the Super-Kamiokande water-Cherenkov detector, showing a projection of the Cherenkov ring from a particle onto the PMT wall.

(a)

(b)
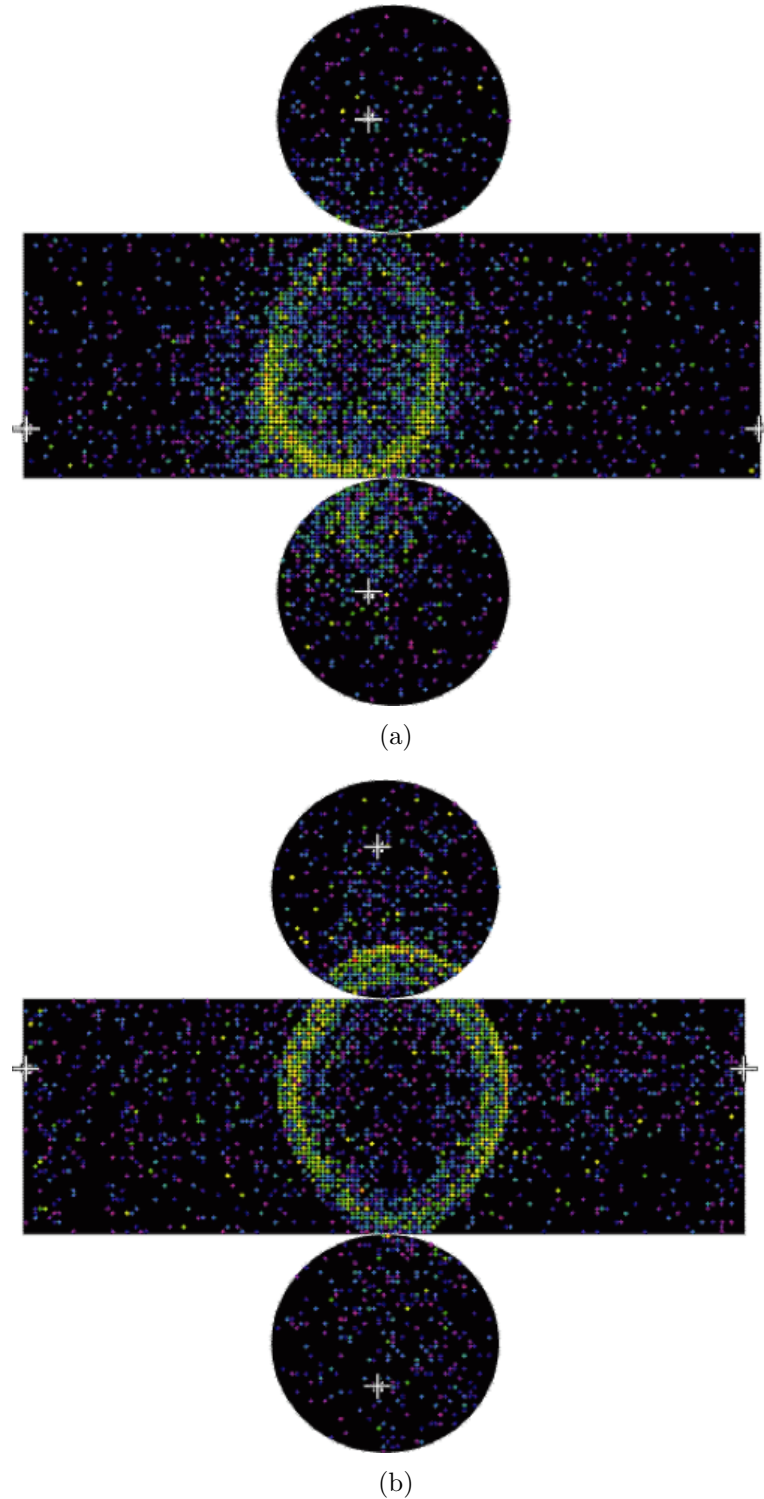
Figure 3.14: Event displays for the Super-Kamiokande detector. Figure (a) is a ν_e candidate event and Figure (b) is a ν_μ candidate event. As SK is unable to discriminate between positive and negative particles, neutrino and antineutrino interactions of the same flavour will look identical.

Chapter 4

Analysis

In this Chapter, a measurement of the contamination in the T2K beam from $\bar{\nu}_e$ will be presented. This is important to measure as it will help to constrain the systematic uncertainties present during T2K oscillation analysis. In neutrino beam mode, this $\bar{\nu}_e$ contamination in the $\nu_\mu \to \nu_e$ measurement was not a priority because the contamination was negligible; however, now that T2K is running in antineutrino mode, the contamination from $\bar{\nu}_e$ is predicted to be approximately 1% and so needs to be evaluated as can be seen in Figure 3.5(b).

It is important for the T2K experiment to take data in both neutrino and antineutrino beam modes as this allows for much tighter constraints to be placed on the phase space of δ_{CP} than if just neutrino or antineutrino data are used [50]. This maximises the physics potential of the T2K experiment.

In this work, we measure the $\bar{\nu}_e$ contamination in the antineutrino beam mode via a selection for $\bar{\nu}_e$ CC interactions, which can be identified by a final state positron. Prior to this work, a T2K ND280 ν_e selection was developed [73, 74] that began by identifying the electron created via a ν_e CC interaction as shown in Figure 2.8. In order to create a $\bar{\nu}_e$ CC selection, the existing ν_e selection was used as a starting point. Minimal changes to the ν_e CC selection were required in

order to select $\bar{\nu}_e$ events instead of ν_e as only one criterion in the ν_e CC selection takes into account the charge of the final state particles. These changes and the criteria shared with the ν_e CC selection are detailed in Section 4.2.

After applying criteria from the ν_e CC selection with a charge change to look for e^+ instead of e^-, a significant background from protons remained in the $\bar{\nu}_e$ sample; therefore, additional criteria were developed to minimise this background as discussed in Section 4.3.2. After the new criteria are applied to the sample, the main background in the sample is from misidentified gamma rays, discussed in Section 4.5.2; the remaining proton contamination is the second-largest background and is discussed in Section 4.5.1. Backgrounds not falling into these two categories are discussed in Section 4.5.3.

4.1 Data and Monte Carlo Simulations

4.1.1 Monte Carlo Simulation

Monte Carlo simulations are used extensively throughout particle physics. They allow our understanding of particle production (MC generators) and interactions (MC prediction) to be tested against data. The T2K experiment uses two neutrino interaction generators, NEUT [75] and GENIE [76], to simulate the complex physics which takes place when a neutrino scatters off a nucleon. NEUT is the primary generator for T2K with GENIE being used as a cross-check. In this analysis, all MC particles were generated with NEUT. First, a simulation of the proton beam's interaction with the carbon target that tracks the resulting particles, including neutrino parents and their decays (see Section 3.1), is produced using FLUKA2011 [77]. This simulation is then used to predict the flux of neutrinos at the ND280 [78]. This flux simulation is initially produced using data from the NA61 experiment [79] and is then reweighted using the differences between

the measured and simulated beam profile at T2K. The reweighting applied in this selection is the 13a flux reweighting, which was produced in October 2014. Once the flux of neutrinos arriving at the ND280 has been simulated, the neutrino interactions are generated with the NEUT package which determines where in the detector the simulated neutrino interacts, and what the products of the neutrino interaction are. Multiple neutrino interactions are combined into a simulated beam spill and the Geant4 [80] energy-deposition simulation toolkit is used to simulate the passage of particles through the ND280. The output of the Geant simulation is then run through dedicated T2K software, elecSim, to simulate the electronic responses of the detector. From this point, the generated MC is processed in the same way and using the same software as the real data collected by the ND280.

4.1.2 T2K Data

Both the data and MC are processed using the oaUnpack program to convert the Midas file produced by the ND280 Data Acquisition (DAQ) system into an oaEvent file for processing. The data and MC are then processed through oaCalib which applies calibration to the files. The reconstruction for the data and MC is handled by oaRecon (see Section 4.1.3) which generates particle tracks and showers from the measured hits (triggered Micromegas pads in the TPCs or scintillator bars with triggered MPPCs in the ECals and FGDs), or the deposition of energy in the detector. A stripped-down version of the oaRecon output is then produced by oaAnalysis which summarises the reconstruction and MC "truth" (unreconstructed) information in an analysis file. This process can be seen in a flow diagram in Figure 4.1.

The data used in this selection comprises antineutrino data collected up to 29th November 2014 and was processed with production 6C of the T2K software. The MC was processed with production 6B. 6C contains updated data calibration

compared to 6B; however, this does not affect the MC. The total data protons-on-target (POT) which passed data quality checks was 9.549×10^{19}. 2.505×10^{19} of the POT was from run 5 and the remaining 7.044×10^{19} POT was from run 6. The total simulated POT used was 1.0×10^{21}.

4.1.3 ND280 Reconstruction

The ND280 reconstruction is performed in two stages. First local reconstruction groups hits from each subdetector together into tracks and showers then the Global reconstruction merges the individual subdetector outputs to form a complete event. The first subdetectors reconstructed are the TPCs which group the Micromegas pads by the time their charge was above the noise threshold and then grouping neighbouring pads into clusters to form a track. Two of the dimensions of the track are provided by the positions of the Micromegas pads. The third dimension is found by comparing the time the charge was detected with the times from matching objects in the FGDs and ECals and then accounting for drift velocity and diffusion. This is done separately for each of the three TPCs.

The FGD reconstruction occurs in two stages; One stage involves matching the FGD hits to the reconstructed TPC tracks using a Kalman filter to match layers beginning with the layer closest to the TPC, if no hits are found in two consecutive layers the fitter stops. The other method using only FGD hits then uses any hits that were not used in the TPC-FGD matching stage are grouped into two 2D sets of XZ and XZ which then use a Radon transform to identify track-like clusters. These two 2D projections are then combined to see if they constitute a 3D XYZ track.

The ECal reconstruction is different from the FGDs and TPCs reconstruction. Because the high density lead can cause particles to shower both the track and shower reconstruction hypothesis must be considered. As with the FGD re-

construction the hits are first grouped into two 2D sets of hits which are then combined into a 3D cluster. The cluster is then examined based on the shape and charge distribution of the 3D cluster and assigned either track-like (long and thin with uniform charge distribution) or shower-like (wide and spherical with non-uniform charge distribution) status.

The final stage of the reconstruction is to combine the outputs from all the subdetectors into a single global reconstruction. As the TPCs have the best spatial resolution they are used as the starting point for global fits in the tracker region and Kahlman filters are used to match reconstructed TPC tracks with reconstructed FGD tracks. These tracks are then matched to the other subdetectors of the ND280. Any time two objects are combined the new combined object is refitted as a single object using a Kalman filter. Once this is done the process is repeated for any remaining unmatched tracks in the P0D and then in the ECals. At the time of writing there is no overall global PID and instead the PID measurements from each subdetector associated with an object are retained to be investigated at the analysis level.

4.1.4   ND280 Analysis Software

The ND280 analysis uses a specially-constructed software framework based on the ROOT software framework [81] called "highland". The highland framework (high-level analysis at the near detector) allows the user to quickly run analyses, plot results and evaluate the impact of systematic errors. The output of highland is a ROOT file containing several data "trees", some of which are single-entry trees such as the POT while others contain a summary of the variables used in the analysis. The output file can be analysed easily with the DrawingTools package in highland.

At its core, highland contains several packages:

- highlandTools which contains the core classes used in the framework.

- highlandIO which deals with the input from analysis files and creates the output files.

- baseAnalysis which provides the basic structure for an analysis. User analyses inherit from this package.

The $\bar{\nu}_e$ CC selection inherits from the baseAnalysis package and utilises several selection criteria that were developed for the ν_e CC selection package.

Figure 4.1: A visual overview of the ND280 software suite showing the outputs of each process feeding into the next [52].

4.2 $\bar{\nu}_e$ Selection

In this section, a selection of the $\bar{\nu}_e$ candidates is defined. In order to avoid the possibility of unconscious biases in the data selection, the selection criteria are developed and honed using only MC. After the selection criteria have been

finalised, they are applied to T2K data. The $\bar{\nu}_e$ CC selection is closely related to the T2K ν_e CC selection and criteria 1-11 in Table 4.1 are shared between the ν_e and $\bar{\nu}_e$ CC-inclusive selections.

A neutrino "event" in ND280 analysis is defined as one or more reconstructed particle tracks with a single, well-defined starting point in the material of the detector. The $\bar{\nu}_e$ selection starts by imposing several criteria to ensure that the event is of adequate quality and that it has the reconstructed information in the ND280 subdetectors necessary for the selection. There are several particle identification (PID) criteria which select positron-like tracks while rejecting muon-like and pion-like tracks. While there is some use of the ECal PID, the primary PID variables applied are those from the TPC subdetector. As discussed in Section 3.2.2.2, the TPCs detect and measure the charge due to ionisation caused by charged particles passing through the TPC drift gas. The amount of ionisation depends on the rate at which a particle of a given momentum loses energy, which is defined by the Bethe-Bloch formula:

$$-\left\langle \frac{dE}{dx} \right\rangle = \frac{4\pi}{m_e c^2} \cdot \frac{nz^2}{\beta^2} \cdot \left(\frac{e^2}{4\pi\epsilon_0} \right)^2 \cdot \left[\ln\left(\frac{2m_e c^2 \beta^2}{I \cdot (1-\beta^2)} \right) - \beta^2 \right] \quad (4.1)$$

where z is the charge of the particle, ϵ_0 is the vacuum permittivity, n is the electron density of the material, I is the mean excitation potential of the material, m_e is the mass of an electron, e is the electric charge and β is $\frac{v}{c}$. Using Equation 4.1 and a measurement of a particle's momentum based on its curvature in the magnetic field of the ND280, the energy-loss rate for a given particle type can be predicted as seen in Figure 4.6, which shows the dE/dx curves measured by T2K. This is used to define the TPC PID pulls given by [63]:

$$\delta_i = \frac{C_T^m - C_T^e(i)}{\sigma(i)} \quad (4.2)$$

where C_T^m is the measured rate of energy loss of the particle (dE/dx), $C_T^e(i)$ is the expected rate of energy loss for a particle of type i, and $\sigma(i)$ is the ionisation energy resolution of the TPCs for particle type i. The pulls used can be seen in Figures 4.2 to 4.4. Finally, there are several veto criteria to reduce background from gamma rays converting into an e^+e^- pair in the detector. These cuts in order are detailed below and summarised in Table 4.1.

1. Event Quality: The event must be associated with a beam trigger and all reconstructed tracks in an event must be within 60 ns (4σ) from the centre of one of the eight beam bunches in a spill.

2. Track Charge: Ensure that the track (the highest-momentum track in the event) has the correct charge (positive when looking for $\bar{\nu}_e$ CC interactions).

3. Momentum: The momentum of the candidate track must be greater than 200 MeV/c in order to remove background from gamma conversions which dominate in the region below 200 MeV/c.

4. FGD FV: The interaction vertex associated with the candidate track must be within the FGD Fiducial Volume (FV).

5. TPC Quality: Require more than 35 reconstructed TPC hits associated with the positron candidate in order to ensure reliable TPC information.

6. PID: The TPC PID is used to identify positron candidates by requiring that the candidate fit the positron hypothesis and does not match either the pion or muon hypotheses; specifically, we apply the following criteria on δ_i from Equation 4.2:

   - $-1 < \delta_e < 2$

   - $\delta_\mu < -2.5$ or $\delta_\mu > 2.5$

- $\delta_\pi < -2$ or $\delta_\pi > 2$

Which can be seen in Figures 4.2, 4.3 and 4.4.

ECal PID (described in Section 4.3.2) is also used where available requiring one of two criteria:

- An ECal likelihood to prefer an electromagnetic hypothesis over the MIP-like hypothesis if the track momentum as measured by the TPC is greater than 1000 MeV/c or the particle shower is not fully contained in the ECal.

- The energy deposited by a particle as it traverses the ECal to be greater than 1100 MeV if the track momentum is less than 1000 MeV/c and the particle shower is fully contained in the ECal.

7. TPC2 PID: This is used to place criteria on a second reconstructed TPC segment (a reconstructed segment in a second TPC if the particle has traversed two TPCs) if one is present. This criterion is less stringent than the previous PID criteria and in order to remove muons requires $\delta_\mu < -2.5$ or $\delta_\mu > 2.5$.

8. TPC Veto: Any events which have a TPC track upstream of the start position of the lepton candidate are removed. This reduces background from upstream interactions which send a positron like track through the FGD.

9. Pair Veto: Events with a pair of tracks that have opposite charge and originate at the event vertex are removed if the invariant mass of the pair is less than 100 MeV/c. This eliminates the majority of events where the positron candidate originated from a gamma conversion rather than from an electron anti-neutrino interaction.

10. P0D Veto: Events where there is a reconstructed object in the P0D are vetoed. Gammas exiting the P0D which convert in the FGD fiducial volume are a strong contributor to the gamma background. When the reconstructed vertex of the positron candidate is in FGD2, it is also required that there are no reconstructed objects in FGD1. This further reduces the background from gamma conversions by eliminating any events from the P0D which could produce gamma rays.

11. ECal Veto: Events with a reconstructed ECal object which is upstream of the positron candidate and is not associated with the positron candidate are removed. As neutrino interactions in the ND280 are forward boosted it is unlikely that a neutrino interaction will produce ECal activity upstream of the neutrino interaction; therefore, this veto had a minimal effect on the desired ν_e CC events while reducing any backgrounds that originate from a neutrino interaction in the ECals such as gamma ray conversions.
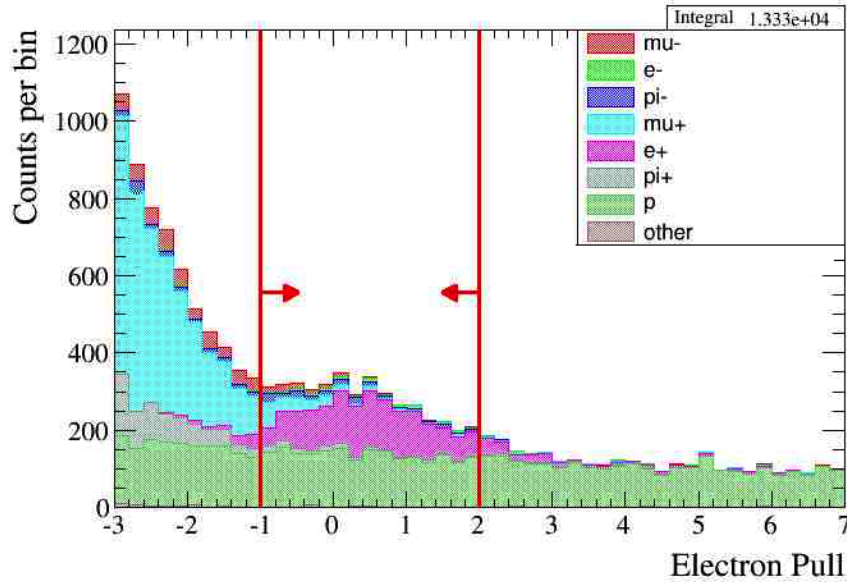
Figure 4.2: The δ_e criterion from criteria 6 from Table 4.1. The arrows indicate selected events. The coloured histogram is MC, with the various colours denoting the particle type of the highest momentum track in the event.
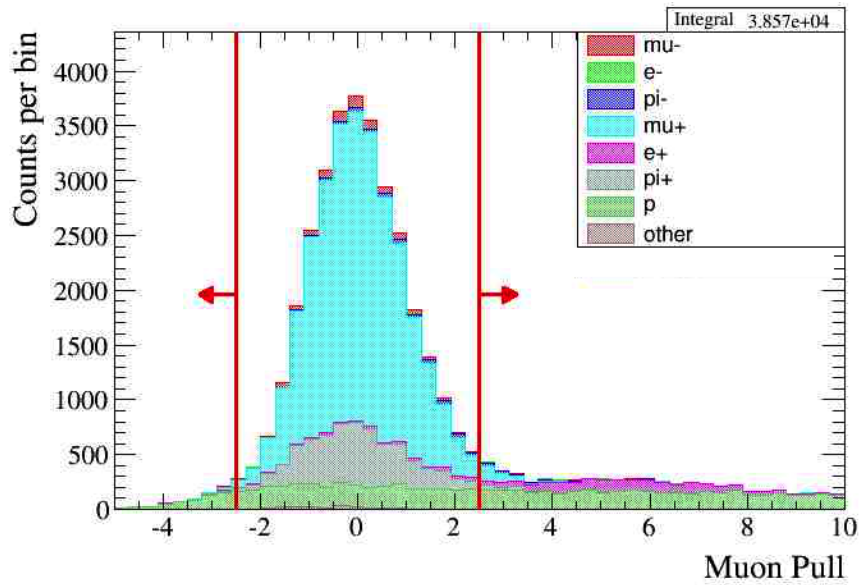
Figure 4.3: The δ_μ criterion from criteria 6 from Table 4.1. The arrows indicate selected events. The coloured histogram is MC, with the various colours denoting the particle type of the highest momentum track in the event.
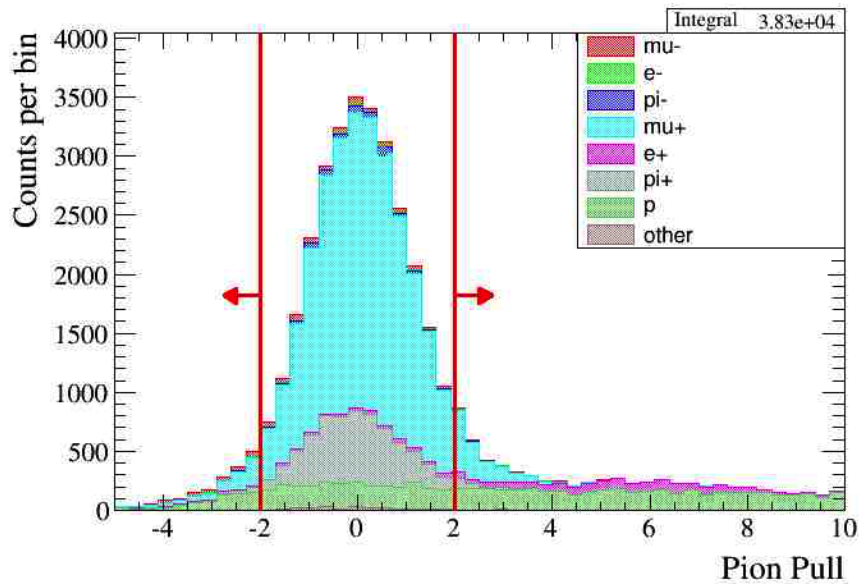
Figure 4.4: The δ_π criterion from criteria 6 from Table 4.1. The arrows indicate selected events. The coloured histogram is MC, with the various colours denoting the particle type of the highest momentum track in the event.

Following the application of criteria 1 through 7 in Table 4.1, the sample is 49% pure in positrons but only 14% of these positrons originate from a $\bar{\nu}_e$ interaction,

with the majority of the non-$\bar{\nu}_e$ events originating from gamma rays. A significant

portion of these gamma rays have been produced in a neutrino interaction which

occurred elsewhere in the detector, usually upstream, which has traveled through

the TPCs without interaction before converting to an e^+e^- pair in the FGD fiducial

volume. To reduce the contamination from gamma ray events an upstream veto is

applied which rejects events with reconstructed tracks in the P0D, TPC, or ECals

that start more than 10 cm upstream of the initial position of the reconstructed

positron candidate (criteria 8, 10, 11 in Table 4.1). If an electron-like negative

track is reconstructed within 10 cm of the positron candidate and the pair of

tracks have a reconstructed mass less than 100 MeV/c^2 (cut 9 in Table 4.1), the

event is rejected as shown in Figures 4.5(a) and 4.5(b). These requirements reduce

the gamma contamination to 16% from 38%. A summary of the criteria as used

in both the ν_e selection and $\bar{\nu}_e$ selection to this stage can be seen in Table 4.1 as

criteria 1-11 and in reference [73] which describes the T2K ν_e CC selection. The

effect each of these criteria has on the sample, in terms of total events and the

number of $\bar{\nu}_e$ CC events selected, can be seen in Table 4.2.

Following the application of all criteria that are also used in the ν_e selection

(cuts 1-11 from Table 4.1) the selection efficiency is 45%; however, the purity is

low due to the presence of protons which, in the ν_e selection, were removed by the

negative charge requirement, but which are accepted in the $\bar{\nu}_e$ selection which has

a positive charge requirement. The proton background will be discussed in the

next section.

4.3   Misidentified Protons in the $\bar{\nu}_e$ Selection

Following the application of all criteria that are also used in the ν_e CC selection,

the $\bar{\nu}_e$ CC selection shares the same backgrounds as the ν_e CC selection which

Criterion Number	Criterion Name	Requirements
1	Event Quality	-
2	Track charge	A positive track ($\bar{\nu}_e$ selection) A negative track (ν_e selection)
3	Momentum	Momentum > 200 MeV/c
4	FGD FV	Track starts inside FGD fiducial volume
5	TPC Quality	Number of TPC hits > 35
6	PID	Apply TPC PID as detailed Section 4.2
7	TPC2 PID	If 2nd TPC segment is present require it is not muon-like
8	TPC Veto	Veto events with upstream TPC activity
9	Pair Veto	Veto events which have tracks consistent with a e$^+$e$^-$ pair
10	P0D Veto	Veto events with P0D activity
11	ECal Veto	Veto events with upstream ECal activity
12	Proton Rejection Criteria	If in momentum 600 MeV/c to 2000 MeV/c require: If in the DsECal: E/P > 0.7 -30 $<$ LLR_ECal_EMHIP $<$ -3 22 $<$ LLR_ECal_MIPPION $<$ 50 If in the BrECal: E/P > 0.7 -20 $<$ LLR_ECal_EMHIP $<$ 1 22 $<$ LLR_ECal_MIPPION $<$ 38

Table 4.1: The parameters of the $\bar{\nu}_e$ and ν_e CC-inclusive selections. The proton rejection criteria (criterion 12) are unique to the $\bar{\nu}_e$ selection and are discussed in Section 4.3.2. The number of events remaining after each of these criteria are applied can be seen in Table 4.2.
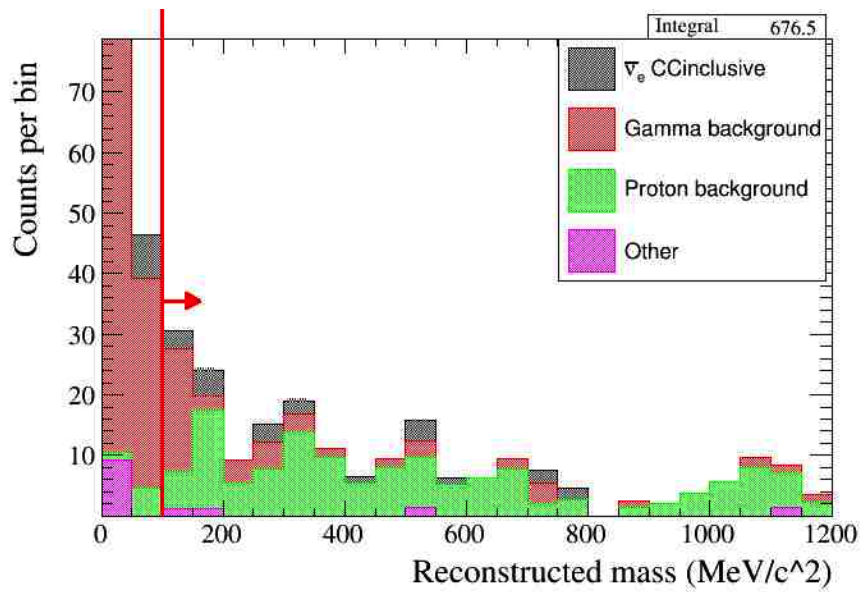
(a)
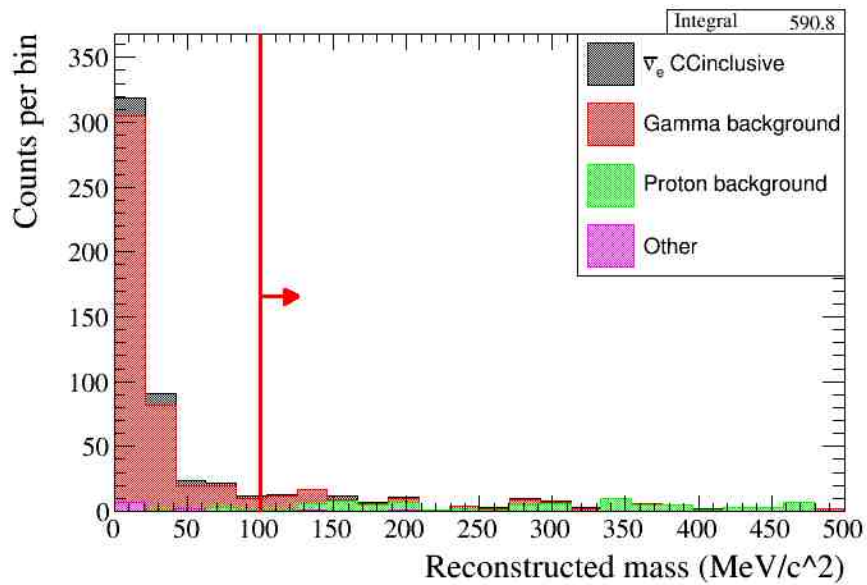
(b)

Figure 4.5: The reconstructed invariant mass for pairs of tracks in the sample with the arrow showing events which pass the pair veto. Figure 4.5(b) is a zoomed in version of 4.5(a). The plots show MC simulated data.

are discussed in Section 4.5. However, in addition there is one unique feature to the $\bar{\nu}_e$ CC selection, which is a large background of protons. These protons originate mostly from ν_μ CC and $\bar{\nu}_\mu$ CC interactions which produce a proton in

Criterion number	Total Events Selected	$\bar{\nu}_e$ CC Selected
4	56810	679
5	51087	609
6	2463	343
7	2374	333
8	1838	311
9	1525	272
10	1519	272
11	1248	260
12	439	184

Table 4.2: The total number of events and the number of $\bar{\nu}_e$ CC events selected in the MC sample after each of the criteria in Table 4.1.

the final state. The reason for these protons passing the selection criteria will be discussed in Section 4.3.1 and their removal will be discussed in Section 4.3.2. The remaining sample after the removal of the protons is discussed in Section 4.6 and the remaining backgrounds, including any remaining protons, are covered in Section 4.5.

4.3.1 Proton Misidentification Due to TPC PID Limitations

As discussed in Section 4.2 the TPCs detect and measure the charge due to ionisation caused by charged particles passing through the drift gas, which is then used to create a PID pull variable for several particle hypotheses as shown in Equation 4.2. As can be seen in Figure 4.6, the positron and proton dE/dx is similar for particles with momenta near 1000 MeV/c. The TPC pulls are entirely dependent on the dE/dx for particle identification; hence, protons with momentum near 1000 MeV/c cannot be distinguished from positrons by TPC PID. Changing the charge requirement on the ν_e selection is necessary but not sufficient to create a suitable $\bar{\nu}_e$ selection, and by itself results in a sample with 57% protons as can be seen in Figure 4.7, where a sharp background peak of protons can be seen to

dominate over the $\bar{\nu}_e$ signal around the 1000 MeV/c region. In addition, this new background is prominent in a region of momentum where the other main background in the sample, the gamma background, begins to decrease and so it affects an area of phase space that is relatively high purity in the ν_e selection. Section 4.3.2 describes the additional criteria imposed to remove the proton contamination.
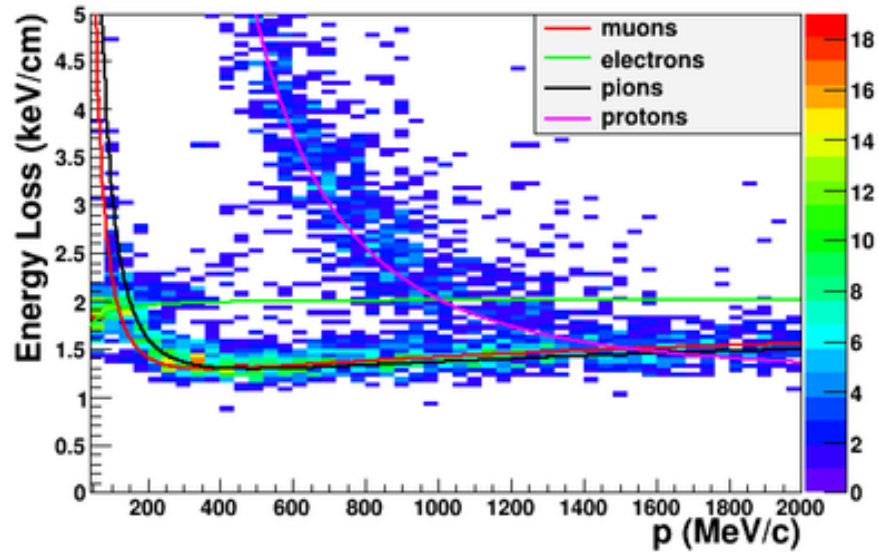
Figure 4.6: The dE/dx curves for the T2K ND280 TPCs. Blue points are data and the curves are theoretical predictions. The pink line for protons can be seen to cross the green line for positrons (electrons) at 1000 MeV/c [73].
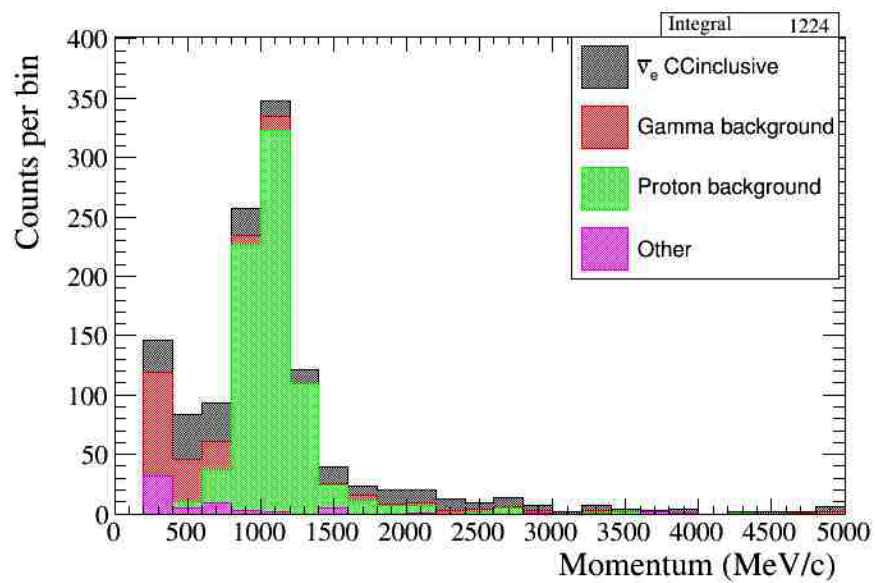
Figure 4.7: The $\bar{\nu}_e$ sample before applying the proton criteria plotted as a function of the positron candidate's momentum. The green shows the proton background dominating over signal (grey) near momentum of 1000 MeV/c. The coloured histogram is MC simulation.

4.3.2 Proton Removal: E/p and ECal PID Variables

In order to remove the protons from the $\bar{\nu}_e$ sample, we must use one of the other subdetectors in the ND280 because the TPCs are unable to discriminate protons from positrons near momenta of 1000 MeV/c. Several combinations of the ECal PID variables were employed; however, they did not yield satisfactory results on their own. Therefore, variables which combined information from different subdetectors were investigated. After applying the TPC criteria, any protons left in the analysis will have a momentum of approximately 1000 MeV/c. Any positrons with a similar momentum will have significantly more kinetic energy than protons due to the larger mass of the proton; hence, the ratio of the momentum measured by the TPCs and the total reconstructed energy deposited in the ECals (E/p) is a strong discriminator between protons and positrons as can be seen in Figures 4.8(a) and 4.8(b). The value of 0.7 for E/p in both the DsECal and BrECals yields the best discrimination between positrons and protons as shown by n-1 plots (plots where all selection criteria are applied except criteria on the variable being plotted) in Section 4.3.3 and Table 4.1.

As some protons are still remaining in the selection following application of the E/p requirement, ECal PID variables [82] are also used in order to maximise the purity of the selection. A description of these variables is below:

- LLR_EM_HIP - A log-likelihood ratio variable, which was designed to separate proton-like, highly-ionising (HIP), interactions from electron-like or positron-like, electromagnetic (EM), interactions. Proton-like events tend to have higher values of LLR_EM_HIP than positron-like interactions as shown in Figure 4.9(a) for the DsECal and Figure 4.9(b) for the BrECal.

- LLR_MIP_PION - A log-likelihood ratio variable, which was designed for discriminating between showering pions and minimally-ionising (MIP) par-

ticles. Positron-like interactions tend to have higher values than proton-like interactions as shown in Figure 4.10(a) for the DsECal and Figure 4.10(b) for the BrECal.

The log-likelihood variables all use the following inputs to create a single likelihood variable for discriminating between two specific criteria:

- Circularity: A combination of two-dimensional principle component analyses such that:

$$\text{Circularity}_i = (2 \times (2nd \text{ principal component})) - 1 \qquad (4.3)$$

$$\text{Circularity} = \text{Circularity}_x \times \text{Circularity}_y \qquad (4.4)$$

- TruncatedMaxRatio: The charge ratio between the ECal layer with the most deposited charge and the least deposited charge, once the bottom and top 20% of hits in each layer have been discarded.

- QRMS: The root mean square of the charge distribution.

- FrontBackRatio: The ratio of charge deposited at the front of an ECal cluster to the charge deposited at the back of the ECal cluster.

Positrons and protons have very different interaction patterns in the ECals. A proton tends to produce a single short track that deposits the majority of its energy at the end of the track when the proton stops. A positron interaction has a high probability to induce an electromagnetic shower and therefore interact with many bars around the initial positron interaction. This produces a wide cone branching out from the point of initial interaction which is different from the typical proton signature and thus can be used to distinguish between the two.

Applying the proton criteria causes a large loss in efficiency. This is largely due to the requirement that all events have reconstructed ECal information, which was optional in previous criteria and is not present in all events. In order to minimize this loss the proton cut is only applied in the region where the proton background is dominant, from 600 MeV/c to 2000 MeV/c. The reason for this exact momentum range is explained in Section 4.3.3.

This causes the purity overall to fall by 7.3%, compared to a selection where the proton cut is applied across the entire momentum range; however, the gain in efficiency by only applying the proton cut to this region of momentum space is 10.0% which outweighs the loss in purity as can be seen in Figure 4.11(b).

The requirements placed on E/p and the ECal PID variables are shown in Table 4.1 criterion 12. The proton criteria reduce the proton background by 96%. The full selection results in a sample with a purity of $(41.9 \pm 2.4)\%$ and an efficiency of $(27.1 \pm 1.7)\%$ for $\bar{\nu}_e$ CC interactions in the FGD fiducial volume as shown in Figure 4.11(b) which shows the efficiency and purity versus the candidate positron's momentum. The backgrounds remaining in the selection are predominantly gamma background, as is also seen in the ν_e CC selection [73], though protons still make up approximately 6% of the total selected events. These backgrounds are discussed further in Section 4.5.1.
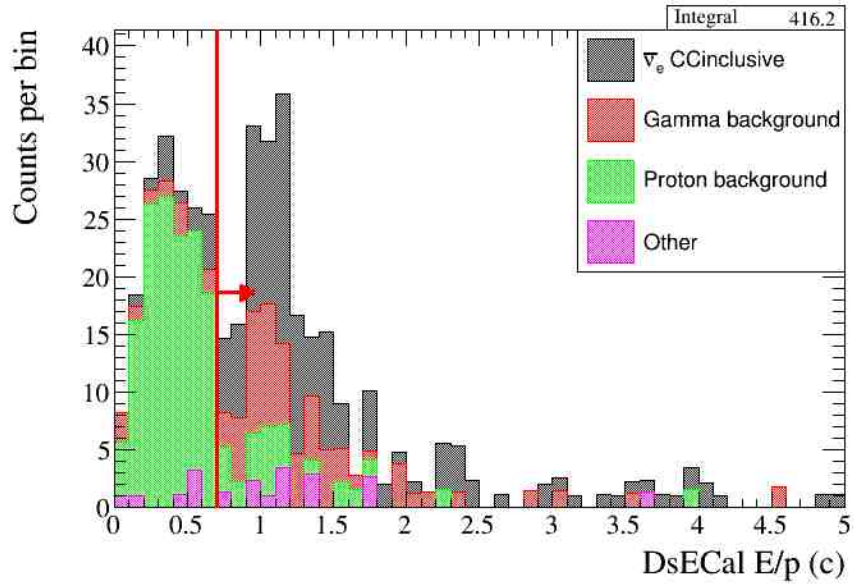
(a)
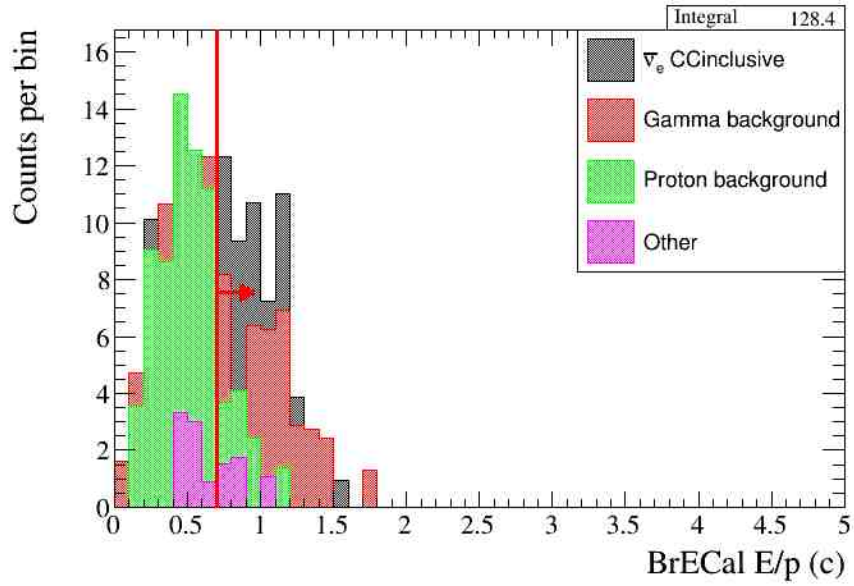
(b)

Figure 4.8: E/p for the DsECal (a) and the BrECal (b) after applying criteria 1-11 from Table 4.1. This variable combines information from the ECals and TPCs. It is the most discriminating variable in the selection and removes several events that cannot be removed using the ECal-only PID variables. The arrows indicate selected events. The coloured histogram is MC, grey is the $\bar{\nu}_e$ CC signal, green is the proton background, red is the gamma background and other backgrounds are shown in purple.
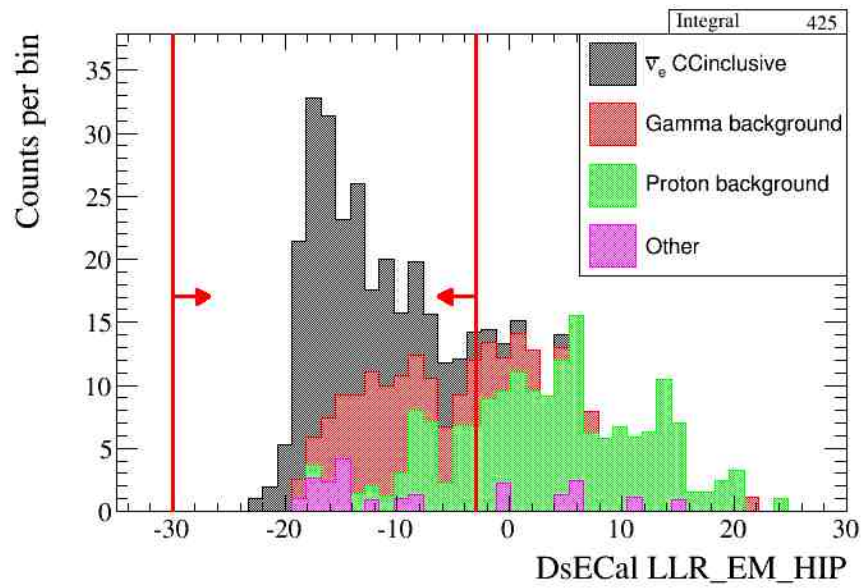
(a)
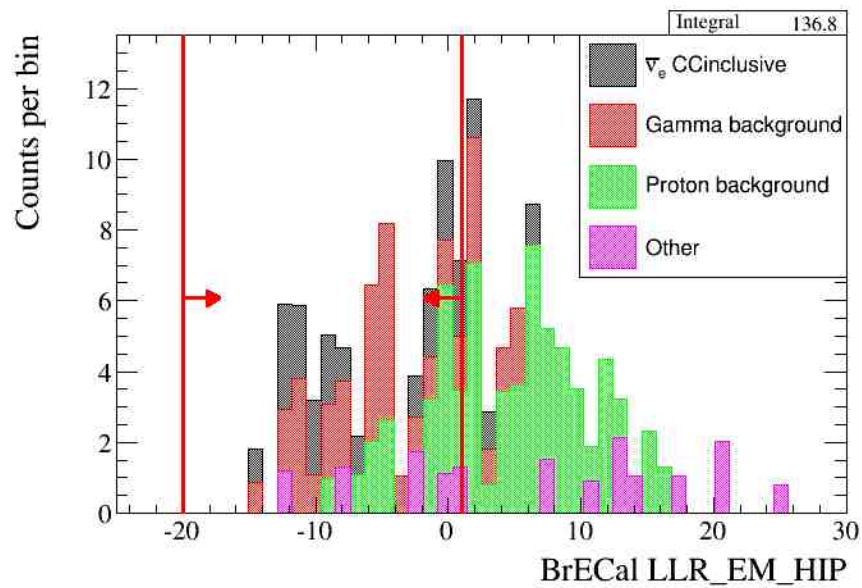
(b)

Figure 4.9: LLR_EM_HIP for the DsECal (a) and BrECal (b) after applying criteria 1-11 from Table 4.1. The arrows indicate selected events. The coloured histogram is MC, grey is the $\bar{\nu}_e$ CC signal, green is the proton background, red is the gamma background and other backgrounds are shown in purple.
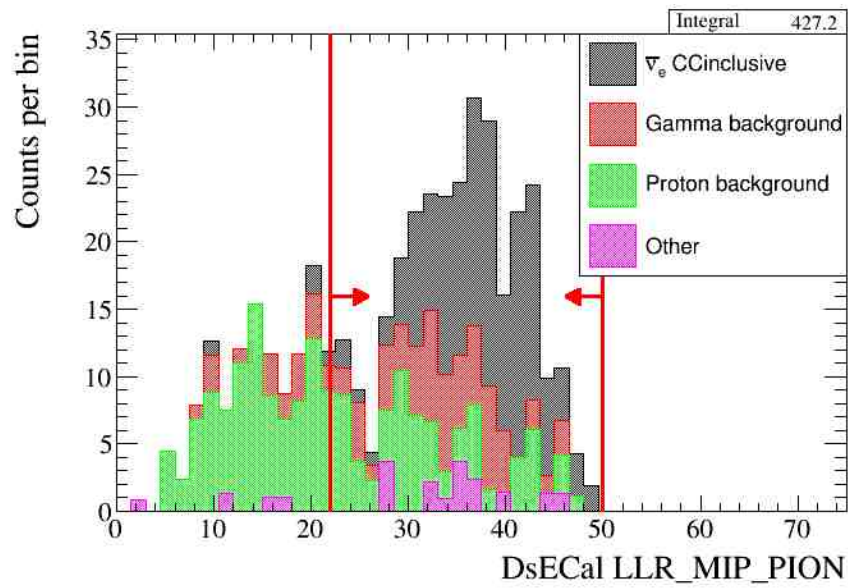
(a)
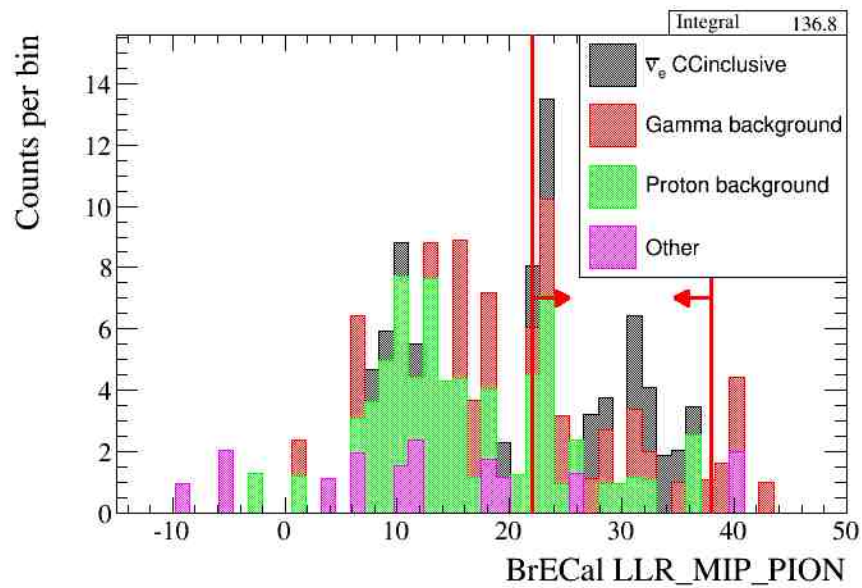
(b)

Figure 4.10: LLR_MIP_PION for the DsECal (a) and BrECal (b) after applying criteria 1-11 from Table 4.1. The arrows indicate selected events. The coloured histogram is MC, grey is the $\bar{\nu}_e$ CC signal, green is the proton background, red is the gamma background and other backgrounds are shown in purple.
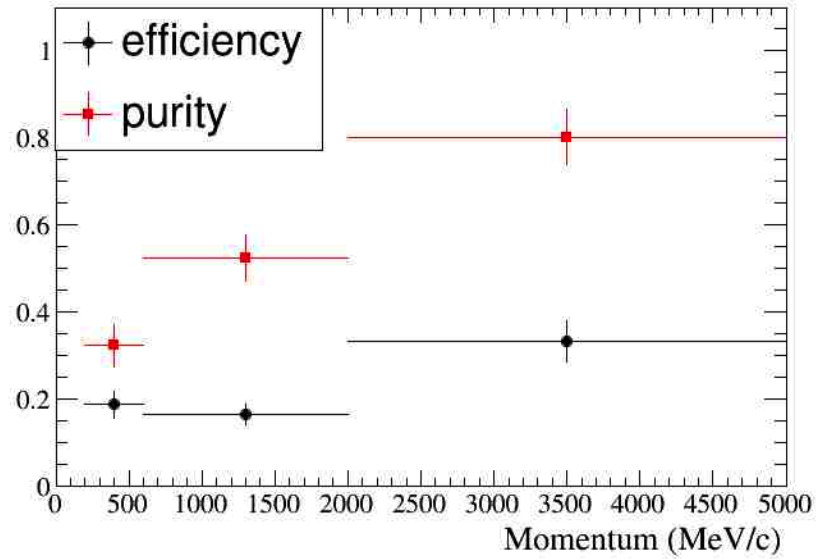
(a)
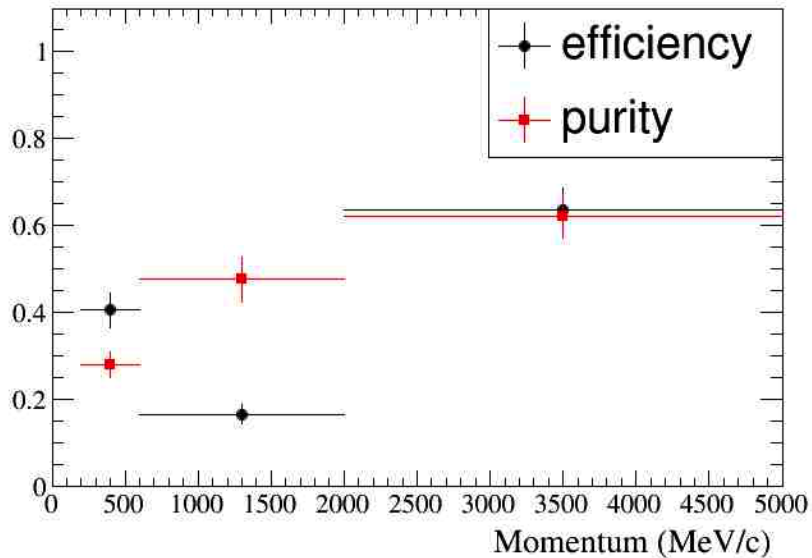
(b)

Figure 4.11: The efficiency and purity of the sample when the proton criteria (Criterion 12 in Table 4.1) are applied to all momentum space (a) and when it is only applied from 600 MeV/c to 2000 MeV/c (b), versus the momentum of the candidate positron. It can be seen that a considerable amount of efficiency is regained for a negligible loss in purity in the low and high momentum bins by not applying the proton criteria in these regions. The loss of efficiency in the 600 MeV/c to 2000 MeV/c region is due to the removal of any events which do not contain an ECal segment as without ECal information the proton background and $\bar{\nu}_e$ CC signal cannot be separated.

4.3.3 Selection Tuning

The selection criteria described in Section 4.3.2 were tuned by first setting criteria values by eye to remove backgrounds while preserving signal. These criteria were then optimised with n-1 plots to have the greatest purity $\times$ efficiency in the selection, resulting in minor shifts in the criteria. This section shows the n-1 plots.

It can be seen in Figures 4.12(a) and 4.12(b) that the E/p requirement in the proton criteria removes more of the proton background than the other criteria. This is due to the momentum limitation on the proton background due to the TPC PID discussed in Section 4.2, which means that the E/p variable is more powerful than even the LLR_EM_HIP variable, which was designed to discriminate between protons and positrons. The LLR_EM_HIP requirement does remove protons that are not removed by the E/p requirement (as seen in Figures 4.13(a) and 4.13(b)) as should be expected from a variable designed to separate proton interactions from electromagnetic interactions. The LLR_MIP_PION requirement (as seen in Figures 4.14(a) and 4.14(b)) is the weakest of the criteria applied as is to be expected for a variable which is not being used for its designed purpose.

As noted in Section 4.3.2 the proton criteria are only applied in a limited momentum range so as to maximise the efficiency of the selection. Figures 4.15(a) and 4.15(b), which show the momentum distribution of positron candidates with DsECal and BrECal components respectively, suggest that this range should be 600 MeV/c to 1400 MeV/c. However, Figure 4.16 shows that the proton distribution for events which do not enter the ECal tails out to 2000 MeV/c and so the optimal region over which the proton cut is applied is 600 MeV/c to 2000 MeV/c. The reason for this tail in the events without ECal information is that the PID criteria (Number 6 in Table 4.1) use ECal information if it is available and so some protons are removed by these extra criteria that are not removed from events

without ECal information. Because no method of removing the proton background without utilising the ECals was found, all events which do not enter the ECal have to be rejected.
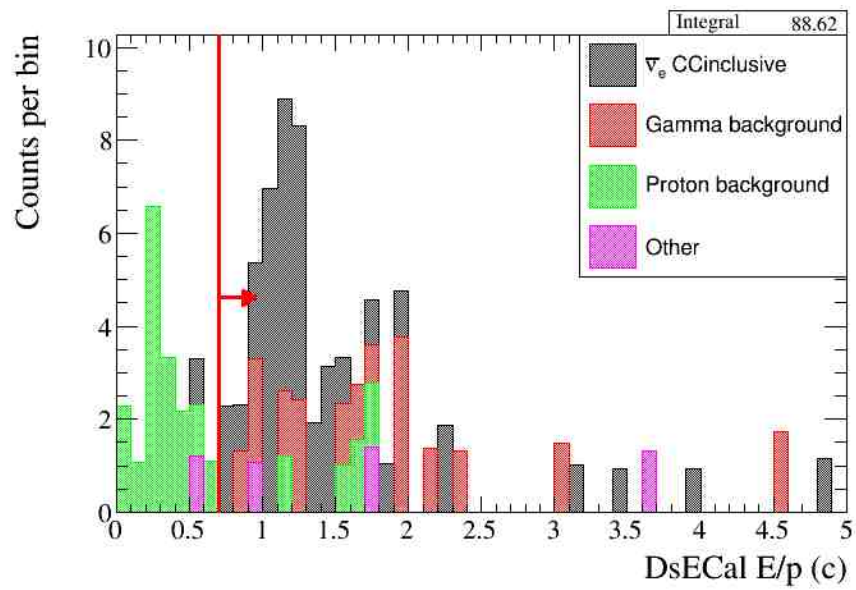
(a)
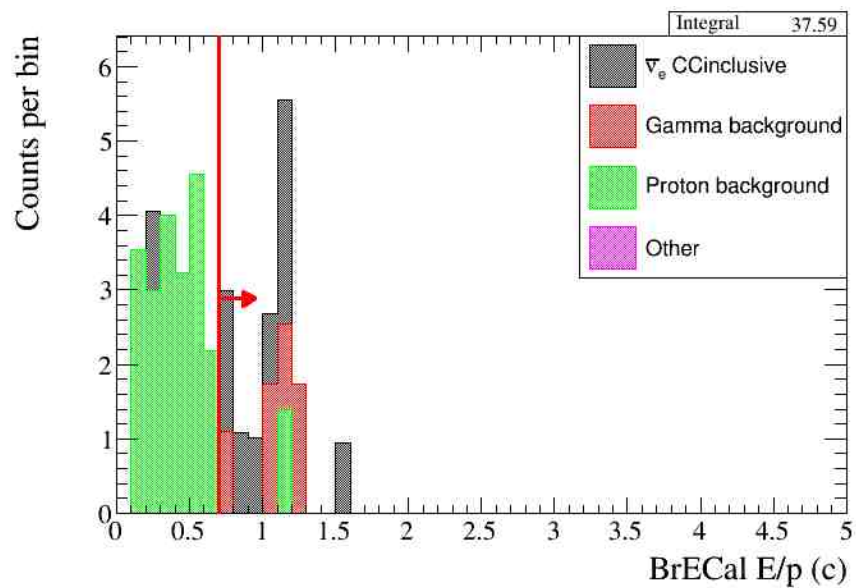
(b)

Figure 4.12: E/p for the DsECAL (a) and the BrECal (b) after all criteria are applied except the requirement on these variables in criterion 12 from Table 4.1. The arrows indicate selected events. The coloured histogram is MC, grey is the $\bar{\nu}_e$ CC signal, green is the proton background, red is the gamma background and other backgrounds are shown in purple.
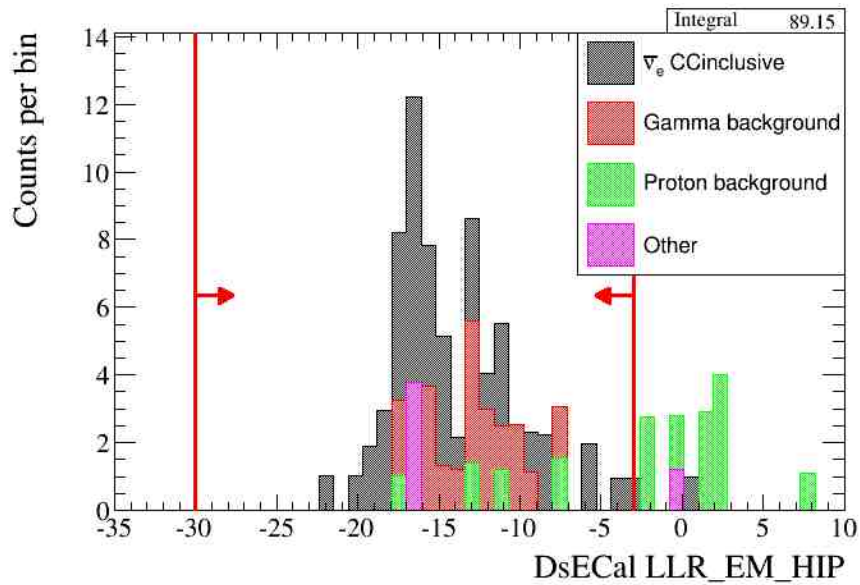
(a)
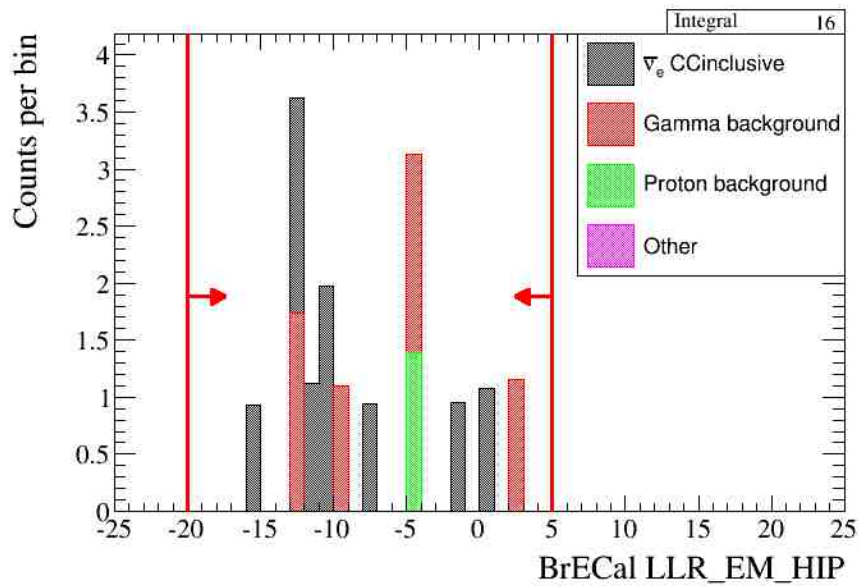
(b)

Figure 4.13: The log-likelihood variable LLR_EM_HIP for the DsECal (a) and BrECal (b) after all criteria are applied except the requirement on these variables in criterion 12 from Table 4.1. The arrows indicate selected events. The coloured histogram is MC, grey is the $\bar{\nu}_e$ CC signal, green is the proton background, red is the gamma background and other backgrounds are shown in purple.
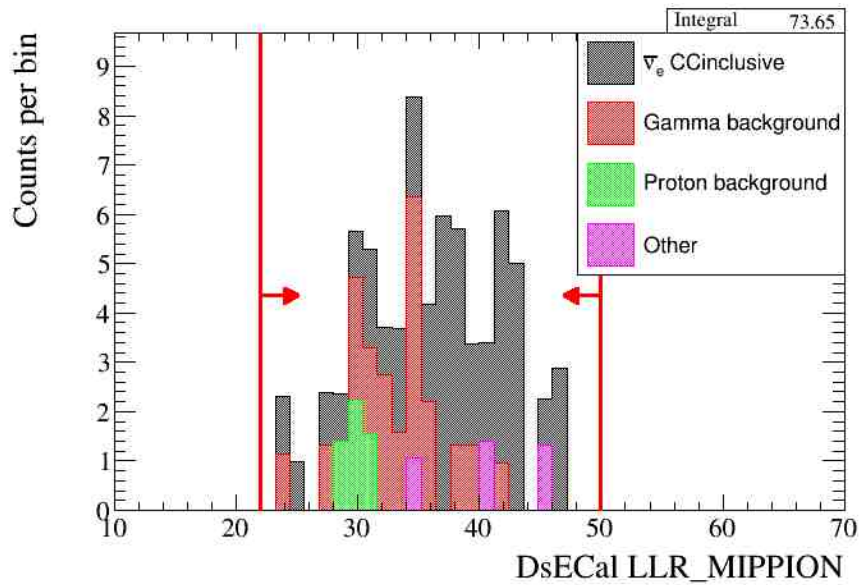
(a)
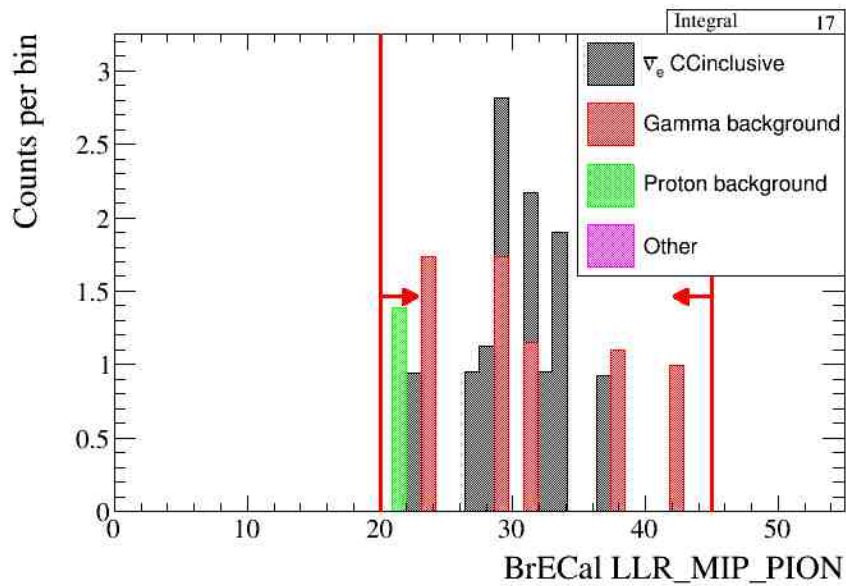
(b)

Figure 4.14: The log-likelihood variable LLR_MIP_PION for the DsECal (a) and BrECal (b) after all criteria are applied except the requirement on these variables in criterion 12 from Table 4.1. The arrows indicate selected events. The coloured histogram is MC, grey is the $\bar{\nu}_e$ CC signal, green is the proton background, red is the gamma background and other backgrounds are shown in purple.
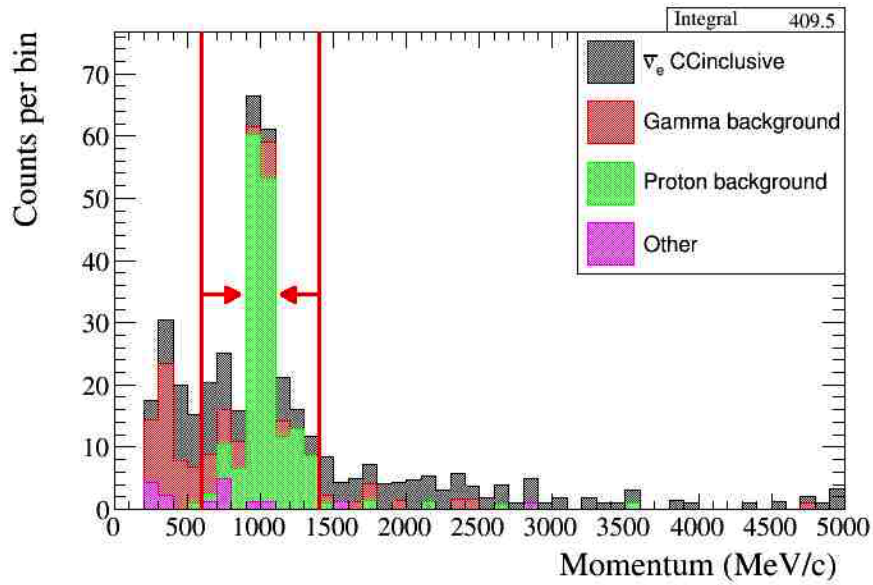
(a)
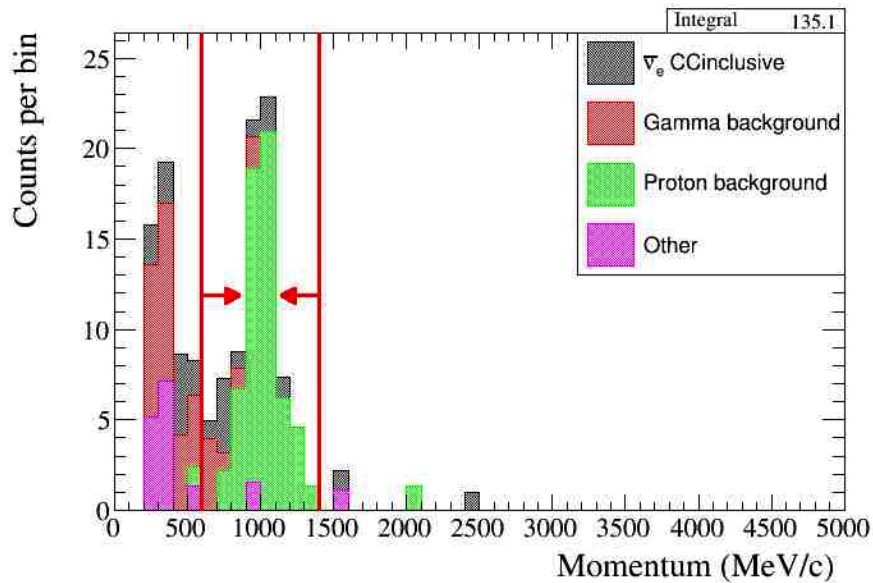
(b)

Figure 4.15: The momentum of the positron candidate for events which have a DsECal component (a) and those which have a BrECal component (b) after criteria 1-11 are applied from Table 4.1. The plots show that for both DsECal and BrECal events, the proton criterion only needs to be applied from 600 MeV/c to 1400 MeV/c in order to preserve efficiency as seen in Figure 4.11(a) and Figure 4.11(b). The arrows show this region. The coloured histogram is MC, grey is the $\bar{\nu}_e$ CC signal, green is the proton background, red is the gamma background and other backgrounds are shown in purple.
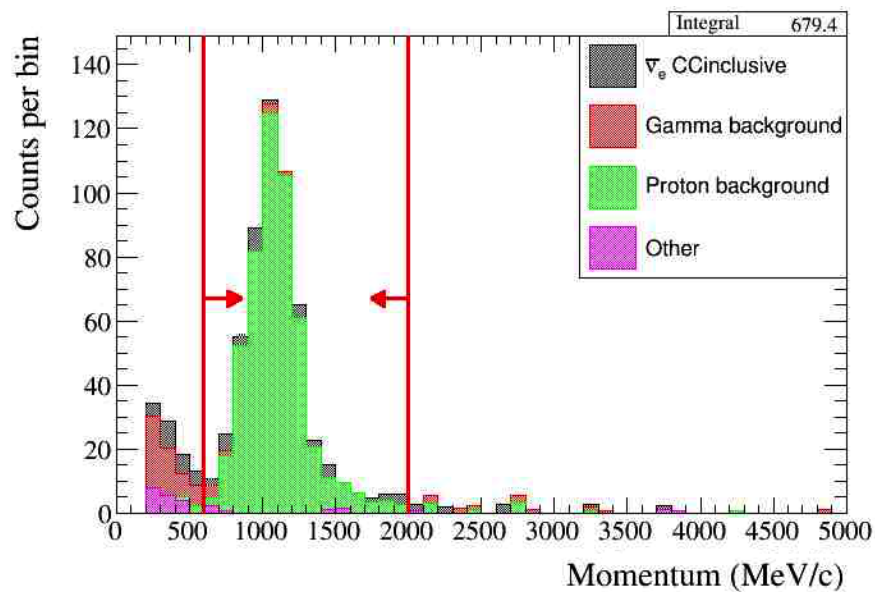
Figure 4.16: The momentum of the positron candidate for events without any reconstructed components in either the DsECal or BrECal after criteria 1-11 are applied from Table 4.1. This plot shows a tail on the proton events which extends out to 2000 MeV/c, which means that the proton criterion needs to be applied from 600 MeV/c to 2000 MeV/c rather than 600 MeV/c to 1400 MeV/c as suggested by Figures 4.15(a) and 4.15(b). The coloured histogram is MC, grey is the $\bar{\nu}_e$ CC signal, green is the proton background, red is the gamma background and other backgrounds are shown in purple

4.4 Performance of the Selection

The final selected sample has a $\bar{\nu}_e$ purity of $(41.9 \pm 2.4)\%$ and an efficiency of $(27.1 \pm 1.7)\%$, where the uncertainty is due to the MC statistical uncertainty and was calculated by the method discussed in Appendix B. The total number of events selected in MC and data and the POT of each used is shown in Table 4.3. The purity and efficiency of the selection are shown versus the momentum of the selected positron candidate (Figure 4.11(b) and Figure 4.17) and versus the cosine of the angle of the positron candidate's track with respect to the ND280 z-axis, $\cos(\theta)$ (Figure 4.18). It can be seen in Figure 4.17 that there is a large efficiency loss for selecting positrons with momentum between 600 MeV/c and 2000 MeV/c which is unavoidable due to the special criteria in order to reduce the proton background in that region.

Table 4.4 shows the purity and efficiency for events which use TPC and DsE-Cal PID; TPC and BrECal PID; and only use TPC PID as they do not have a reconstructed ECal segment. The table is divided into events where the interaction vertex is in FGD1 and where it is in FGD2. From Table 4.4 it can be seen that the FGD2 sample is mainly comprised of events with a DsECal segment with only 8.8% of events containing either a BrECal segment or no ECal segment. As both FGDs have similar masses and the mass-weighted CC inclusive cross-section ratio of oxygen to carbon is close to unity [83], both FGDs have a similar neutrino interaction rate and thus before the selection criteria are applied both have a similar number of neutrino interaction vertices. The DsECal PID has greater discrimination power than the BrECal PID, due to particles entering the DsECal at angles approximately perpendicular to the upstream face; whereas, particles entering the BrECal do so at shallow angles which makes reconstruction more challenging. Therefore the proximity of the DsECal to FGD2 causes an FGD2-

only sample, as seen in Figure 4.19(b), to have more events and a greater purity than an FGD1-only sample as seen in Figure 4.19(a). The FGD1 sample is 37.9% pure whereas the FGD2 sample is 42.4% pure.

Figure 4.20 shows the changes in efficiency and purity as each of the $\bar{\nu}_e$ selection criteria in Table 4.1 are applied. The largest changes in efficiency and purity are due to the application of the first PID selection criteria and the proton criteria, while the veto criteria have small though noticeable improvements in purity. This is to be expected given the power of the TPC and ECal PID variables.
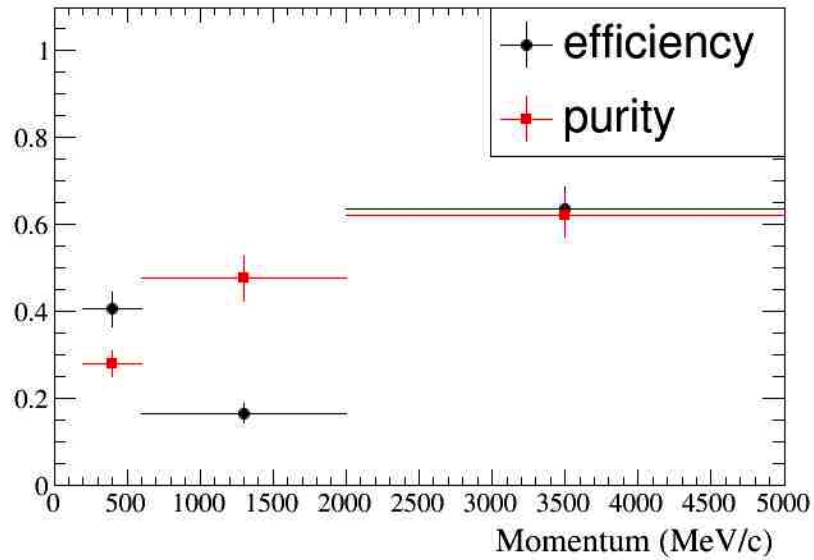
Figure 4.17: The efficiency and purity of the $\bar{\nu}_e$ CC selection versus the positron candidate's momentum. It can be seen that the central bin where the proton criterion is applied has taken a large efficiency loss.

	Total POT	Total Number of Events	Normalised Number of Events
Data	9.549×10^{19}	45	45
MC	1.0×10^{21}	439	41.92

Table 4.3: The total number of events selected in data and MC for the final number of MC events after normalising to POT of the data.
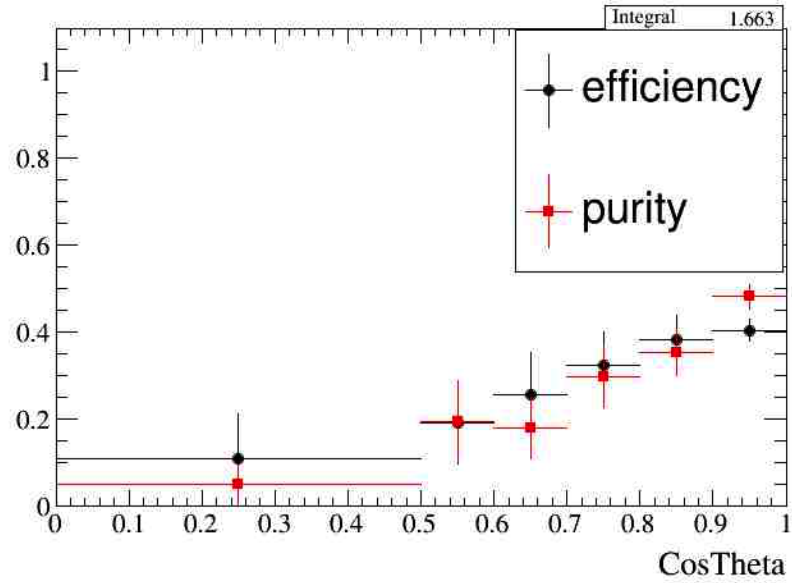
Figure 4.18: The efficiency of the $\bar{\nu}_e$ CC selection versus $\cos(\theta)$ where θ is the angle between the direction of the positron candidate and the z-axis of the detector.

FGD1			
Category	Events (%)	Efficiency (%)	Purity (%)
TPC only	41.7	18.0	32.3
TPC + DsECal	33.7	43.9	43.8
TPC + BrECal	24.6	38.4	42.2
FGD2			
	Events (%)	Efficiency (%)	Purity (%)
TPC only	5.1	8.4	17.5
TPC + DsECal	91.2	47.8	50.0
TPC + BrECal	3.7	30.7	18.2

Table 4.4: The purity and efficiency for events which use TPC and DsECal PID, TPC and BrECal PID and only use TPC PID as they do not have a reconstructed ECal segment. With the breakdown between events where the positron candidate originates in FGD1 or FGD2, it can be seen that the proximity of the DsECal to FGD2 has a large impact on the efficiency of the sample. The FGD1 sample also contains significantly more TPC-only events than the FGD2 sample, due to the particles leaving FGD1 showering in FGD2 before they reach an ECal.
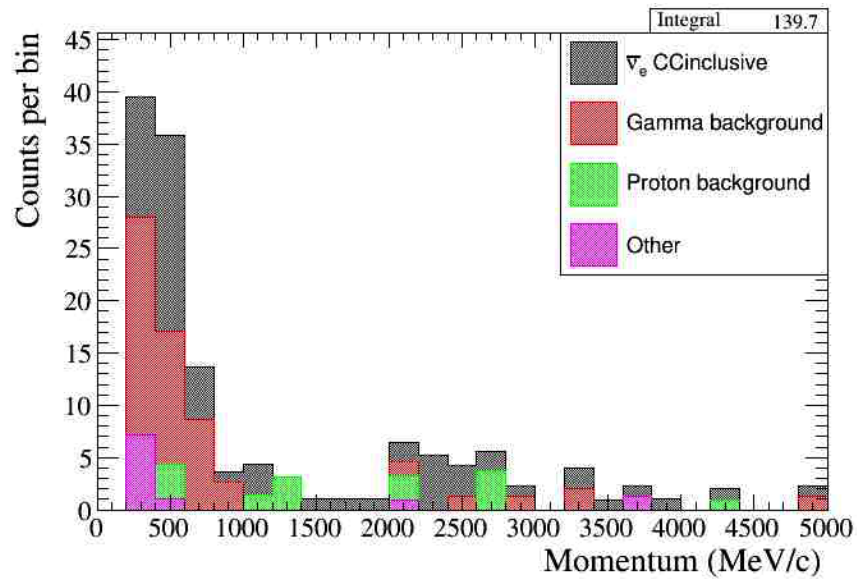
(a)
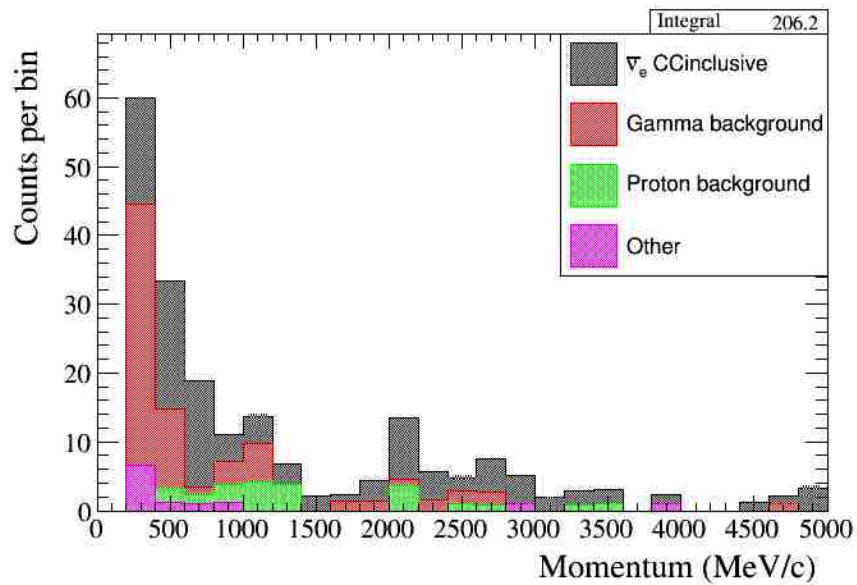
(b)

Figure 4.19: The selected samples for FGD1 (a) and FGD2 (b) plotted as a function of the positron candidate's momentum. The greater number of events in the FGD2 sample is due to the greater discriminating power of the DsECal which is closer to FGD2 than to FGD1.
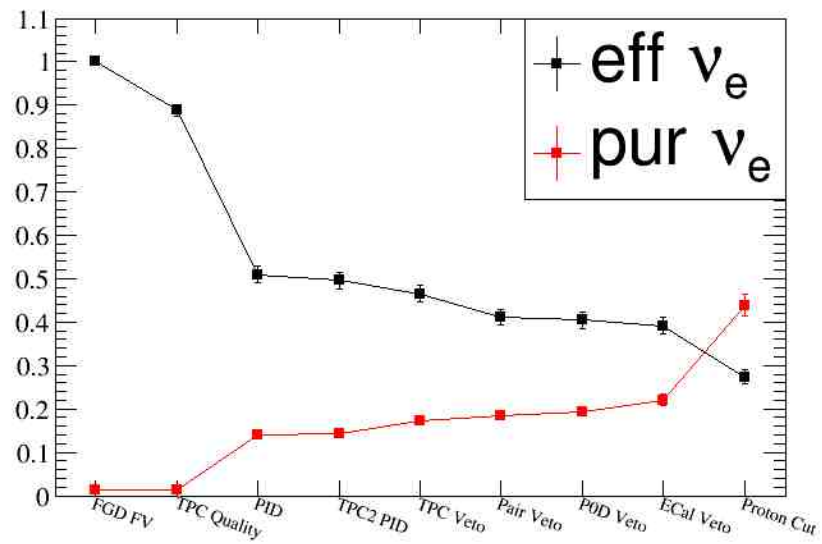
Figure 4.20: The efficiency and purity of selecting $\bar{\nu}_e$ CC events as each criterion in Table 4.1 is applied. The efficiency is relative to the number of events which have the highest-momentum positive track starting in the FGD fiducial volume.

4.5   Backgrounds

In this section, the backgrounds remaining in the selection will be presented. The proton background, which is unique to the $\bar{\nu}_e$ selection, is detailed in Section 4.5.1. The gamma background, which is the dominant background in this selection and has also been the dominant background in the ν_e selection, is detailed in Section 4.5.2. Any other backgrounds in the selection are covered in Section 4.5.3.

4.5.1   Remaining Proton Background

Following the application of the proton rejection criteria, the $\bar{\nu}_e$ sample is still 6.3% protons. The proton momentum distribution is shown in Figure 4.21. These protons can be broken down into two categories: protons with high momentum where, for the sake of efficiency, it is not worth applying the proton criteria (see Figures 4.11(a) and 4.11(b)), and those protons that manage to pass all the criteria, including the proton rejection criteria. For the protons which pass the criteria it is important to understand why they do. To this end, event displays of MC simulated events with a proton that passes the proton criteria were hand-scanned and it was found that in the majority of cases the proton is knocked out of its parent atom in a deep inelastic scattering (DIS) interaction. In the DIS interactions there are also a number of gamma rays created, often via a π^0 decay, which then interact in the ECals close to the proton. This gamma ray interaction is mis-reconstructed as part of the proton track so when the E/p criterion is applied it is the energy of the proton and gamma ray rather than just the energy of the proton that is normalised to the proton momentum. This leads to the E/p being reconstructed as higher than it should be for the proton and so it passes the criterion. For the log-likelihood variables, positron and gamma ray showers are extremely similar as they are both electromagnetic and so are extremely difficult to separate; therefore,

in the case where a gamma shower has been reconstructed following a proton track the criteria on the ECal log-likelihood variables will also fail to remove the proton. The next largest source of protons which pass proton criteria is NC interactions which also produce a gamma ray in addition to knocking a proton out of its parent atom, similar to DIS interactions.

The high-momentum protons are produced by an approximately-equal mix of CCQE, CCRES and CCDIS interactions. These processes may produce a proton with momentum greater than 2000 MeV, a region where the proton criteria are not applied.
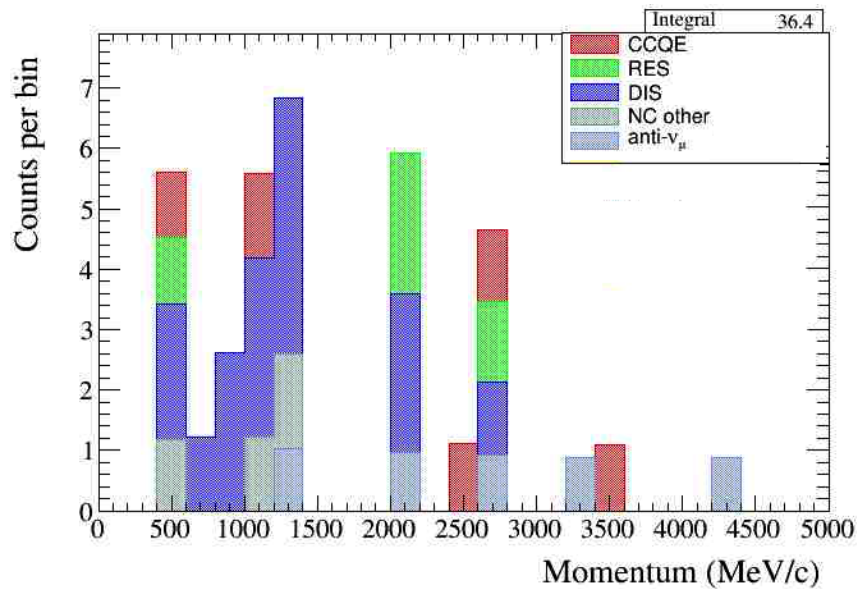
Figure 4.21: The MC prediction of the momentum of protons remaining in the $\bar{\nu}_e$ selection after applying the $\bar{\nu}_e$ selection criteria. These can be broken down into two categories: those protons with high momentum where, for the sake of efficiency, it is not worth applying the proton criteria (see Figures 4.11(a) and 4.11(b)) and those protons that manage to pass all the criteria. The colours show the proton production method via ν interactions.

4.5.2 Gamma Background

As in the ν_e selection, the sample in the $\bar{\nu}_e$ selection is dominated at low energy by positrons which originate from a gamma conversion where one of the e^+e^- pair, is not reconstructed rather than positrons from a $\bar{\nu}_e$ interaction. This background is the dominant background in the $\bar{\nu}_e$ selection comprising 39.5% of the total selected sample. This is also the case in the ν_e selection where it comprises $\sim22\%$ and the gamma background is described in more detail in Sections 7 and 8 of [73]. As can be seen in Figure 4.22, the biggest source of gamma events is DIS interactions where high-energy neutrino interactions produce showers of particles. The next largest source of gamma rays is from NC interactions where the gamma ray is usually produced from the decay of a π^0 which was produced in the interaction. A small number of gamma rays are produced by coherent pion production (COH), which is where the neutrino interacts with the nucleus as a whole rather than with one of its individual nucleons.

A brief study into possible methods to reduce the gamma background, specifically events where the gamma originated outside of the FGD fiducial volume, was made and it was discovered that the positrons produced in gamma events tend to have lower momenta than the positron from $\bar{\nu}_e$ CC interactions, and that the positrons produced by gamma rays through pair production have sightly higher angle with respect to the neutrino beam than positrons produced by $\bar{\nu}_e$ CC interactions. It was decided against increasing the momentum limit (criteria 3 in Table 4.1) and placing criteria on the angle with respect to the beam direction, because these two variables are used during the calculations of neutrino interaction cross sections and so placing criteria on them would limit the phase space were this selection to be used for a cross section measurement.
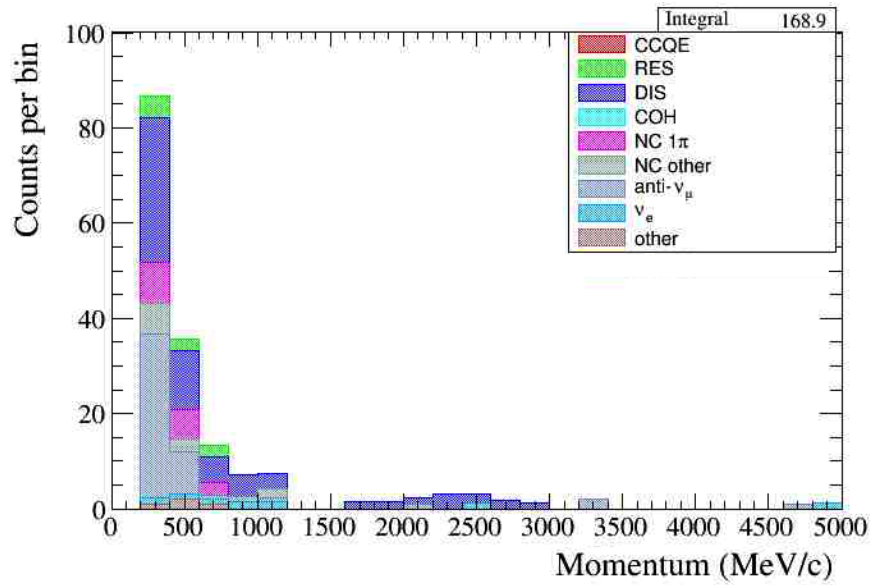
Figure 4.22: The MC prediction of the momentum of gamma rays in the $\bar{\nu}_e$ selection. It can be seen that one of the biggest sources of gamma rays is DIS interactions, with the second-biggest being NC interactions.

4.5.3 Other Backgrounds

Figure 4.23 shows the momentum of the other (non-proton and non-gamma) backgrounds remaining in the $\bar{\nu}_e$ sample after the selection is applied. As can be seen in Table 4.5, of the other backgrounds in the sample almost half (48.1% of the 11.9% of other background events) is made up of events where the highest-momentum particle belongs to a negative track. The reason that these events pass criterion 2 of Table 4.1 is that the highest-momentum reconstructed track in these events is often backwards-going, but is reconstructed as forward-going; hence, the track is assigned the wrong charge. This is because a track is assumed to be forward-going unless subdetector timing shows otherwise; however, on rate occasions a backwards-going particle has traversed multiple subdetectors in less time than the timing resolution of the subdetectors. For example a particle which leaves the BrECal, travels across the corner of TPC3 and then enters FGD2 which can occur in less than a nanosecond. Such a particle would then be reconstructed as

forward-going even though in reality it is backwards-going and assigned the wrong charge.

The remainder of the other background is predominantly π^+ and μ^+ which remain in the selection. The π^+ rejection rate is 99.7% and the μ^+ rejection rate is 99.9%.
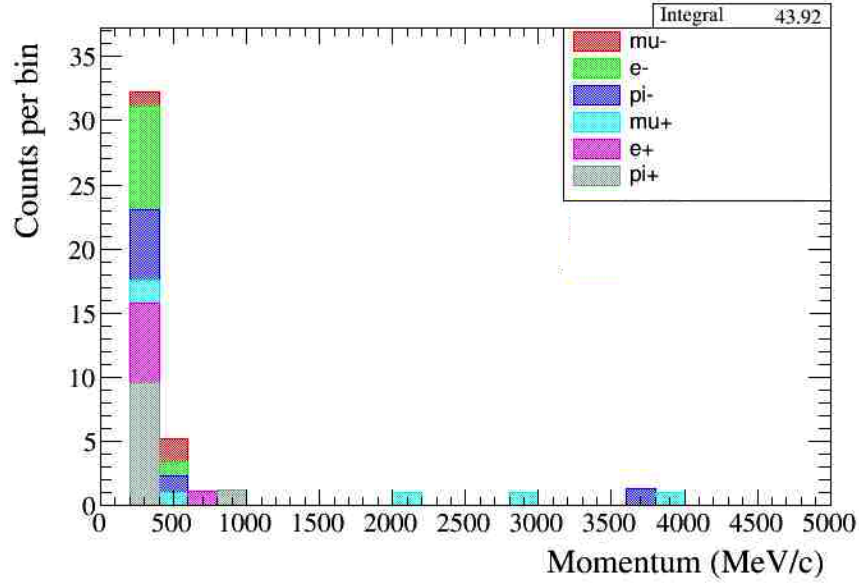
Figure 4.23: The momentum of the highest-momentum particle in the event for non-proton and non-gamma backgrounds, broken down by particle type. It can be seen that almost half of the other backgrounds (5.7% of the total sample) are from negatively-charged tracks which are from backwards-going particles reconstructed as forward-going and so assigned the wrong charge.

Particle	Percentage of other background
μ^-	8.6%
e^-	22.7%
π^-	16.8%
μ^+	14.1%
e^+	15.2%
π^+	22.5 %

Table 4.5: The breakdown of the "other background" category from Figure 4.23 by particle type.

4.6 Results with Observed Data

The $\bar{\nu}_e$ selection was finalised using MC as described above. In this section data
and MC are compared after all criteria have been applied and the properties of
the events which enter the $\bar{\nu}_e$ CC-inclusive sample are discussed. Applying all of
the selection criteria discussed in Section 4.2 and Section 4.3.2 to the ND280 an-
tineutrino data produces the sample shown in Figure 4.24, which shows reasonable
agreement between data and the NEUT MC simulation. In total 45 events were
selected in the data sample and 41.92 events were selected in the Monte Carlo sam-
ple when normalised by POT. The positrons in the events tend to be boosted in
the direction of the neutrino beam with the majority of positrons having a $\cos(\theta)$
[1] greater than 0.9 as shown by Figure 4.25. They also have the momentum distri-
bution shown in Figure 4.24, which peaks strongly in the low momentum region
around 200 MeV/c before tailing off; a second peak can be seen at 2000 MeV/c
which is due to the proton rejection criteria not being applied above 2000 MeV/c
which causes an efficiency increase for $\bar{\nu}_e$ but also increases the backgrounds. A
typical reconstructed signal event (from MC simulation) is shown in Figure 4.26,
where a single positron-like track exits FGD2 and then traverses TPC3 to shower
in the DsECal. The line shows the vertex and reconstructed track in TPC3; the
cone represents the reconstructed ECal shower in the DsECal.

Category	Composition
$\bar{\nu}_e$ CC	41.9%
Gamma background	39.5%
Proton background	6.3%
Other	12.3 %

Table 4.6: The composition of the final selected sample. The backgrounds are
broken down into proton and gamma backgrounds with the remaining backgrounds
being classed as other.

[1]θ is the angle between the z axis of the ND280 and the direction of the particle track as
measured by the TPC.
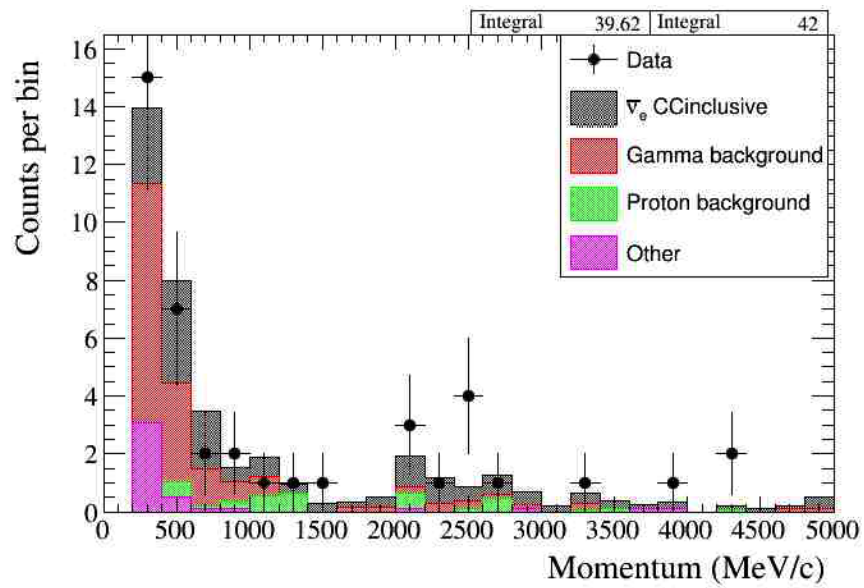
Figure 4.24: The momentum of the positron candidate in the $\bar{\nu}_e$ CC-inclusive sample after applying all selection criteria. The coloured histogram is MC and the points are data. Grey is the $\bar{\nu}_e$ CC signal, green is the proton background, red is the gamma background and other backgrounds are shown in purple.
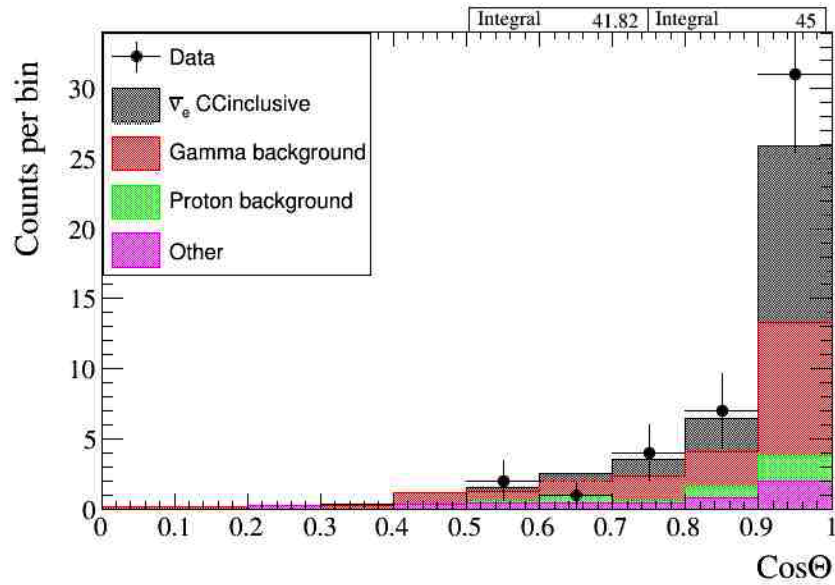
Figure 4.25: The $\bar{\nu}_e$ CC-inclusive sample after applying all the criteria as a function of the reconstructed $\cos(\theta)$ at the start of the candidate positron track. The coloured histogram is MC and the points are data. Grey is the $\bar{\nu}_e$ CC signal, green is the proton background, red is the gamma background and other backgrounds are shown in purple.
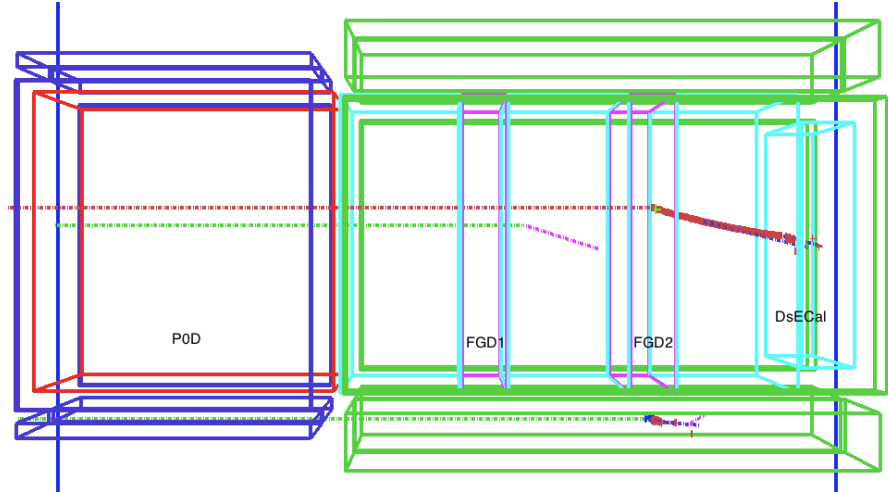
Figure 4.26: A MC simulated $\bar{\nu}_e$ signal event with the $\bar{\nu}_e$ interaction vertex in FGD2 and a component in the DsECal. The positron is produced in FGD2, traverses TPC3, then showers in the DsECal. The dashed red line represents the incoming $\bar{\nu}_e$ and the thick red line is the outgoing positron. The dashed green line represents a $\bar{\nu}_\mu$ which interacts in the magnet and produces a neutron which is represented by the dashed purple line.

Chapter 5

Systematic Uncertainties

In this Chapter the systematic uncertainties for the selection are discussed. Section 5.1 will discuss the systematic uncertainties due to the detector that are evaluated with the highland package in Section 5.1.1, and the ECal systematic uncertainties in Section 5.1.2. The systematic uncertainties due to the neutrino flux are covered in Section 5.2 and any other systematic uncertainties are discussed in Section 5.3. The total systematic uncertainty for the selection is covered in Section 5.4.

5.1   Detector Systematic Uncertainties

The highland package, discussed in Section 4.1, includes the evaluation of several systematic uncertainties. These are discussed in Section 5.1.1. The ECal systematics were calculated outside the highland package using a Gaussian smearing technique which will be discussed in Section 5.1.2.

5.1.1   Systematic Uncertainties Calculated in Highland

There are two types of systematic uncertainties that are evaluated in highland: variations and weights. Systematic variations modify the event properties, such

as the particle's momentum, the deposited energy, etc. Weights only affect the final weights of the event in our sample, but leave the whole event untouched. Thus, after applying a systematic variation, the event selection needs to be redone. This is not the case for the systematic weights. Systematic effects that affect a continuous property of the event (momentum resolution, momentum scale, TPC PID, FGD PID) must be implemented as variations. Systematic effects that affect a binary property of the event (charge confusion, tracking efficiencies, etc) can be implemented either as weights or variations. Systematic effects that affect only the event normalization (FGD mass, pile-up, etc) can only be implemented as weights.

The detector uncertainties currently implemented in highland are:

- Momentum Scale: The systematic uncertainty associated with the overall scale of the TPC momentum measurement and how the TPC-measured momentum differs from true momentum. This arises from uncertainties in the overall magnetic field strength of the ND280 magnet and includes uncertainties from misalignment of the Hall probes and intrinsic uncertainty of the Hall probes used to measure the magnetic field.

- Momentum Resolution: The systematic uncertainty on the resolution of the TPC momentum measurement. This is measured by comparing the inverse of the transverse momentum between two TPCs, after accounting for energy lost in the FGD between them.

- TPC PID: The systematic uncertainty associated with the TPC PID variables. As was covered in Section 4.2 the TPC PID depends on dE/dx; therefore, the systematic uncertainty for both the energy resolution and the energy scale must be calculated and included. As dE/dx differs for different particles, this systematic is calculated separately for electrons, muons/pions (which have similar dE/dx so are treated the same) and protons. The sys-

tematic uncertainties are calculated by selecting samples with high purity of each specific particle type without utilising the TPC PID. The TPC pulls are then examined for each particle sample and ideally would be a Gaussian distribution of mean 0 and width 1. Differences in the mean imply a systematic uncertainty on the energy scale and differences in the width imply a systematic uncertainty on the energy resolution.

- FGD PID: The systematic uncertainty associated with the FGD PID variables. The TPC PID is used to select a control sample of particles which stop in the FGDs. As with the TPC PID systematic uncertainty a Gaussian distribution is then fitted to each of the pulls and differences between data and MC mean and width values are used to calculate the systematic uncertainty.

- Charge Confusion: The systematic uncertainty associated with the charge determination. This is calculated by looking at tracks which cross all three TPCs. The probability of all three TPCs reconstructing the same charge is then related to the probability of misidentifying the charge.

- TPC-FGD Track Matching: The systematic uncertainty associated with matching tracks reconstructed in the FGDs with the correct reconstructed TPC track. This is measured by using a sample of through-going muons where it is assumed that tracks in two TPCs must have an FGD track between them. If there is a match between the FGD segment and the segment in the downstream TPC then the track matching is assumed to be good.

- Fiducial Volume: The systematic uncertainty due to the FGD fiducial-volume and out-of-fiducial-volume events. A sample of events is created for a series of 15 fiducial-volume sizes (7 larger fiducial volumes, 7 smaller fiducial volumes and the fiducial volume used in the selection). The fraction of out-

of-fiducial-volume events in the final sample for each fiducial volume is then calculated. The standard deviation in the fraction of out-of-fiducial-volume events is then used as the systematic uncertainty.

- FGD Mass: The systematic uncertainty associated with the FGD mass, which is computed from the uncertainties on the size and composition of the FGD components.

- Michel Electron: The systematic uncertainty due to electrons which were produced during muon decays. A sample of cosmic muons that stop in the FGDs is compiled and the efficiency with which the FGDs identify Michel electrons is compared for data and MC.

- Sand Muon: The systematic uncertainty due to sand muons, which are muons that originate from neutrino interactions outside the detector, passing the selection criteria. These are not modeled in the beam MC; however, it is very unlikely that a sand muon will enter the selection due to the high muon rejection rate and as such this systematic uncertainty is small.

- Pile-up: The systematic uncertainty due to multiple neutrino interactions in a single beam window. This also includes the systematic uncertainty due to sand muons triggering one of the veto criteria.

- TPC Cluster Efficiency: The systematic uncertainty associated with the TPC reconstruction reconstructing TPC clusters (hits) where they are expected. This systematic uncertainty is computed separately for Micromegas pads in the centre of the Micromegas modules and for Micromegas pads on the edges of the Micromegas modules, because the pads on the edges of the modules are affected by edge effects.

These are also listed in Table 5.1 along with the method used to calculate

them (variations or weight). The total systematic uncertainty due to these sys-
tematic uncertainties is 6.5%, obtained by combining the individual uncertainties
in quadrature.

The total systematic uncertainty due to these systematic effects is shown in
Figure 5.1 versus the momentum of the positron candidate and in Figure 5.2 as a
function of the cosine of the angle of the positron candidate's track with respect to
the z-axis of the detector. From Figure 5.1 it can be seen that the uncertainty is
smaller in the low momentum region which is the region with the most events that
pass the selection criteria, and from Figure 5.2 it can be seen that the uncertainty
is smallest for events where the candidate positron's track has a small angle with
respect to the z-axis. This is again the region with the most events which pass the
selection.
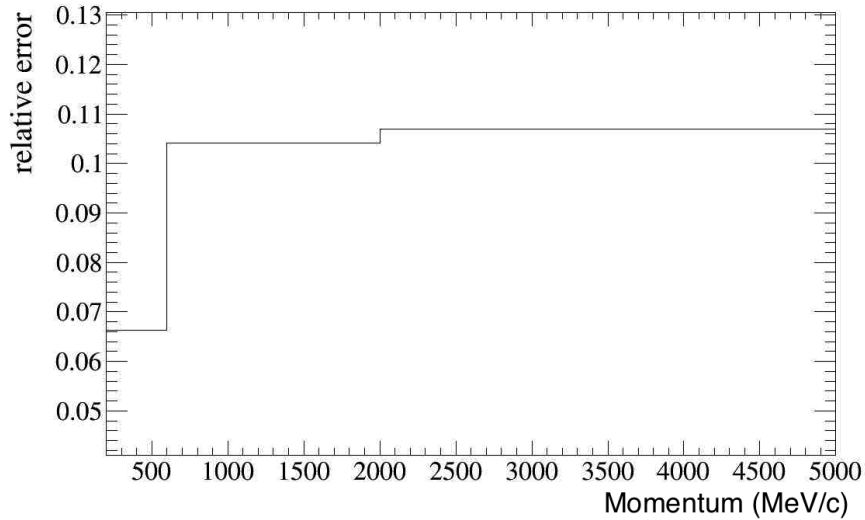
Figure 5.1: The systematic uncertainties associated with the detector as shown
in Table 5.1 and computed in highland versus the momentum of the candidate
positron in a selected event. This plot shows how the uncertainties change between
the low momentum region (below where the proton rejection criteria are applied),
the region of the proton criteria and in the high momentum region (above where
the proton criteria are applied).

Systematic Uncertainties	Systematic Type	Uncertainty (%)
Momentum Scale	variation	0.07
Momentum Resolution	variation	0.4
TPC PID	variation	1.8
FGD PID	variation	<0.001
Charge Confusion	weight	0.4
TPC-FGD Track Matching	weight	1.1
Fiducial Volume	weight	5.6
Pile-up	weight	2.4
FGD Mass	weight	0.35
Michel Electron	weight	0.58
Sand Muon	weight	<0.001
TPC Cluster Efficiency	weight	0.004
Total		6.5

Table 5.1: The systematic uncertainties included in Figure 5.1 as determined by the highland package.
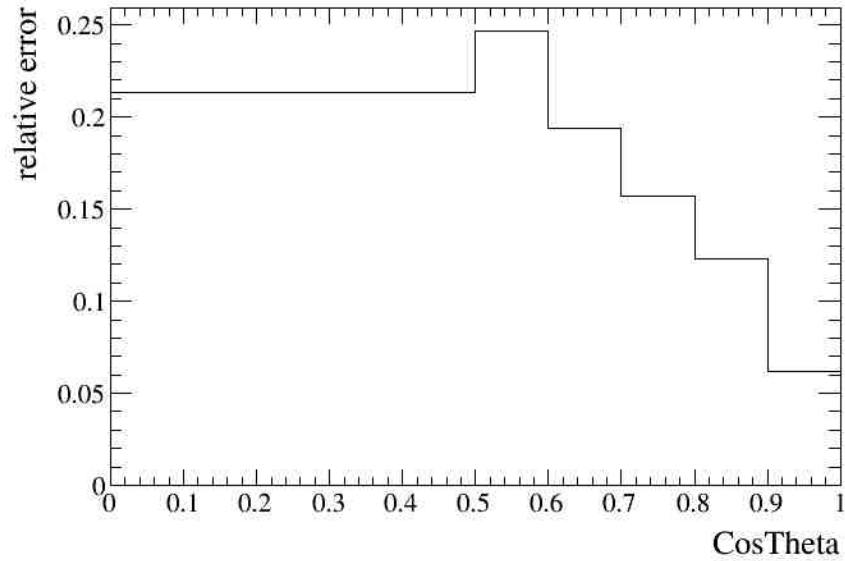
Figure 5.2: The systematic uncertainties associated with the detector as shown in Table 5.1 and computed using highland as a function of the cosine of the angle of the positron candidate's track with respect to the z-axis.

5.1.2   ECal Variable Systematic Uncertainties

While the highland package evaluates the uncertainties due to the FGDs and TPCs (see Section 5.1.1), the evaluation of the systematic uncertainties for the DsECal

and BrECal has not yet been implemented in highland. In order to evaluate the uncertainties due to the ECal variables and the criteria placed upon them, a Gaussian smearing technique was used. In this technique, the histogram of the Monte Carlo simulation is convolved with a Gaussian distribution in order to produce a smeared histogram. The smeared histogram is then compared to the real data and the χ^2 of the fit calculated as in Equation 5.1.

$$\chi^2 = \sum_{k=1}^{n} \frac{(O_k - E_k)^2}{E_k} \tag{5.1}$$

where O_k is the observed number of events in bin k, E_k is the expected number of events in bin k, and n is the total number of bins in the histogram.

A grid search is then performed using many Gaussian distributions with a mean of -5 to 5 and width from 0 to 10, in order to find the Gaussian distribution which produces the smeared histogram that best fits the data. The exception to this is the E/p variable where a width of 0 to 1 was used due to the variable's smaller domain. The difference in the number of events removed by a criterion before and after the variable is smeared is then calculated and divided by the total number of events in the histogram to give the percentage systematic uncertainty due to applying that criterion.

The Gaussian parameters used for each variable and the change in the absolute number of events removed by a criterion are shown in Table 5.2. The smeared and unsmeared distributions compared to data for each of the ECal variables can be seen in Figures 5.3(a) to 5.8(b). The systematic uncertainty for each of the ECal variables along with the total ECal systematic uncertainty is shown in Table 5.3 and is the average of the DsECal and BrECal systematic uncertainties weighted by the number of events.

Due to the small quantity of antineutrino data available neutrino data and Monte Carlo was used to evaluate the ECal systematics. This should have a neg-

ligible effect on the systematic evaluation as the ECal PID is charge independent and the same backgrounds are present in the selection in both neutrino beam mode and antineutrino beam mode.
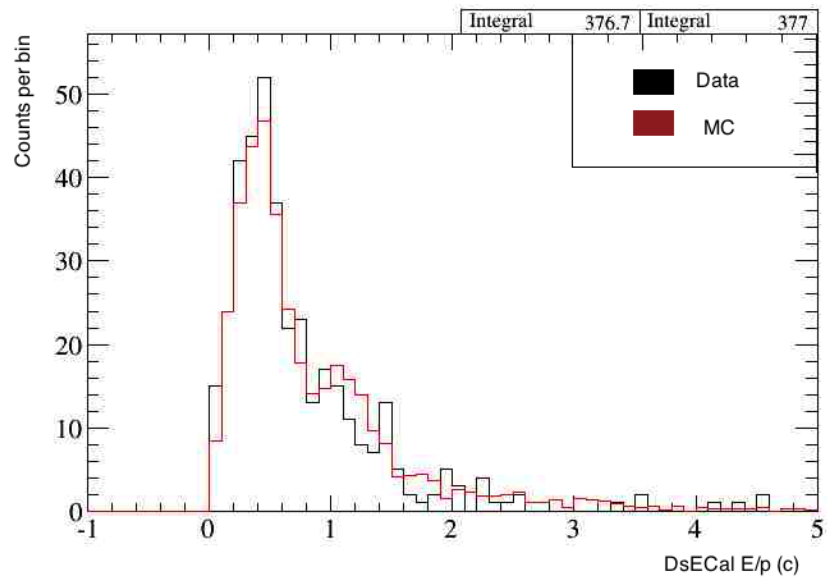
(a)
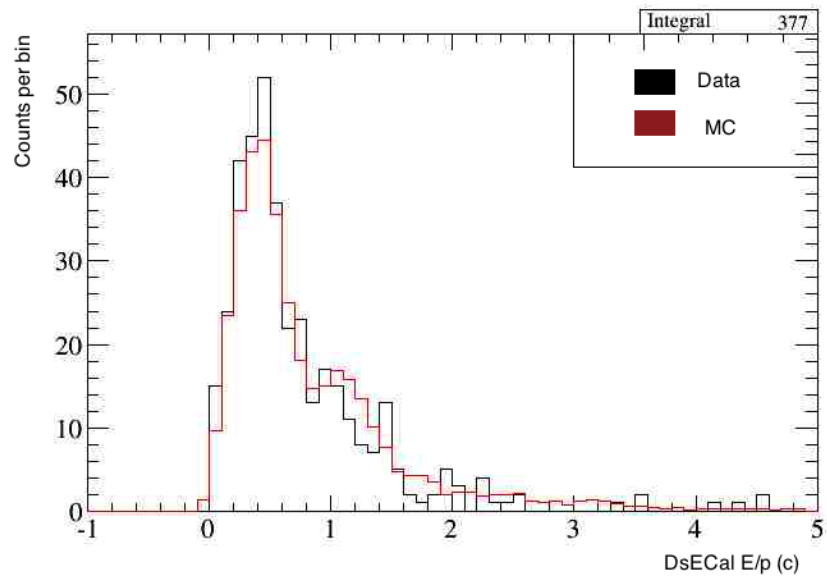
(b)

Figure 5.3: Before (a) and after (b) the smearing process for DsECal E/p. The properties of the Gaussian distribution used for smearing are shown in Table 5.2 and the final calculated uncertainty is shown in Table 5.3.

Variable	Gaussian Sigma	Gaussian Mean	Δ Events	χ^2/NDoF
DsECal E/P	0.05	0	- 1.009	57.65/60
DsECal EMHIP	2.6	0.4	- 3.358	52.22/65
DsECal MIPPION	3.1	-1.6	+ 17.598	61.53/75
BrECal E/P	0	0	0	33.40/60
BrECal EMHIP	0.3	0.6	- 4.75	33.70/65
BrECal MIPPION	4.0	0.4	+ 3.04	37.59/65

Table 5.2: The DsECal and BrECal variables for which the systematic uncertainty has been calculated along with the parameters of the Gaussian distribution which generated the best-fitting distribution during the smearing process. The change in the absolute number of events removed by a criterion after smearing is also included.

Variable	Systematic Error (%)
DsECal E/p	0.20
DsECal EMHIP	0.87
DsECal MIPPION	4.56
BrECal E/p	0.01
BrECal EMHIP	3.01
BrECal MIPPION	1.94
DsECal total	4.65
BrECal total	3.58
ECal combined total	4.49

Table 5.3: The systematic uncertainties evaluated for the DsECal and BrECal and the total systematic uncertainty for the ECal variables.
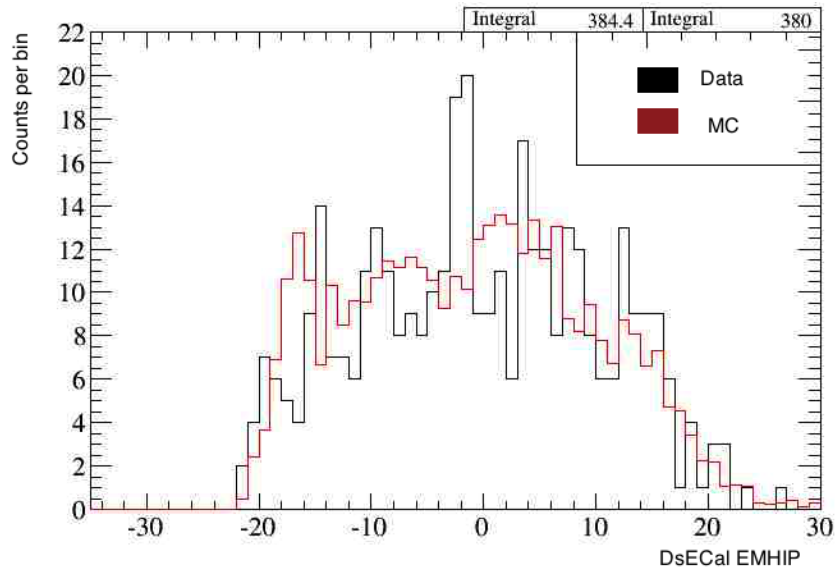
(a)
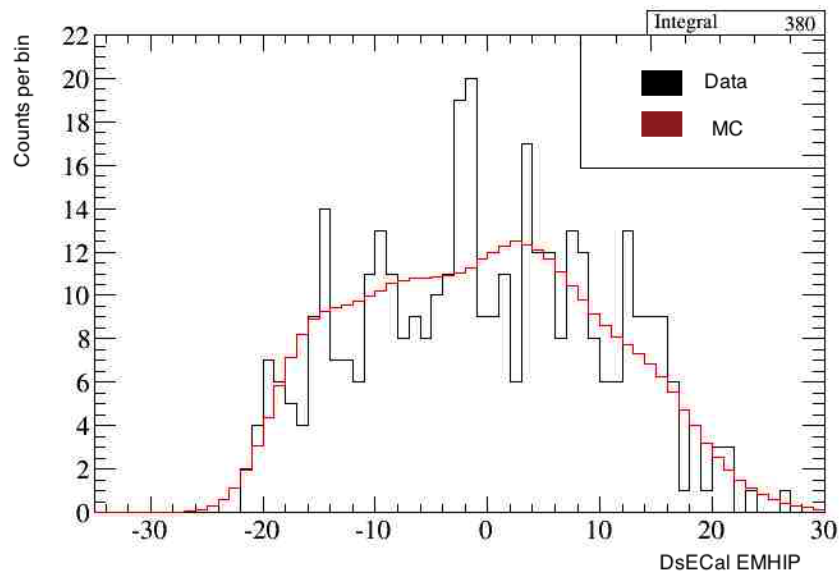
(b)

Figure 5.4: Before (a) and after (b) the smearing process for DsECal EMHIP. The properties of the Gaussian distribution used for smearing are shown in Table 5.2 and the final calculated uncertainty is shown in Table 5.3.
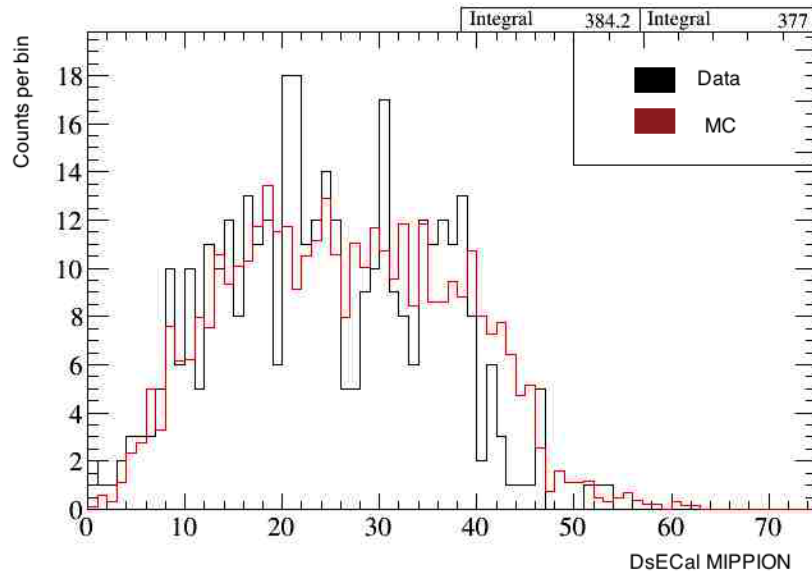
(a)
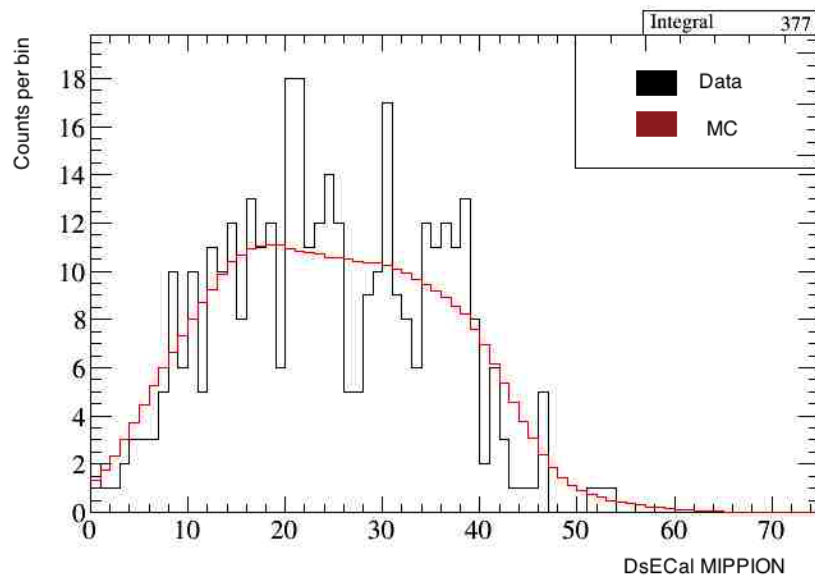
(b)

Figure 5.5: Before (a) and after (b) the smearing process for DsECal MIPION. The properties of the Gaussian distribution used for smearing are shown in Table 5.2 and the final calculated uncertainty is shown in Table 5.3.
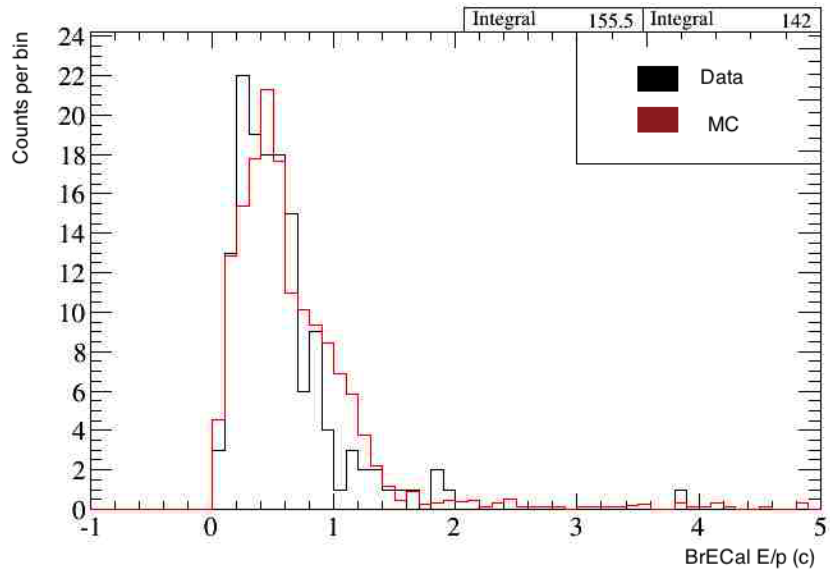
(a)
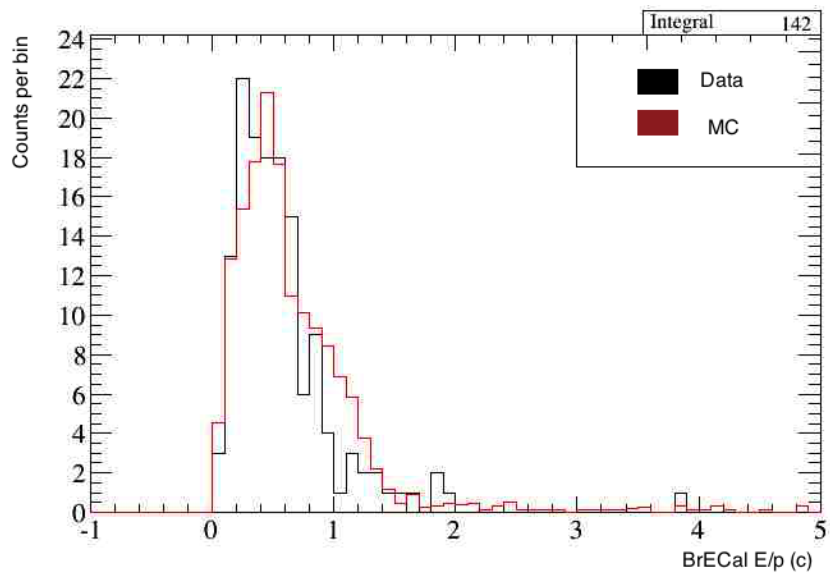
(b)

Figure 5.6: Before (a) and after (b) the smearing process for BrECal E/p. The properties of the Gaussian distribution used for smearing are shown in Table 5.2 and the final calculated uncertainty is shown in Table 5.3.
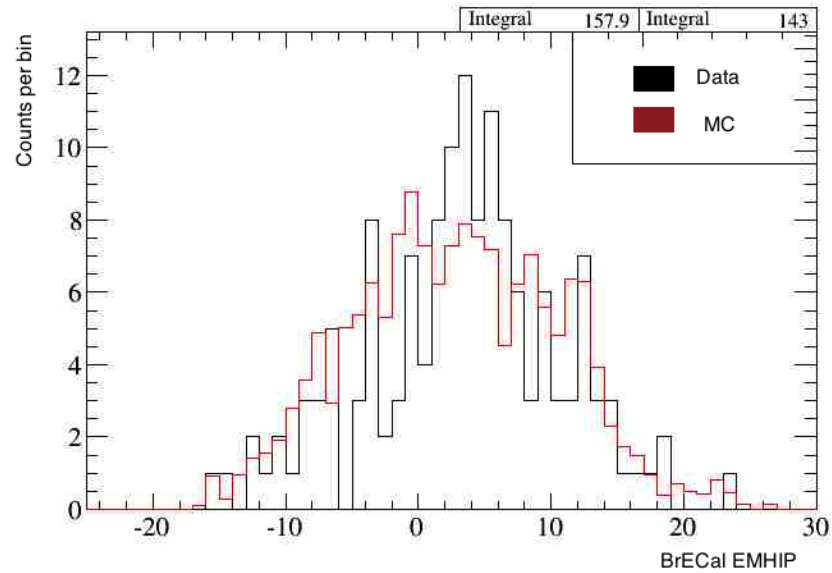
(a)
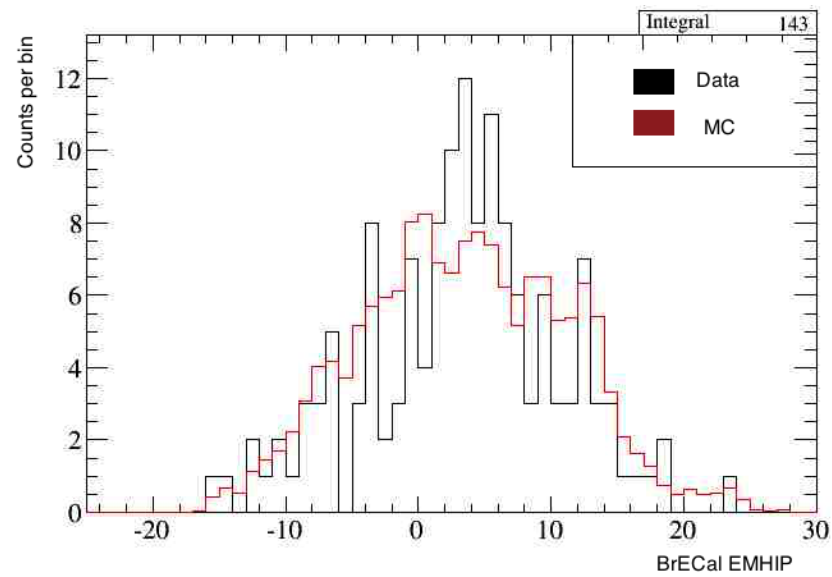
(b)

Figure 5.7: Before (a) and after (b) the smearing process for BrECal EMHIP. The properties of the Gaussian distribution used for smearing are shown in Table 5.2 and the final calculated uncertainty is shown in Table 5.3.
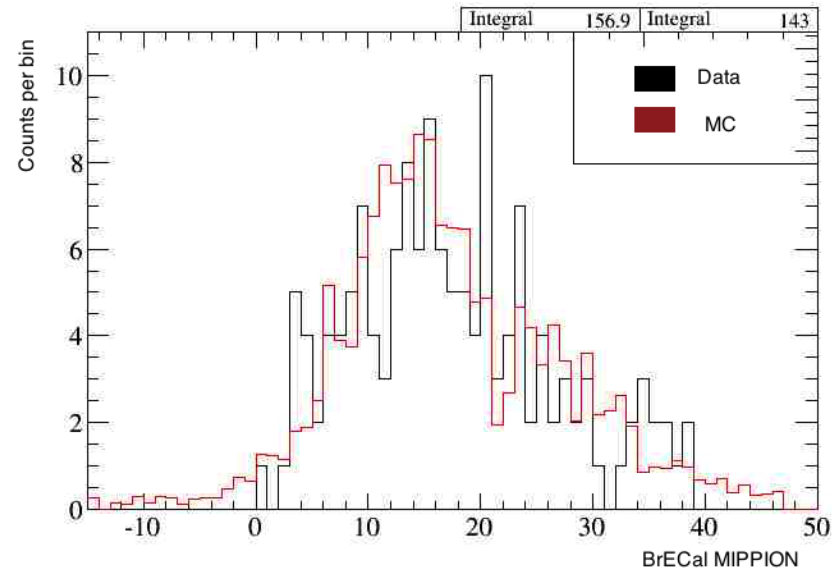
(a)
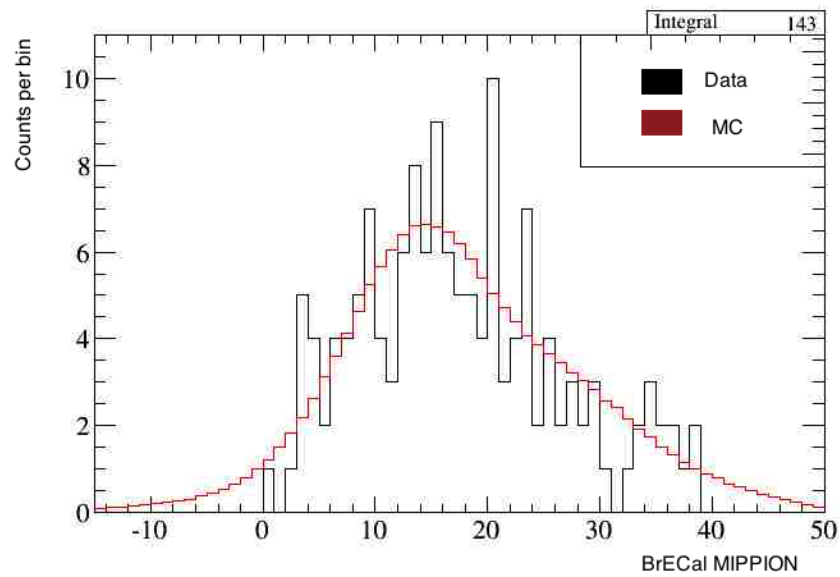
(b)

Figure 5.8: Before (a) and after (b) the smearing process for BrECal MIPION. The properties of the Gaussian distribution used for smearing are shown in Table 5.2 and the final calculated uncertainty is shown in Table 5.3.

5.2 Flux Systematic Uncertainty

In order to assess the uncertainty on the ND280 neutrino flux, the covariance matrix that encodes the uncertainty on the flux mode must be varied about its normal values. The T2K beam group provide a covariance matrix that has 25 bins for both ND280 and SK, for both neutrino and antineutrino mode running, giving a matrix with 100 rows and columns. For the purposes of this analysis only the 25 by 25 submatrix corresponding to ND280 antineutrino mode is required.

This matrix has the following energy bins (MeV):

- 11 $\bar{\nu}_\mu$: 0, 400, 500, 600, 700, 1000, 1500, 2500, 3500, 5000, 7000, 30000.

- 5 ν_μ: 0, 700, 1000, 1500, 2500, 30000.

- 7 $\bar{\nu}_e$: 0, 500, 700, 800, 1500, 2500, 4000, 30000.

- 2 ν_e: 0, 2500, 30000.

and can be seen in Figure 5.9(a) [84].

This matrix is then Cholesky decomposed into a lower triangle matrix (Figure 5.9(b)) and the conjugate transpose of the lower matrix, which is not used.

The lower triangle matrix is multiplied by a vector of random numbers from a Gaussian distribution of mean 0 and width 1. This gives a new flux matrix to use in a toy experiment for each neutrino flavour and energy bin. This process is repeated for many toy experiments. The flux uncertainty is then found by summing the difference between the number of events in the selection and the number of events in a toy experiment over all toy experiments, and then normalising by the number of toy experiments. The results of this can be seen in Figure 5.10. The systematic uncertainty due to the flux is 9.1%.
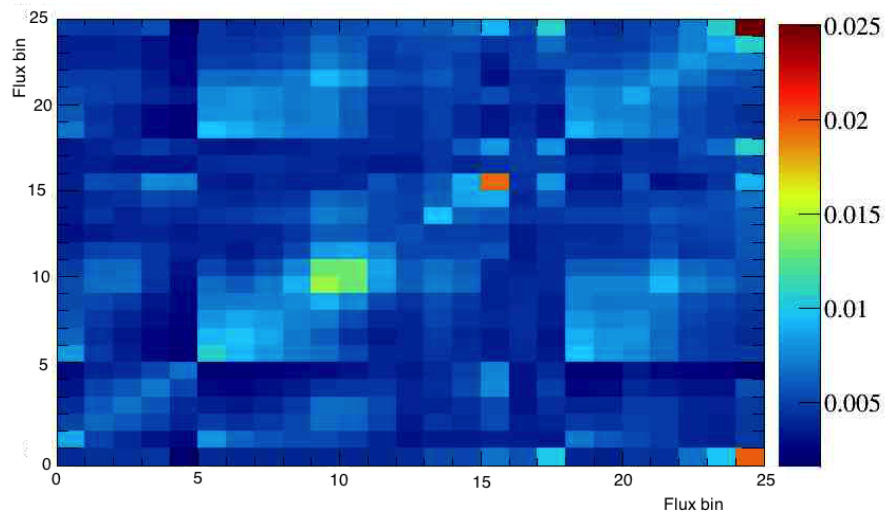
(a)
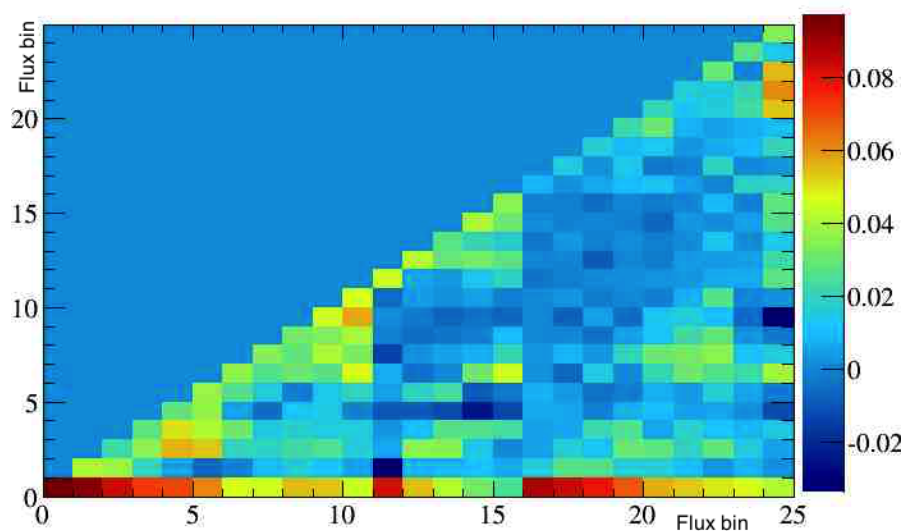
(b)

Figure 5.9: The covariance matrix for the antineutrino flux at the ND280 (a) and the lower triangle matrix from Cholesky decomposition (b).

5.3   Other Systematic Uncertainties

If there is a difference in efficiency between data and MC for matching components of a track between a TPC and one of the ECals, the number of events in a selection
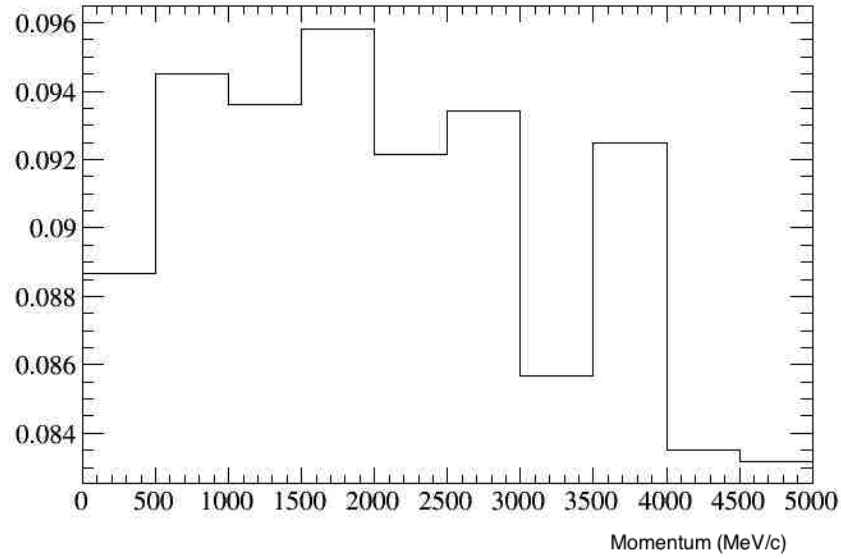
Figure 5.10: The systematic uncertainty due to the flux versus the momentum of the positron candidate.

using the TPCs and ECals will be different for data and Monte Carlo. To take this into account, a systematic uncertainty is calculated for tracks entering the BrECal or the DsECal from a TPC.

The systematic uncertainty is calculated by first using TPC PID to create a sample of electrons and positrons. The end position in the most downstream TPC is then used to determine whether a particle enters the ECals. The matching efficiency is then defined as:

$$\epsilon = \frac{\text{Tracks which enter the ECals and have a matched ECal component}}{\text{Tracks which enter the ECals}}. \quad (5.2)$$

The systematic uncertainty is then calculated from the matching efficiency difference between data and MC and the statistical uncertainties on the efficiencies.

The TPC-ECal matching systematic uncertainty is 0.7% for both the DsECal and BrECal. The variation of the uncertainties with momentum is shown in Figure

5.11(a) for the DsECal and Figure 5.11(b) for the BrECal.
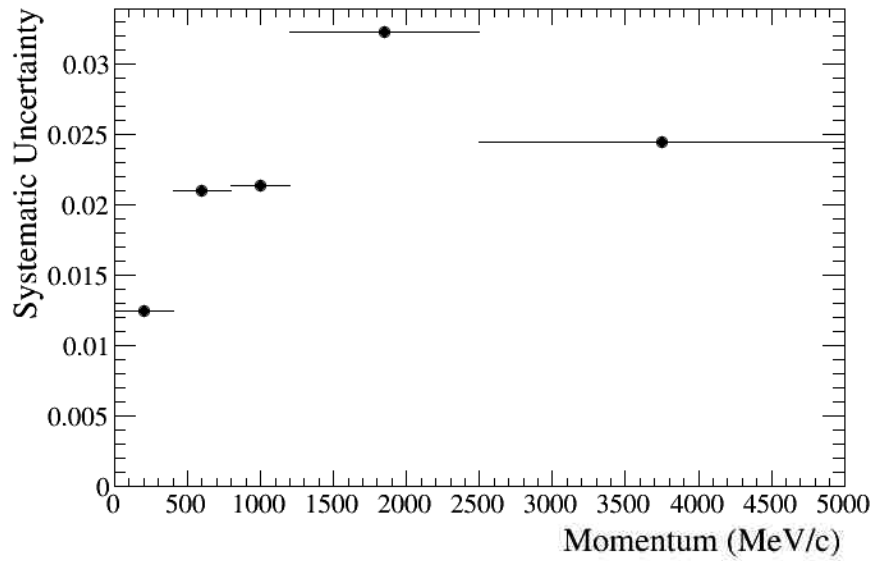
(a)
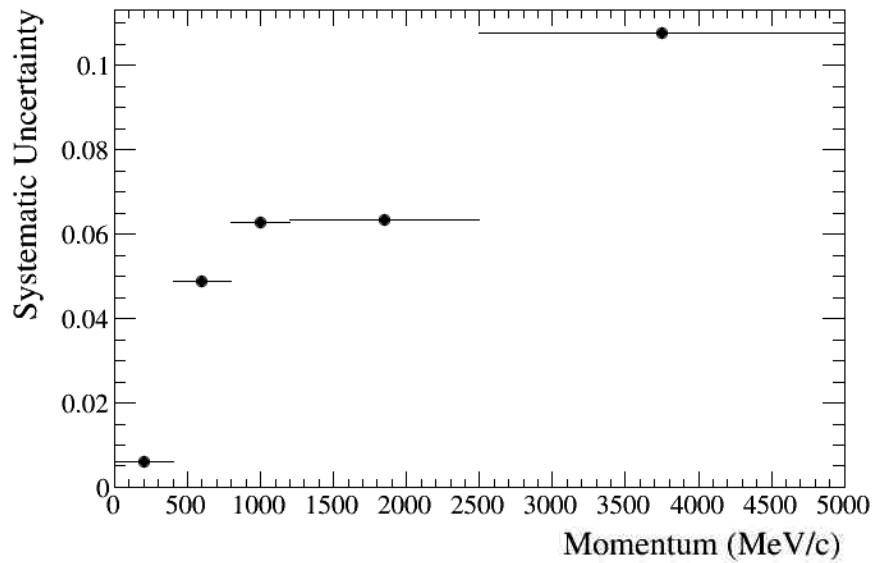
(b)

Figure 5.11: The systematic uncertainty for matching electron-like tracks in the TPC to an ECal segment as a function of the particle momentum. Figure 5.11(a) shows the fractional uncertainties for the DsECal and Figure 5.11(b) shows the fractional uncertainties for the BrECal.

5.4 Total Systematic Uncertainty

The total systematic uncertainty is 12.1%. The largest contribution to the systematic uncertainty is from the neutrino flux which has an uncertainty of 9.1%, with the ECal PID uncertainty the second-largest contributor at 4.5% as can be seen in Table 5.4. This level of systematic uncertainty is acceptable at the moment as T2K has just begun antineutrino running and so data is limited; however, as more data is gathered a greater understanding of the uncertainties presented here will need to be gained especially for the flux which is the largest contributor to the uncertainty. This can be done by improving our understanding of particle interactions in the target and the horns surrounding it, which is one of the aims of the NA61 experiment [79].

Systematic Uncertainty	Uncertainty (%)
Highland Systematic Uncertainties	6.5
TPC-ECal matching	0.7
ECal PID variables	4.5
Flux	9.1
Total Systematic Uncertainty	12.1

Table 5.4: All systematic uncertainties evaluated and the total systematic uncertainty for the analysis where the uncertainties have been added in quadrature.

Chapter 6

Conclusions

For this analysis, a cut-based selection has been developed for Charged-Current $\bar{\nu}_e$ interactions in the Fine-Grained Detectors of the ND280, the T2K near detector, in order to measure the $\bar{\nu}_e$ contamination in the T2K antineutrino beam. The selection imposed criteria on both the TPC and ECal PID and also used a variable combining TPC and ECal information, E/p.

The main challenge of developing a $\bar{\nu}_e$ CC selection was the removal of the proton background (Figure 4.7) which was still present in the selection after TPC PID was applied. To remove these protons ECal PID was used as TPC PID is unable to distinguish between protons and positrons at certain momenta (Figure 4.6). The variable with the strongest discriminating power between positrons and protons in the selection is E/p, which was able to differentiate between positrons and protons due to the positrons having much greater kinetic energy than protons while, due to the TPC criteria already applied, their momenta are similar. After application of all criteria, the $\bar{\nu}_e$ CC selection has a purity of $(41.9 \pm 2.4)\%$ and an efficiency of $(27.1 \pm 1.7)\%$.

To measure the $\bar{\nu}_e$ contamination in the T2K antineutrino beam, the analysis used antineutrino data from T2K run 5 and run 6 (from 21st May 2014 up to 29th

November 2014) which was reweighted with the 13a flux reweighting produced in October 2014. This data was compared to the NEUT MC simulation.

In total 45 events were selected in the data sample. When normalised by POT 41.92 events were selected in the Monte Carlo sample of which approximately 17.56 events are genuine $\bar{\nu}_e$ CC interactions with the remaining 24.36 events being background events. This then gives a data to MC ratio for the $\bar{\nu}_e$ content of the T2K antineutrino beam mode of:

$$\frac{data}{Monte\ Carlo} = 1.07 \pm 0.16(stat.) \pm 0.13(syst.) = 1.07 \pm 0.21 \qquad (6.1)$$

It is important that T2K has a good understanding of the $\bar{\nu}_e$ component of its antineutrino beam as $\bar{\nu}_e$ present in the T2K antineutrino beam before oscillation are the primary background in any T2K $\bar{\nu}_\mu \rightarrow \bar{\nu}_e$ appearance results. This analysis demonstrates that the data and MC are consistent; hence, we can be assured that T2K has a good understanding of the $\bar{\nu}_e$ component of the antineutrino beam, which gives us confidence in any future δ_{cp} measurements made using antineutrino data. Elements of this selection are being used to select a sample in order to measure the $\bar{\nu}_e$ cross section on carbon in the ND280.

As a cross-check on the result, a theoretical prediction was calculated directly using the average flux and cross-section of the T2K beam. For a theoretical $\bar{\nu}_e$ CC cross section of 0.30×10^{-38} cm^2/nucleon [85]and by taking the total $\bar{\nu}_e$ flux of 1.6×10^{11} cm^2/10^{21}POT [78], we can calculate the expected total number of $\bar{\nu}_e$ interactions in the ND280. For the 2.2 tonne FGDs this gives 60.7 $\bar{\nu}_e$ CC interactions in the 9.549×10^{19} POT used in this analysis which is in agreement with the data measurement which gives 69.5 $\pm$ 10.3 (stat.) when the efficiency and purity of the selection are taken into account.

Though the statistics available for this analysis are too small to make a reliable cross section measurement, the agreement between data and the theoretical pre-

diction of the $\bar{\nu}_e$ CC cross section demonstrates that the theory has has no large discrepancies from reality. Future analyses with access to more data and with improved systematic uncertainties will be able to test the theoretical cross section predictions more thoroughly, including testing the differences between $\bar{\nu}_e$ and $\bar{\nu}_\mu$ CC interactions at the GeV energy scale, which is a powerful method of testing the theory of neutrino interactions.

Appendix A

The Selection in Neutrino Beam Mode

As there is also some $\bar{\nu}_e$ contamination in neutrino beam mode this contamination should also be measured. This would require a retuning of the selection criteria developed in this work for the antineutrino beam mode and so is beyond the scope of this thesis. In neutrino beam mode there are significantly fewer $\bar{\nu}_e$ interactions due to the neutrino beam having a much smaller antineutrino contamination than the antineutrino beam has neutrino contamination. The kinematic distribution of the $\bar{\nu}_e$ interactions is also different as, unlike in the antineutrino beam mode where $\bar{\nu}_e$ contamination comes from both μ^- and K^- decays, in neutrino beam mode the $\bar{\nu}_e$ contamination only comes from K^- decays. As such, it is much harder to separate the $\bar{\nu}_e$ signal from the increased percentage of proton and gamma background events in neutrino beam mode.

Each of the requirements used to reject protons in the antineutrino beam mode needs to be re-optimised for a neutrino beam mode selection; however, there was insufficient time to perform this task. The variable plots for the selection in neutrino beam mode are shown in Figures A.1 to A.3. The arrows on the plots show

the values used in the $\bar{\nu}_e$ antineutrino beam mode selection, which would need to be retuned were this selection to be used for a measurement of the $\bar{\nu}_e$ contamination in neutrino beam mode. Using the values optimised for the antineutrino mode selection gives the sample shown in Figure A.6 which is 12.3% pure in $\bar{\nu}_e$ CC interactions, significantly lower than the purity of $(41.9 \pm 2.4)\%$ achieved in the antineutrino mode. The main reason for the lower purity is that there is a much lower percentage of $\bar{\nu}_e$ in the neutrino beam compared to the antineutrino beam and as both the largest backgrounds (the gamma and proton backgrounds) can be produced by ν_μ CC interactions, the $\bar{\nu}_e$ signal to background ratio is significantly higher. Another reason for the lower purity is that the proton background tails out to higher values of momentum space in the neutrino beam mode sample as can be seen in Figure A.4(a), Figure A.4(b) and Figure A.5, likely due to the increased number of neutrino CC interactions which produce a final state proton. The purity of the sample would be improved if the selection was retuned specifically for neutrino data; however, it would likely still be significantly lower than the purity of the antineutrino beam sample due to the extra difficulties posed when selecting $\bar{\nu}_e$ CC interactions from the neutrino beam. The efficiency of the sample is also reduced at 21.6%, which is smaller than the efficiency of the selection in antineutrino mode of $(27.1 \pm 1.7)\%$.
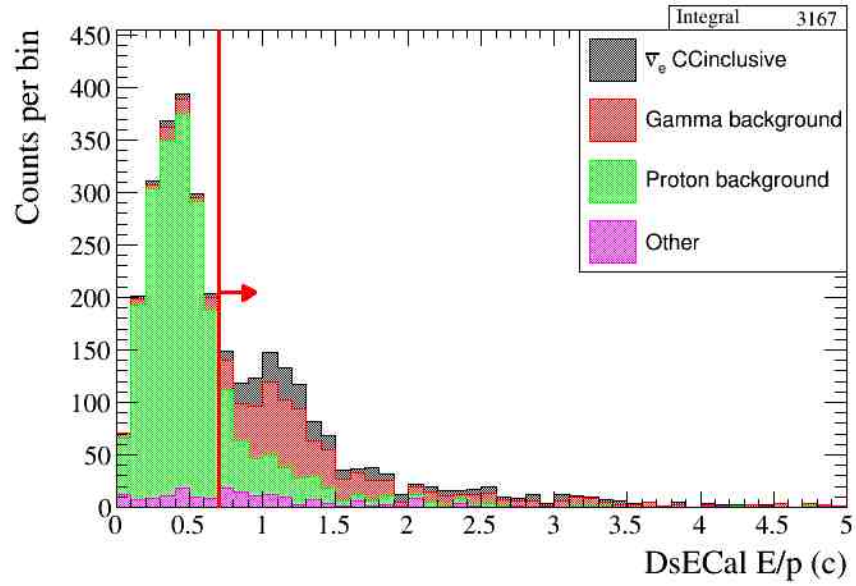
(a)
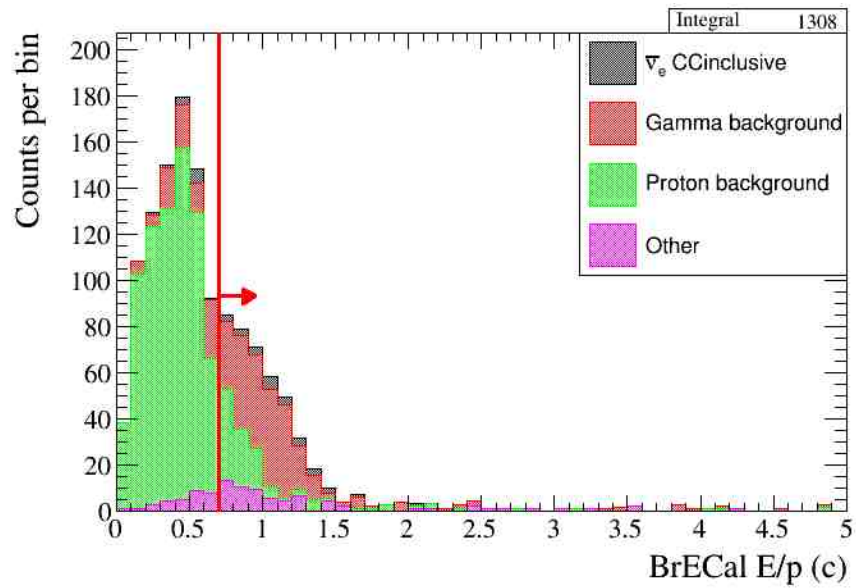
(b)

Figure A.1: E/p for the DsECal (a) and the BrECal (b) in neutrino beam mode. The arrows indicate the selected events. The coloured histogram is MC, grey is the $\bar{\nu}_e$ CC signal, green is the proton background, red is the gamma background and other backgrounds are shown in purple.
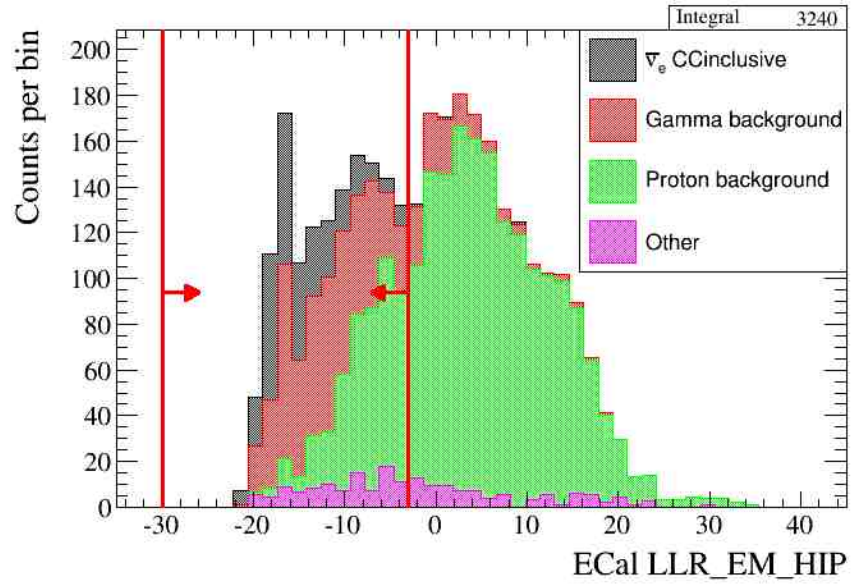
(a)
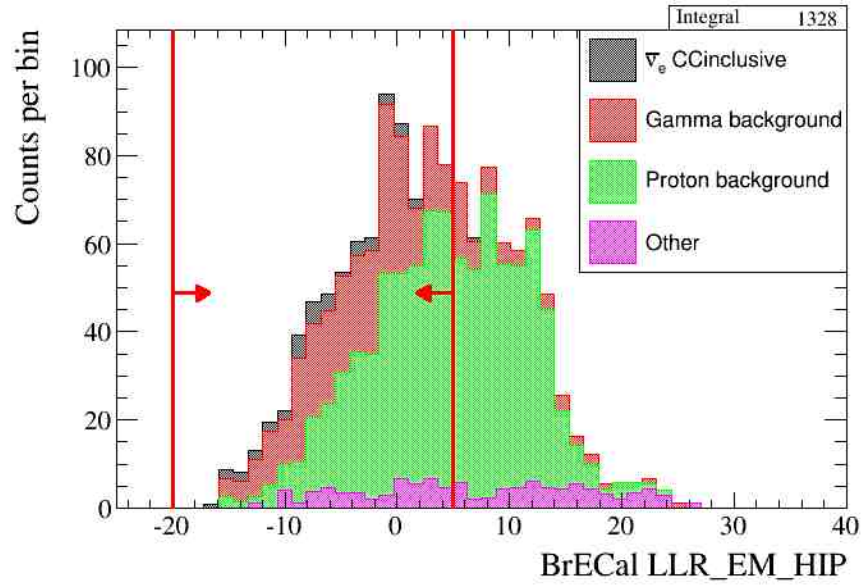
(b)

Figure A.2: LLR_EM_HIP for the DsECal (a) and BrECal (b) in neutrino beam mode. The arrows indicate the selected events. The coloured histogram is MC, grey is the $\bar{\nu}_e$ CC signal, green is the proton background, red is the gamma background and other backgrounds are shown in purple.
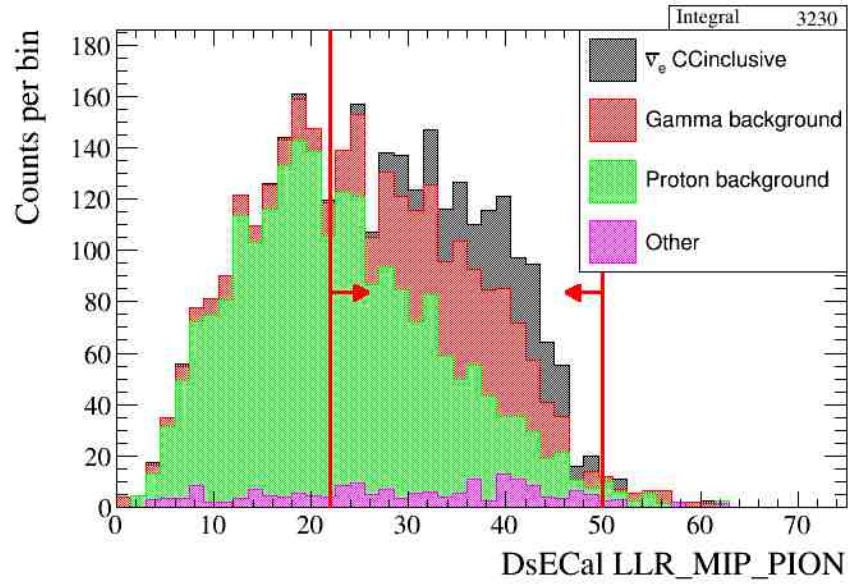
(a)
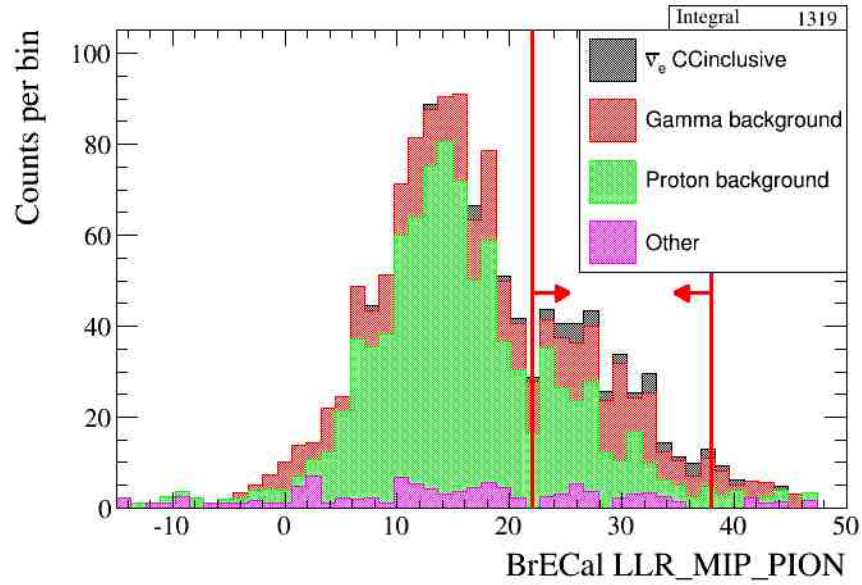
(b)

Figure A.3: LLR_MIP_PION for the DsECal (a) and BrECal (b) in neutrino beam mode. The arrows indicate the selected events. The coloured histogram is MC, grey is the $\bar{\nu}_e$ CC signal, green is the proton background, red is the gamma background and other backgrounds are shown in purple.
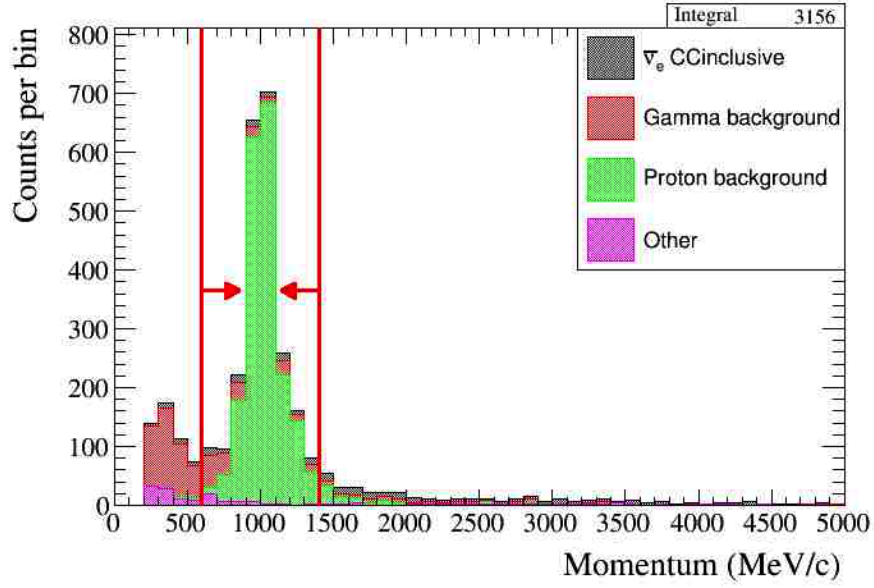
(a)
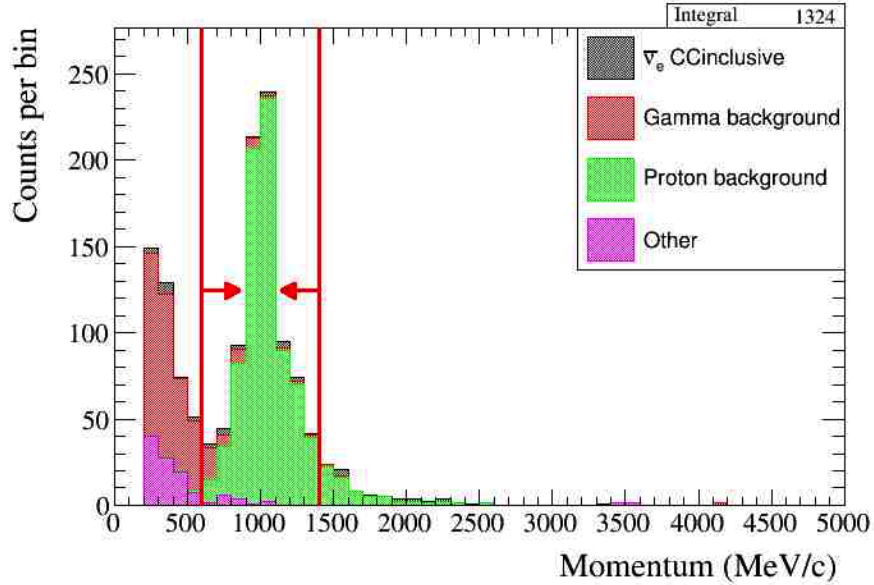
(b)

Figure A.4: The momentum of the positron candidate for events which have a DsECal component (a) and those which have a BrECal component (b) in the neutrino beam mode. The plots show that for the neutrino mode sample the proton peak tails out to higher momenta than for the antineutrino mode sample, where the tail cuts off at 1400 MeV/c as shown in Figures 4.15(a) and 4.15(b). The arrows indicate the position of the selection criteria. The coloured histogram is MC, grey is the $\bar{\nu}_e$ CC signal, green is the proton background, red is the gamma background and other backgrounds are shown in purple.
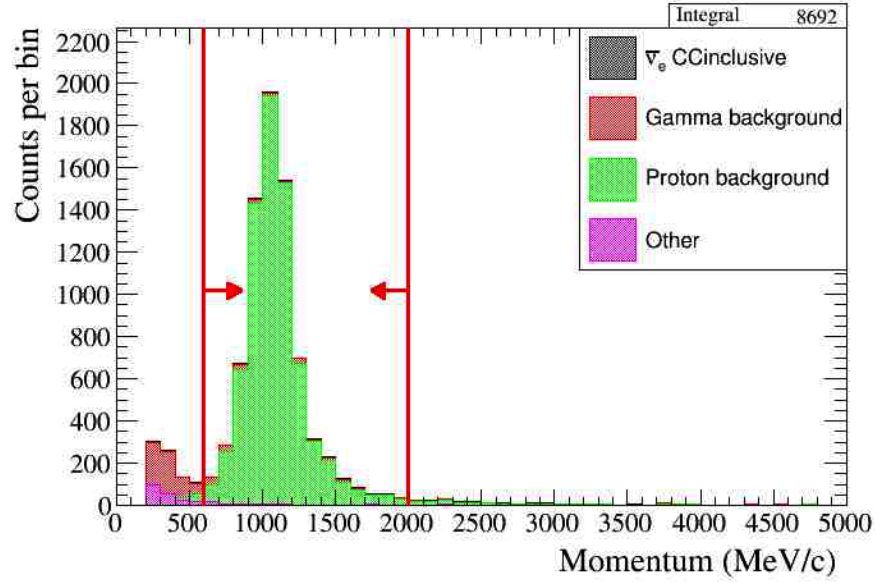
Figure A.5: The momentum of the positron candidate for events without reconstruction in either the DsECal or BrECal in neutrino beam mode. This plot shows that the tail on the proton events continues to be significant for higher momenta than 2000 MeV/c. The coloured histogram is MC, grey is the $\bar{\nu}_e$ CC signal, green is the proton background, red is the gamma background and other backgrounds are shown in purple.
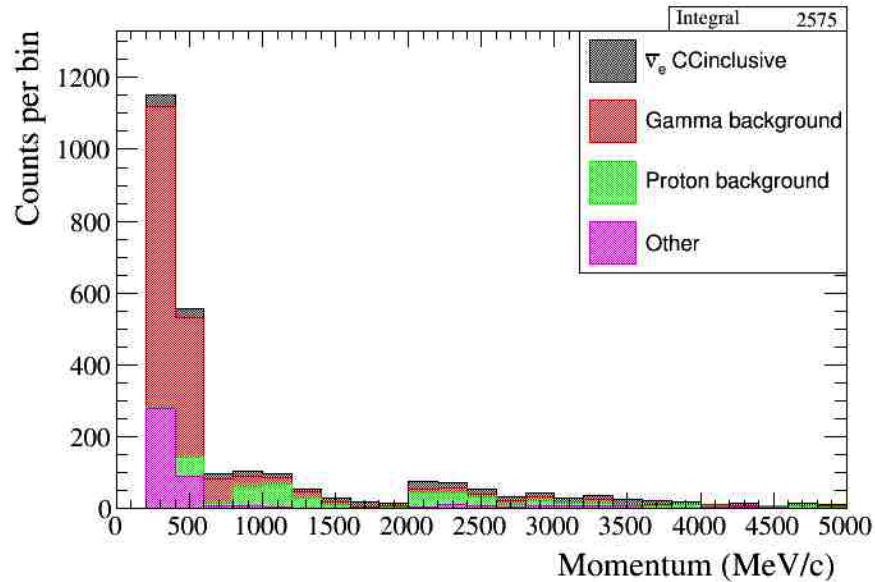
Figure A.6: The momentum of the positron candidate in the $\bar{\nu}_e$ sample after applying all criteria to MC simulation of the neutrino beam. The coloured histogram is MC, grey is the $\bar{\nu}_e$ CC signal, green is the proton background, red is the gamma background and other backgrounds are shown in purple.

Appendix B

Uncertainties on Efficiency and Purity

The efficiency (ξ) and purity (P) of a selection are defined in Equations B.1 and B.2.

$$\xi = \frac{Number\ of\ signal\ selected}{Number\ of\ signal\ before\ applying\ selection\ criteria} \tag{B.1}$$

$$P = \frac{Number\ of\ signal\ selected}{Total\ number\ of\ events\ selected} \tag{B.2}$$

With the number of events obeying counting statistics, the uncertainty on the numerators and denominators is:

$$\sigma_N = \sqrt{N} \tag{B.3}$$

The most common approach in physics for evaluating the uncertainty on a quantity is to use Poisson statistics where the uncertainty on efficiency or purity

would be calculated by:

$$\frac{\sigma_{quantity}}{quantity} = \sqrt{\left(\frac{\sigma_{Numerator}}{Numerator}\right)^2 + \left(\frac{\sigma_{Denominator}}{Denominator}\right)^2} \tag{B.4}$$

which, using Equation B.3 simplifies to:

$$\frac{\sigma_{quantity}}{quantity} = \sqrt{\frac{1}{Numerator} + \frac{1}{Denominator}} \tag{B.5}$$

However, Poisson statistics assumes large sample size which in neutrino physics where event rates are low is often not the case. A more correct method is to use binomial statistics which makes the following assumptions:

- There are a fixed number of tests.

- Each event is independent of the others.

- There are only two outcomes.

- The probability of each outcome remains constant from test to test.

In this case the uncertainty on a quantity (efficiency or purity) can be calculated by:

$$\sigma_{quantity} = \sqrt{\frac{quantity(1 - quantity)}{Total\ number\ of\ events\ selected}} \tag{B.6}$$

where the total number of events selected is equivalent to the number of binomial tests performed.

However, Equation B.6 begins to break down as one approaches a limiting case, such as efficiency or purity of 0% or 100% where the uncertainty will approach 0 even if the number of tests performed is small. A more correct solution would be to use Bayes' Theorem as presented in Section 3.1 of Reference [86]. However, the efficiency and purity of the analysis presented in the thesis are not limiting cases

and so it was decided to use binomial statistics and the uncertainty calculation shown in Equation B.6 to calculate the errors on efficiency and purity.

Appendix C

Glossary of Technical Terms and Abbreviations

13a flux reweighting - Corrections to the T2K flux.

BrECal - Barrel Electromagnetic Calorimeter

CC - Charged-Current

CCDIS - Charged-Current Deep Inelastic Scattering

CCQE - Charged-Current Quasi-Elastic

CCRES - Charged-Current Resonant

CP - Charge Parity

DAQ - Data Acquisition

DsECal - Downstream Electromagnetic Calorimeter

ECal - Electromagnetic Calorimeter

FGD - Fine Grained Detector

FLUKA2011 - A particle physics Monte-Carlo simulation package

Geant - A toolkit for the simulation of the passage of particles through matter

GENIE - A neutrino interaction simulation program

INGRID - Interactive Neutrino Grid

J-PARC - Japanese Proton Accelerator Research Complex

KamLAND - Kamioka Liquid Scintillator Antineutrino Detector

KATRIN - Karlsruhe Tritium Neutrino Experiment

LCG - LHC Computing GRID

LINAC - Linear Accelerator

LEP - Large Electron-Positron Collider

LSND - Liquid Scintillator Neutrino Detector

MC - Monte Carlo

MiniBooNE - Mini Booster Neutrino Experiment

MINOS - Main Injector Neutrino Oscillation Search

MIP - Minimum Ionising Particle

MPPC - Multi-Pixel Photon Counter

MSW - Mikheyev-Smirnov-Wolfenstein

NA61 - North Area 61, also known as SHINE - SPS Heavy Ion and Neutrino Experiment

NC - Neutral-Current

ND280 - Near Detector 280m

NDoF - Number of Degrees of Freedom

NEUT - A neutrino interaction simulation program

NOMAD - Neutrino Oscillation Magnetic Detector

P0D - Pi-Zero detector

PID - Particle Identification

PMNS - Pontecorvo-Maki-Nakagawa-Sakata

PMT - Photomultiplier Tube

POT - Protons on Target

SK - Super-Kamiokande

SMRD - Side Muon Ranged Detector

SNO - Sudbury Neutrino Observatory

T2K - Tokai to Kamioka

TPC - Time Projection Chamber

UA1 - Underground Area 1

WLS - Wavelength Shifting Fibre

Bibliography

[1] Glashow, S.L. 1961. Partial Symmetries of Weak Interactions. *Nucl. Phys.* **22**(4), pp. 579-588.

[2] Weinberg, S. 1967. A Model of Leptons. *Phys. Rev. Lett.* **19**(21), pp. 1264-1266.

[3] Svartholm, N. and Salam, A. 1968. Elementary Particle Physics: Relativistic Groups And Analycity. *Eighth Nobel Symposium, Stockholm, Almquvist and Wiksell.* 367.

[4] Higgs, P. 1964. Broken Symmetries and the Masses of Gauge Bosons. *Phys. Rev. Lett.* **13**(16), p. 508.

[5] Pauli, W. 1925. Zeeman-Effect and the Dependence of Electron-Mass on the Velocity. *Z. Phys.* **31**, p. 373.

[6] Bose, S.N. 1924. Plancks Gesetz und Lichtquantenhypothese. *Zeitschrift für Physik* **26**(1), p. 178.

[7] Eberhardt, O. *et al.* 2012. Impact of a Higgs Boson at a Mass of 126 GeV on the Standard Model with Three and Four Fermion Generations. *Phys. Rev. Lett.* **109**(24).

[8] Fritzsch, H. 1983. *Quarks: The Stuff of Matter.* Basic Books. ISBN 978-0-465-06781-7.

[9] Aaij, R. *et al.* (LHCb collaboration). 2015. Observation of J/ψp resonances consistent with pentaquark states in Λ^0 b→J/ψK-p decays. *Phys. Rev. Lett.* **115**(7).

[10] MissMJ. 2014. *Standard Model of Elementary Particles.* Licensed under CC BY-SA 3.0. [online] Available at: https://commons.wikimedia.org/wiki/ File:Standard_Model_of_Elementary_Particles.svg [Accessed 20 February 2016].

[11] HEL. 2007. *Right Left Helicity.* Licensed under CC BY-SA 3.0. [online] Available at: https://upload.wikimedia.org/wikipedia/en/7/75/Right_left_helicity.jpg

[12] Pauli, W. 1930. Open letter to radioactive persons. *Letter to a conference in Tubingen*, 4th December.

[13] Brown, L.M. 1978. The idea of the neutrino. *Physics Today.* **31**(9), p. 23.

[14] Cowan, C.L. Jr., Reines, F., Harrison, F.B., Kruse, H.W., and McGuire A.D. 1956. Detection of the Free Neutrino: a Confirmation. *Science.* **124**(3212), pp. 103-4.

[15] Feinberg, G. and Lederman, L.M. 1963. The Physics of Muons and Muon Neutrinos. *Annual Review of Nuclear Science.* **13**, pp. 431-504.

[16] Kodama, K. *et al.* (the DONUT collaboration). 2001. Observation of tau neutrino interactions. *Phys. Lett. B.* **504**(3), p. 218.

[17] Beringer, J. *et al.* (Particle Data Group). 2012. Review of particle physics. *Phys. Rev. D* **86**(1).

[18] Davis, R. Harmer, D.S. and Hoffman, K.C. 1968. Search for neutrinos from the sun. *Phys. Rev. Lett.* **20**(21), p. 1205.

[19] Bahcall, J.N. 1964. Solar Neutrino Cross Sections and Nuclear Beta Decay. *Phys. Rev.* **135**(1B), p. 137.

[20] Bahcall, J.N. Fowler, W.A. Iben, I. and Sears, R.L. 1963. Solar Neutrino Flux. *ApJ.* **137**(1), pp. 344-346.

[21] Bahcall, J.N. Pinsonneault, M.H. and Basu, S. 2001. Solar Models: current epoch and time dependences, neutrinos, and helioseismological properties. *Astrophys.J.* **555**(2), pp. 990-1012.

[22] Hirata, K. *et al.* (Kamiokande Collaboration). Real-time, directional measurement of ^{8}B solar neutrinos in the Kamiokande II detector. *Phys. Rev. D* **44**(8).

[23] Anselmann, P. *et al.* (GALLEX Collaboration). 1995. GALLEX solar neutrino observations: complete results for GALLEX II. *Phys. Lett. B.* **357**(1), pp. 237-247.

[24] Abdurashitov, J.N. *et al.* (SAGE Collaboration). 1999. Measurement of the solar neutrino capture rate with gallium metal. *Phys. Rev. C.* **60**(5).

[25] Altmann, M. *et al.* (GNO Collaboration). 2000. GNO Solar Neutrino Observations: Results for GNO I. *Phys. Lett. B.* **490**(1), pp. 16-26.

[26] Fukuda, S. *et al.* (Super-Kamiokande Collaboration). 2001. Solar ^{8}B and hep Neutrino Measurements from 1258 Days of Super-Kamiokande Data. *Phys. Rev. Lett.* **86**(25).

[27] Pontecorvo, B. 1968. Neutrino experiments and the question of leptonic-charge conservation. *Soviet Physics-JETP.* **26**, pp. 984-988.

[28] Ahmad, Q.R. *et al.* (SNO Collaboration). 2001. Measurement of the Rate of $\nu_e + \text{d} \rightarrow \text{p} + \text{p} + e^-$ Interactions Produced by ^{8}B Solar Neutrinos at the Sudbury Neutrino Observatory. *Phys. Rev. Lett.* **87**(7).

[29] Fukuda, Y. *et al.* (Super-Kamiokande Collaboration). 1998. Evidence for Oscillation of Atmospheric Neutrinos. *Phys. Lett.* **81**(8).

[30] Eguchi, K. *et al.* (KamLAND Collaboration). 1998. First Results from Kam-LAND: Evidence for Reactor Antineutrino Disappearance. *Phys. Lett.* **90**(2).

[31] Ahuja, G. Gupta, M. and Randhawa, M. 2007. Constructing the CKM and PMNS matrices from mixing data. *PU Research Journal.* **57**.

[32] Abe, K. *et al.* (The T2K Collaboration). 201I. Indication of Electron Neutrino Appearance from an Accelerator-Produced Off-Axis Muon Neutrino Beam. *Phys. Rev. Lett.* **107**(4).

[33] An, F.P. *et al.* (The Daya Bay Collaboration). 2012. Observation of Electron-Antineutrino Disappearance at Daya Bay. *Phys. Rev. Lett.* **108**(17).

[34] Rosen, S.P. and Gelb, J.M. 1986. Mikheyev-Smirnov-Wolfenstein enhancement of oscillations as a possible solution to the solar-neutrino problem. *Phys. Rev. D.* **34**(4), p. 969.

[35] Abe, K. *et al.* (The T2K Collaboration). 2014. Precise Measurement of the Neutrino Mixing Parameter θ_{23} from Muon Neutrino Disappearance in an Off-Axis Beam. *Phys. Lett.* **112**(18).

[36] kismalac. 2011. *Neutrino mass hierarchy.* Licensed under CC BY-SA 3.0. [online]. Available at: https://commons.wikimedia.org/wiki/File:NeutrinoHierarchy.svg [Accessed 20 February 2016].

[37] Lesgourgues, J. and Pastor, S. 2014. Neutrino cosmology and Planck. *New Journal of Physics.* **16**(6).

[38] Kraus, Ch. *et al.* 2005. Final results from phase II of the Mainz neutrino mass searching tritium β decay. *Eur.Phys.J.* **40**(4), pp. 447-468.

[39] Drexlin, G. Hannen, V. Mertens, S. and Weinheimer, C. 2013. Current Direct Neutrino Mass Experiments. *Advances in High Energy Physics.* **2013**. Article ID 293986.

[40] Kayser, B. 2009. Are Neutrinos Their Own Antiparticles?. *J. Phys. Conf.Ser.* 173:012013.

[41] The ALEPH Collaboration, the DELPHI Collaboration, the L3 Collaboration, the OPAL Collaboration, the SLD Collaboration, the LEP Electroweak Working Group, the SLD electroweak, heavy flavour groups. 2006. Precision Electroweak Measurements on the Z Resonance. *Phys. Rept.* **427**(5), pp. 257-454.

[42] A. Aguilar *et al.* (LSND Collaboration). *et al.* 2001. Evidence for neutrino oscillations from the observation of $\bar{\nu}_e$ appearance in a $\bar{\nu}_\mu$ beam. *Phys. Rev. D.* **64**(11).

[43] Mention, G. *et al.* 2011. The reactor antineutrino anomaly. *Phys. Rev. D.* **83**(7).

[44] Giunti, C. and Laveder, M. 2011. Statistical significance of the gallium anomaly. *Phys. Rev. C.* **83**(6).

[45] Aguilar-Arevalo, A.A. *et al.* 2013. Improved search for $\bar{\nu}_\mu \rightarrow \bar{\nu}_e$ oscillations in the MiniBooNE experiment. *Phys.Rev.Lett.* **110**(16).

[46] Pakvasa, S. 2000. Neutrino anomalies without oscillations. *Pramana.* **54**(1). pp. 65-77.

[47] Machado, P. Nunokawa, P. Pereira dos Santos, F. and Zukanovich Funchal, R. 2012. Bulk neutrinos as an alternative cause of the gallium and reactor anti-neutrino anomalies. *Phys. Rev. D* **85**(7).

[48] Adamson, P. *et al.* (The MINOS Collaboration). 2010. Search for sterile neutrino mixing in the MINOS long-baseline experiment, *Phys. Rev. D.* **81**(5).

[49] Ghosh, A. Thakore, T. and Choubey, S. 2013. Determining the Neutrino Mass Hierarchy with INO, T2K, NOvA and Reactor Experiments. *JHEP.* **2013**(04).

[50] Abe, K. *et al.* (The T2K Collaboration). 2015. Neutrino oscillation physics potential of the T2K experiment. *Prog. Theor. Exp. Phys.* 043C01.

[51] Formaggio, J.A. and Zeller, G.P. 2012. From eV to EeV: Neutrino cross sections across energy scales. *Rev. Mod. Phys.* **84**(3), pp. 1307-1341.

[52] Abe, K. *et al.* (The T2K Collaboration). 2011. The T2K Experiment. *Nucl. Instrum. Methods A.* **659**(1), pp. 106-135.

[53] Abe, K. *et al.* (The T2K Collaboration). 2013. Evidence of electron neutrino appearance in a muon neutrino beam. *Phys. Rev. D* **88**(3).

[54] Abe, K. *et al.* (T2K Collaboration). 2014. Observation of Electron Neutrino Appearance in a Muon Neutrino Beam. *Phys. Rev. Lett.* **112**(6).

[55] Nagamiya, S. (2012). Introduction to J-PARC. *Prog. Theor. Exp. Phys.* **2012**(2).

[56] Ichikawa, A.K. 2012. Design concept of the magnetic horn system for the T2K neutrino beam. *Nucl. Instrum. Methods A.* **690**, pp. 27-33.

[57] Kormos, L. 2010. *Towards Seeking θ_{13}: Status and Initial Data from T2K.* XIV Mexican School on Particles and Fields.

[58] Nakaya, T. and Plunkett, R. 2015. Neutrino Oscillations with the MINOS, MINOS+, T2K, and NOvA Experiments. *New Journal of Physics.* **18**(1).

[59] Abgrall, N. *et al.* (The NA61/SHINE Collaboration). 2011. Measurements of cross sections and charged pion spectra in proton-carbon interactions at 31 GeV/c. *Phys. Rev. C.* **84**(3).

[60] Kudenko, Y. 2009. The Near neutrino detector for the T2K experiment. *Nucl. Instrum. Methods A* **598**(1), pp. 289-295.

[61] Abe, K. *et al.* (The T2K Collaboration). 2012. Measurements of the T2K neutrino beam properties using the INGRID on-axis near detector. *Nucl. Instrum. Methods A.* **694**(1), pp. 211-223.

[62] Frank, E. *et al.* 2012. A dedicated device for measuring the magnetic field of the ND280 magnet in the T2K experiment. *JINST.* **7**(1).

[63] Abgrall, N. *et al.* (T2K ND280 TPC collaboration). 2011. Time projection chambers for the T2K near detectors. *Nucl. Instrum. Methods A.* **637**(1), pp. 25-46.

[64] Vasseur, G. 2012. Operation of the T2K time projection chambers *JINST.* **7**(2).

[65] Amaudruz, P.A. *et al.* (T2K ND280 FGD Collaboration). 2012. The T2K fine-grained detectors. *Nucl. Instrum. Methods A.* **696**, pp. 1-31.

[66] Yokoyama, M. *et al.* 2010. Performance of Multi-Pixel Photon Counters for the T2K near detectors. *Nucl. Instrum. Methods A.* **622**(3), pp. 567-573.

[67] Allan, D. *et al.* (T2K UK). 2013. The Electromagnetic Calorimeter for the T2K Near Detector ND280. *JINST.* **8**(10), P10019.

[68] Assylbekov, S. *et al.* 2012. The T2K ND280 off-axis pi-zero detector. *Nucl. Instrum. Methods A.* **686**, pp. 48-63.

[69] Aoki, S. *et al.* 2012. The T2K Side Muon Range Detector (SMRD). *Nucl. Instrum. Methods A.* **698**, pp. 135-146.

[70] Uchida, Y. 2010. ND280 Data and MC Processing and Distribution. *T2K ASG Conveners Meeting at J-PARC.*

[71] Shiozawa, M. *et al.* (The SK Collaboration). 1998. Search for Proton Decay via p $\rightarrow e^+ + \pi^0$ in a Large Water Cherenkov Detector. *Phys. Rev. Lett.* **81**(16), p. 3319.

[72] Mitsui, K. Kitamura, T. Wada, T. and Okei, K. 2003. Identification problems of muon and electron events in the Super-Kamiokande detector. *Journal of Physics G: Nuclear and Particle Physics.* **29**(9).

[73] Abe, K. *et al.* (T2K Collaboration). 2014. Measurement of the intrinsic electron neutrino component in the T2K neutrino beam with the ND280 detector. *Phys. Rev. D.* **89**(9).

[74] Abe, K. *et al.* (T2K Collaboration). 2014. Measurement of the Inclusive Electron Neutrino Charged Current Cross Section on Carbon with the T2K Near Detector. *Phys. Rev. Lett.* **113**(24).

[75] Hayato, Y. 2009. A neutrino interaction simulation program library NEUT. *Acta Phys.Polon. B.* **40**, pp. 2477-2489.

[76] Andreopoulos, C. *et al.* 2009 The GENIE Neutrino Monte Carlo Generator. *Nucl. Instrum. Methods A.* **614**(1), pp. 87-104.

[77] Battistoni, G. Cerutti F. Fasso, A. Ferrari, A. Muraro, S. Ranft, J. Roesle, S. and Sala, P.R. 2007. The FLUKA code: Description and benchmarking. *AIP Conference Proceeding.* **896**. pp. 31-49.

[78] Abe, K. *et al.* (T2K Collaboration). 2013. T2K neutrino flux prediction. *Phys. Rev. D.* **87**(1).

[79] Abgrall, N. *et al.* (The NA61/SHINE Collaboration). 2013. Pion emission from the T2K replica target: Method, results and application. *Nucl. Inst. and Meth. in Phys. Res. A.* **701**, pp. 99-114.

[80] Agostinelli, S. *et al.* 2003. Geant4 a simulation toolkit. *Nucl. Instrum. Meth. A.* **506**(3), pp. 250-303.

[81] Brun, R. and Rademakers, F. 1997. ROOT an object oriented data analysis framework. *Nucl. Inst. and Meth. in Phys. Res. A.* **389**, pp. 81-86.

[82] Barker, G. *et al.* 2012. Implementation of the Second Generation PID for the ND280 Tracker ECals. T2K internal technical note TN 111.

[83] Brook-Roberge, D. 2012. Measurements of Neutrino Interactions on Water using a Fine-Grained Scintillator Detector with Water Targets. *PhD thesis. The University Of British Columbia.*

[84] Hartz, D. *et al.* 2014. Constraining the Flux and Cross Section Models with Data from the ND280 Detector for the 2014/15 Oscillation Analysis. T2K internal technical note TN 220.

[85] Bross, A. 2013. *Neutrinos from Stored Muons.* NuPhys 2013.

[86] Paterno, M. 2003. Calculating Efficiencies and Their Uncertainties. FERMILAB- TM-2286-CD.